

A Study of Millerite from Cu-Ni-PGE Footwall Veins, Sudbury, ON: Crystal-Chemistry,  
Morphology, & Geological Implications

by

Thomas Edward Gore

Thesis submitted in partial fulfilment  
of the requirements for the degree of  
Masters of Science in Geology

The Faculty of Graduate Studies  
Laurentian University  
Sudbury, Ontario, Canada

© Thomas Edward Gore, 2020

**THESIS DEFENCE COMMITTEE/COMITÉ DE SOUTENANCE DE THÈSE**  
**Laurentian Université/Université Laurentienne**  
Faculty of Graduate Studies/Faculté des études supérieures

Title of Thesis Titre de la thèse	A Study of Millerite from Cu-Ni-PGE Footwall Veins, Sudbury, ON: Crystal-Chemistry, Morphology, & Geological Implications	
Name of Candidate Nom du candidat	Gore, Thomas Edward	
Degree Diplôme	Master of Science	
Department/Program Département/Programme	Geology	Date of Defence Date de la soutenance May 20, 2020

**APPROVED/APPROUVÉ**

Thesis Examiners/Examineurs de thèse:

Dr. Andrew McDonald  
(Supervisor/Directeur de thèse)

Dr. Pedro Jugo  
(Committee member/Membre du comité)

Dr. Daniel Marshall  
(External Examiner/Examineur externe)

Approved for the Faculty of Graduate Studies  
Approuvé pour la Faculté des études supérieures  
Dr. David Lesbarrères  
Monsieur David Lesbarrères  
Acting Dean, Faculty of Graduate Studies  
Doyen intérimaire, Faculté des études supérieures

**ACCESSIBILITY CLAUSE AND PERMISSION TO USE**

I, **Thomas Edward Gore**, hereby grant to Laurentian University and/or its agents the non-exclusive license to archive and make accessible my thesis, dissertation, or project report in whole or in part in all forms of media, now or for the duration of my copyright ownership. I retain all other ownership rights to the copyright of the thesis, dissertation or project report. I also reserve the right to use in future works (such as articles or books) all or part of this thesis, dissertation, or project report. I further agree that permission for copying of this thesis in any manner, in whole or in part, for scholarly purposes may be granted by the professor or professors who supervised my thesis work or, in their absence, by the Head of the Department in which my thesis work was done. It is understood that any copying or publication or use of this thesis or parts thereof for financial gain shall not be allowed without my written permission. It is also understood that this copy is being made available in this form by the authority of the copyright owner solely for the purpose of private study and research and may not be copied or reproduced except as permitted by the copyright laws without written authority from the copyright owner.

## ABSTRACT

Millerite ( $\beta$ -NiS) is a common accessory mineral in magmatic Cu-Ni-PGE deposits, such as those occurring in Sudbury, Ontario, Canada. In such localities, millerite develops as platy crystals, often forming large, cleavable masses. This is in stark contrast to the more widespread occurrence of millerite as a hydrothermal precipitate within vugs in carbonate basins, where it develops an acicular morphology, with crystals often exhibiting exaggerated aspect ratios ( $l:w > 20$ ). The reason for these contrasting morphologies is attributed directly to the genesis of magmatic millerite that initially crystallizes as the high-temperature mineral crowningshieldite ( $\alpha$ -NiS), later inverting to millerite upon further cooling. The morphology exhibited by platy millerite is thus representative of crowningshieldite *via* a paramorphic relationship. Millerite of magmatic origin also frequently exhibits secondary twinning on  $\{01\bar{1}2\}$ , resulting from a post-crystallization increase in pressure. Development of these twins produces a variable response under BSE microscopy that is attributed to orientation contrast.

## KEYWORDS

Millerite, NiS, magmatic sulphide, crystal structure, morphology, polymorph, crystal growth, twinning, backscatter coefficient, electron channelling

## ACKNOWLEDGEMENTS

This project represents the culmination of years of work, not only my own, but of countless others who have provided their assistance along the way. This section is dedicated to them.

To my supervisor, Dr. Andrew McDonald, I would like to convey my most sincere gratitude for supporting me not only in this project, but for guiding me through the fascinating world of mineralogy since I first stepped into his classroom in 2014. Without his tireless efforts reviewing shoddy abstracts and manuscripts, facilitating hours upon hours of discussion, and teaching me the invaluable skill of observation as a scientist, this project would have been impossible. To Dr. Pedro Jugo, who assisted me in designing the synthesis experiments, and generously allowed me access to and use of his experimental petrology laboratory. To Willard Desjardins, for preparing all of the polished thin sections examined over the course of this study. To Dr. William Zhe and Chris Beckett-Brown, who assisted greatly in collecting and processing EBSD data. To Rémy Poulin, who assisted in collecting PXRD data. To Brad Lazich, Andre Stewart, and Kevin Pieterse of Nickel Rim South mine, and Brian Gauvreau and Kyle Kauppi of Coleman mine for facilitating access to the mines and assisting with sample collection. To Erika Anderson and Ralph Rowe of the Canadian Museum of Nature for providing the representative samples of hydrothermal millerite for comparison. To all my fellow classmates and graduate students, for the years of camaraderie and passionate geological discussions. And finally to my family, for all the endless support they have given me over the years and helping me in pursuit of my passion.

Our evolving scientific understanding of the world we live in is built on the shoulders of those who came before us. Their theories and propositions provide the foundations for our interpretations and understandings. Similarly, this project was not a singular undertaking, but was only achievable through the support of everyone mentioned above, and a great number of others who were not named explicitly. To all of them, I owe a depth of gratitude.

Thank you.

Thomas E. Gore

# TABLE OF CONTENTS

THESIS DEFENCE COMMITTEE .....	ERROR! BOOKMARK NOT DEFINED.
ABSTRACT.....	III
ACKNOWLEDGEMENTS .....	IV
TABLE OF CONTENTS.....	V
LIST OF FIGURES .....	VII
LIST OF TABLES .....	VIII
LIST OF EQUATIONS.....	VIII
PREAMBLE .....	IX

## **Chapter 1: .....** 1

### **Relationship Between the Crystal Chemistry & Morphology of Millerite.....** 1

ABSTRACT.....	2
1.0 INTRODUCTION.....	3
1.1 BACKGROUND.....	5
1.1.1 Structure & Morphology .....	5
1.1.2 Structure & Polymorphism of NiS.....	7
1.1.3 Phase Equilibrium.....	11
1.1.3.1 THE FE-NI-S TERNARY SYSTEM .....	11
1.1.3.2 THE FE-NI-CU-S QUATERNARY SYSTEM.....	14
1.1.3.3 THE NI-S BINARY SYSTEM .....	16
1.1.4 Synthesis of $\alpha$ -NiS .....	19
1.1.5 Notes on Magmatic vs. Hydrothermal Millerite.....	21
1.1.6 Sample Locations .....	22
1.2 METHODS.....	25
1.2.1 Chemistry.....	25
1.2.2 CVT Synthesis.....	25
1.2.3 X-Ray Diffraction .....	26
1.3 OBSERVATIONS.....	27
1.3.1 Hand Samples.....	27
1.3.2 Reflected Light Petrography.....	30
1.3.3 Electron Microscopy I – PGMs & Associated Trace Minerals.....	34
1.3.4 Electron Microscopy II – Synthetic Materials.....	39
1.4 RESULTS.....	44
1.4.1 Chemistry.....	44
1.4.2 X-Ray Diffraction .....	49
1.5 DISCUSSION.....	51
1.5.1 Genesis of Cu-Ni-PGE Veins in the Sudbury Basin .....	51
1.5.2 Chemical Influences (or Lack Thereof) on Morphology .....	54
1.5.3 Structural & Genetic Influences on Morphology .....	55
1.5.4 Comments on the Stability & Inversion of NiS.....	57
1.6 CONCLUSIONS.....	59
1.7 REFERENCES.....	61

## **Chapter 2: .....** 66

### **Orientation Contrast & Twinning in Millerite from the Sudbury Basin .....** 66

ABSTRACT.....	67
2.0 INTRODUCTION.....	68

<b>2.1 BACKGROUND.....</b>	<b>69</b>
2.1.1 Backscattered-Electron Imaging.....	69
2.1.2 Sample Locations .....	72
<b>2.2 METHODS.....</b>	<b>72</b>
2.2.1 Chemistry.....	72
2.2.2 Electron Backscatter Diffraction.....	73
<b>2.3 OBSERVATIONS.....</b>	<b>73</b>
2.3.1 Hand Samples.....	73
2.3.2 Petrography of Millerite.....	75
2.3.3 Electron Microscopy .....	76
<b>2.4 RESULTS.....</b>	<b>78</b>
2.4.1 Chemistry.....	78
2.4.2 Electron Backscatter Diffraction.....	80
<b>2.5 DISCUSSION.....</b>	<b>83</b>
2.5.1 Orientation Contrast .....	83
2.5.2 Twinning.....	86
2.5.3 Notes on Orientation Contrast in Geological Materials.....	90
<b>2.6 CONCLUSIONS.....</b>	<b>91</b>
<b>2.7 REFERENCES.....</b>	<b>92</b>
<b>APPENDIX A – MINERALOGY OF MAGMATIC SAMPLES.....</b>	<b>94</b>
Table A1 – Macroscopic Mineralogy.....	94
Table A2 – Microscopic Mineralogy.....	96
<b>APPENDIX B – CHEMISTRY OF MILLERITE .....</b>	<b>97</b>
Table B1 – Chemistry of Magmatic Millerite.....	97
Table B2 – Chemistry of Hydrothermal Millerite .....	101
<b>APPENDIX C – TEMPERATURE GRADIENTS FOR FURNACES .....</b>	<b>104</b>
Table C1 – Temperature Gradients for Chico .....	104
Table C2 – Temperature Gradients for Gummo .....	104
<b>APPENDIX D – CATALOGUE OF ALL MILLERITE &amp; NIS SPECIMENS .....</b>	<b>105</b>
<u>Samples from Canadian Museum of Nature.....</u>	105
<u>Samples from Nickel Rim South Mine .....</u>	105
<u>Samples from Coleman Mine .....</u>	110
<u>Samples from the Morrison Deposit.....</u>	113
<u>Samples Synthesized by CVT.....</u>	115

## LIST OF FIGURES

<b>FIG. 1.1.</b> Crystal structures of the two NiS polymorphs .....	8
<b>FIG. 1.2.</b> Idealized 3D models of NiS crystals .....	11
<b>FIG. 1.3.</b> Ternary diagram illustrating equilibrium in the Fe-Ni-S system .....	13
<b>FIG. 1.4.</b> Compositional fields in the Fe-Ni-Cu-S quaternary system at 760 °C.....	15
<b>FIG. 1.5.</b> Phase diagram of the Ni-S system.....	17
<b>FIG. 1.6.</b> Changes in the atomic structure of NiS during the $\alpha \rightarrow \beta$ transition .....	18
<b>FIG. 1.7.</b> Schematic cross section of CVT.....	21
<b>FIG. 1.8.</b> Plan view map of the Sudbury Basin .....	23
<b>FIG. 1.9.</b> Massive sulphide vein underground at the 1740 m level of Coleman mine.....	24
<b>FIG. 1.10.</b> Representative hand samples of mlr and associated minerals .....	29
<b>FIG. 1.11.</b> Idealized paragenetic sequence of millerite and associated minerals.....	30
<b>FIG. 1.12.</b> RL images of mlr and associated minerals from magmatic systems.....	33
<b>FIG. 1.13.</b> BSE images of PGMs and associated minerals from magmatic systems - I .....	36
<b>FIG. 1.14.</b> BSE images of PGMs and associated minerals from magmatic systems - II .....	38
<b>FIG. 1.15.</b> BSE images of PGMs and associated minerals from magmatic systems - III.....	40
<b>FIG. 1.16.</b> Trends in grain development during CVT.....	41
<b>FIG. 1.17.</b> SE images of synthetic crystals of $\alpha$ -NiS grown using chemical vapour transport .....	43
<b>FIG. 1.18.</b> Ternary diagram representing millerite chemistry .....	45
<b>FIG. 1.19.</b> <i>Me</i> :S values magmatic millerite .....	47
<b>FIG. 1.20.</b> <i>Me</i> :S values hydrothermal millerite. ....	47
<b>FIG. 1.21.</b> Distribution curves for <i>Me</i> :S values of millerite. ....	48
<b>FIG. 1.22.</b> Calculated X-ray diffraction powder patterns for $\alpha$ -NiS and $\beta$ -NiS).....	50
<b>FIG. 1.23.</b> Diffractograms for synthetic $\alpha$ -NiS and millerite from Coleman mine.....	50
<b>FIG. 1.24.</b> $\alpha \rightarrow \beta$ transition temperature vs pressure. ....	58
<b>FIG. 2.1.</b> $\eta$ vs $Z_{avg}$ .....	70
<b>FIG. 2.2.</b> Electron channelling in a 2D crystal lattice.....	71
<b>FIG. 2.3.</b> Hand sample images of millerite .....	74
<b>FIG. 2.4.</b> RL & BSE images of millerite .....	77
<b>FIG. 2.5.</b> BSE images of millerite from Coleman mine .....	79
<b>FIG. 2.6.</b> Bar graph of millerite chemistry from Coleman mine .....	80
<b>FIG. 2.7.</b> EBSD map of millerite from Coleman mine .....	82
<b>FIG. 2.8.</b> Orientation of millerite twins from Coleman mine .....	82
<b>FIG. 2.9.</b> 3D crystal and crystal-structure representations of millerite twins .....	84

## LIST OF TABLES

<b>Table 1.1:</b> Information Relating to Millerite Examined .....	24
<b>Table 1.2:</b> Parameters for CVT Synthesis .....	26
<b>Table 2.1:</b> Mineral Chemistry of Millerite from Coleman Mine .....	79

## LIST OF EQUATIONS

<b>Eq. 1.1</b> Chemical reaction for the transition of equimolar NiS .....	16
<b>Eq. 1.2</b> Chemical reaction for the transition of metal-deficient NiS .....	17
<b>Eq. 1.3</b> General chemical reaction for chemical-vapour transport .....	20
<b>Eq. 2.1</b> Calculation of $\eta$ based on $Z_{\text{avg}}$ of a given material .....	69

## **PREAMBLE**

This manuscript is divided into two sections, each addressing a specific question with regards to the overall study.

Chapter 1 is dedicated to defining the relationship between the crystal-chemistry and the morphology of millerite ( $\beta$ -NiS). This is accomplished by categorizing and defining the occurrence of millerite from the selected localities including: mineral assemblages (when applicable), textural relationships, morphology, paragenesis, chemistry, and structure.

Chapter 2 addresses controls on the backscatter coefficient ( $\eta$ ) of crystalline materials, specifically with respect to the observations made in several samples of millerite from the Sudbury area. The effects of orientation contrast and electron channelling are examined, and the role and nature of polysynthetic twinning in millerite is described in detail.

The findings of this study and the interpretations presented herein may be expanded and applied to other occurrences of millerite globally, well beyond the confines of the Sudbury area.

# **Chapter 1:**

## **Relationship Between the Crystal Chemistry & Morphology of Millerite**

## ABSTRACT

Millerite ( $\beta$ -NiS) is a common accessory mineral in magmatic Cu-Ni-PGE (and some Fe-Ni) deposits, such as those found in Sudbury, Ontario, Canada, the Noril'sk region in Russia, and the Marbridge mine in Québec, Canada. It is also a widespread secondary mineral found within vugs in sedimentary basins. The prior occurrence exhibits the development of platy crystals of millerite, while the latter environment shows only the development of acicular crystals of millerite. This dichotomy exhibited by the habit of millerite suggests a relationship between the environment of formation and the resultant external morphology of the crystals, possibly through chemical differences inherent in the environment, or other genetic factors. In addition to the common mineral, millerite, NiS may also adopt the structural form as crowningshieldite ( $\alpha$ -NiS) as temperatures above 379 °C. Millerite from both magmatic and hydrothermal occurrences were investigated *via* SEM-EDS, PXRD, and synthetic crystals of  $\alpha$ -NiS were grown for morphological analysis. Chemical analyses did not indicate any significant correlation between mineral chemistry or stoichiometry and the environment of formation, indicating that substitution and/or metal-deficiency does not exert a measurable impact on the morphology of millerite crystals. Synthetic crystals of  $\alpha$ -NiS demonstrated a predominantly platy morphology, similar to that observed amongst millerite of magmatic origin, suggesting a link between crowningshieldite and millerite in these types of environments. It is thus concluded that millerite in magmatic systems initially crystallized as crowningshieldite at temperatures above 379 °C, and subsequently experienced a solid-state phase transformation to millerite. Such a process preserved the external morphology of crowningshieldite through the paramorphic relationship, and explains the predominance of platy millerite in magmatic systems.

## 1.0 INTRODUCTION

Advancements in modern analytical techniques have greatly facilitated the acquisition of comprehensive datasets for geological materials, including but not limited to: whole rock geochemistry, in-situ trace-element concentrations, isotopic compositions, grain-size analysis, grain orientation, and structural information. Although the emergence of techniques such as laser-ablation-ICP-MS, high-resolution single-crystal XRD, and select-area electron diffraction have greatly contributed to advancing our knowledge and understanding of the natural world, it is critical that other, more basic techniques are not completely usurped by modern methods. This is directed particularly with respect to the information that can be gleaned from initial visual observations of rocks and minerals. Human beings are by nature largely visual creatures (Wilson 2004), and as the initial examinations made on any encountered material will be entirely physical in nature, these interpretations as to what they are and how they formed will rely heavily upon visual observations. With respect to observations of individual mineral species, the first observations made (almost subconsciously) upon contact will be the size, the colour, and inevitably the shape of the material. These three observations can be made rapidly, simply, and even when the observer lacks a general understanding of geological principles. However, despite the apparent simplicity of these actions, they are the first step in the geological interpretation of any sample. Aside from simple mineral identification, these observations can provide extensive information regarding the genetic history of the minerals themselves, their chemical composition, and the geological conditions under which they formed. This information in turn can be extended to encompass the geological environment of the locality as a whole. The case will be made herein that the observation of external morphology is the most significant of these three initial observations when it comes to interpreting the geological history of the sample.

The diversity exhibited within the mineralogical realm in terms of the morphological variations for a given mineral species within the natural environment is truly astounding. Calcite alone has been documented to exhibit over 2500 naturally occurring morphologies (Goldschmidt

1916). A comprehensive study conducted by V. M. Goldschmidt in the early part of the 20<sup>th</sup> century documented the morphologies of all known minerals at the time, and was compiled in nine volumes together exhibiting thousands of individual crystal shapes (Goldschmidt 1913a, 1913b, 1916, 1918a, 1918b, 1920, 1922a, 1922b, 1923). Further research in the variations exhibited by specific minerals was conducted throughout the 20<sup>th</sup> century, including comprehensive documentation of morphological variations of calcite and pyrite (Sunagawa 1953, 1957). More recent studies have investigated the relationship between the morphologies of certain minerals and the nature of the geological environment in which they formed. For example: (1) the length-to-width ratio of arsenopyrite can provide clues as to the As:S value for a given crystal (Kerstedjian 1997); (2) the morphology of pyrite and the presence of striations along certain crystal faces had been linked to the conditions of supersaturation and the chemistry of the parent fluid (Endo & Sunagawa 1973; Murowchick & Barnes 1987); and (3) the morphology of zircon crystals can be used as a tool to infer the alkalinity, temperature, and H<sub>2</sub>O content of the environment of formation (Pupin 1980). These are simply a few examples of how the morphology of a mineral can be used to interpret the complexity of a geological system, and how powerful such a simple observation may prove to be.

In systems as complex as those observed in nature, the external morphology of a mineral can be influenced by a wide variety of factors including (but not limited to): temperature, pressure, chemistry of the system, availability of space, growth rate,  $E_h$ , pH, rate of cooling, nutrient supply, flow direction, and saturation of the system (Kirkpatrick 1975). Such factors are considered to be *extrinsic*, in the sense that they are dictated and controlled by the physio-chemical conditions present in the environment of formation. However, outside of these parameters, if one assumes ideal physical and chemical growth conditions, the fundamental underlying principle that governs the geometric form adopted by a given mineral is the internal arrangement of the constituent atoms of the material, *i.e.* the atomic structure (Sunagawa 1999). This gives rise to the so-called *equilibrium form*, *i.e.* the ideal geometric form adopted by a given

crystalline material if only *intrinsic* factors (*i.e.* those directly related to the crystal structure of the material) are considered. Such factors include, but are not restricted to atom-type, coordination polyhedra, crystal-structure configurations, and interplanar spacing (Einstein 2015).

The importance of understanding particularly the intrinsic crystal-structure factors influencing the morphology of a crystal will be considered herein to explain observations made on the relatively common mineral, millerite ( $\beta$ -NiS) that represents a common constituent in footwall Cu-Ni-PGE samples from select mines in the Sudbury basin, along with those from world-wide occurrence from both other magmatic Cu-Ni-PGE deposits (such as Noril'sk) and low-temperature environments such as carbonate basins, and supergene alteration zones. General observations of millerite indicate that material coming from what are presumed to be low-temperature environments (often carbonate-hosted sedimentary basins) is typically acicular to prismatic in morphology (Dana 1949), while that associated with magmatic ore deposits typically exhibits a platy morphology (Ramdohr 1969; Graterol & Naldrett 1971; Wawrzonkowski 2015). The striking difference in morphologies between these occurrences of millerite suggests the existence of a possible relationship between the environment of formation and the morphology of the resulting crystals. As such, an examination of mineral assemblages containing millerite from both magmatic and hydrothermal localities has been undertaken. This will involve documentation of the morphology of the millerite in conjunction with investigation of potential crystal-chemical influences on external morphology. The broader implications are to examine and provide a more complete interpretation of the geological system in which it formed.

## **1.1 BACKGROUND**

### *1.1.1 Structure & Morphology*

The fundamental understanding of the ways in which the atomic (crystal) structure influences the morphology of crystalline materials is a growing and ever-evolving field of research that goes back to the early observations of snowflakes made by Johannes Kepler in the

early part of the 17<sup>th</sup> century. While the application of a modern understanding of atomic theory was impossible at the time, Kepler (1611) correctly proposed that the external shape of materials exhibiting nearly perfect geometric forms, such as snowflakes (which we now understand to be crystalline materials), must in some way be related to the way in which the matter that composes them is internally arranged. In the latter half of the 17<sup>th</sup> century, Nicolas Steno (1669) proposed that the cause for mineral exhibiting different polyhedral forms was due to growth-rate anisotropy, although empirical confirmation of this would not appear for nearly 200 more years. Auguste Bravais is credited with first describing the concept of a unit cell (the basic building blocks of crystals) in the mid-19<sup>th</sup> century, and provided a mathematical framework for the relationship between crystal structure and crystal morphology (Bravais 1850). He also devised an empirical rule known as *The Law of Bravais* linking the development of crystal faces to their associated reticular densities. The law explicitly states that “the growth rate of a crystal face is inversely proportional to the interplanar spacing,  $d_{hkl}$ , corresponding to that face” (Bravais 1866). In other words, crystals will tend to grow faster along their shortest crystallographic axis, resulting in the development of larger crystal faces parallel to this axis. In effect, crystals will be dominated by forms corresponding to those planes along which unit cells are added the fastest, *i.e.* those having the shortest crystallographic length. At the same time the law also serves to explain how the dominant forms present on a very small crystal ( $\leq 1 \mu\text{m}$ ) may not be represented on one of the same type several mm in diameter as these faces effectively grow themselves out of existence as the crystal increases in size (Hartman 1958).

With the advent of X-ray crystallography at the onset of the 20<sup>th</sup> century, the prevailing notions underlying the structure of minerals and their periodic nature were confirmed, providing the opportunity to refine the relationship between crystal structure and external morphology. Donnay & Harker (1937) introduced an extension to The Law of Bravais to help account for the influences of screw-axes and glide-planes on reticular density (which were unknown during Bravais' time), and these concepts were then further developed into the modern theory of the

periodic-bond-chain (PBC) (Hartman & Perdok 1955a, 1955b, 1955c). However, the underlying principle of growth-rate anisotropy persists to this day, and still represents the most fundamental concept in interpreting the influences of crystal structure on the external morphology of a crystal. It remains true that the equilibrium form of a crystal is controlled exclusively by the atomic structure of the material, and largely by the arrangement of the constituent atoms in 3D space. Therefore, the external morphology of a mineral (particularly one that is chemically simple) can be relatively accurately predicted simply by knowing the unit-cell parameters of the material.

### 1.1.2 Structure & Polymorphism of NiS

Two forms of NiS are known:  $\alpha$ -NiS and  $\beta$ -NiS both occur naturally as minerals, the polymorphs being related by a reconstructive  $\alpha \rightarrow \beta$  phase transition that occurs at 379 °C (Wang 2005a).

Millerite ( $\beta$ -NiS) is the geologically dominant form of NiS, and occurs frequently as a low-temperature precipitate through hydrothermal activity (Young 2011) or as an alteration product of earlier Ni-bearing minerals (Fin'ko & Mohkov 1985). Millerite is also present generally as an accessory mineral in magmatic Cu-Ni-PGE deposits (Ames *et al.* 2008), but concentrations can develop that have important economic significance (Graterol & Naldrett 1971). As millerite represents the low-temperature form of NiS, it is expected to be the most widespread form in carbonate basins and other hydrothermal systems, as these generally develop under low-temperature conditions (*i.e.*, < 250 °C). Millerite crystallizes in the space group  $R\bar{3}m$  (No. 160) with hexagonal axes  $a = 9.607(1)$  Å and  $c = 3.143(1)$  Å and  $Z = 9$ . All atoms occupy Wyckoff position  $9b$  ( $x, \bar{x}, z$ ) where  $x_{\text{Ni}} = 0.91225(9)$ ,  $z_{\text{Ni}} = 0.4755(10)$ ,  $x_{\text{S}} = 0.11224(19)$ , and  $z_{\text{S}} = 0$  (Grice & Ferguson 1974). The crystal structure of millerite is layered along [0001] and contains six stepped overlapping layers of alternating Ni and S atoms within each unit cell (Fig. 1.1a). Ni atoms are in 5-fold coordination with S atoms giving rise to a tetragonal pyramid. In turn, S atoms are in 5-fold coordination with Ni atoms located at the vertices of a tetragonal pyramid

(Rajamani & Prewitt 1974). Three NiS<sub>5</sub> tetragonal pyramids are linked through shared edges to form a Ni<sub>3</sub>S<sub>9</sub> cluster (Gibbs *et al.* 2005) (Fig. 1.1c). The crystal structure exhibited by millerite is quite rare, and the only other known mineral to crystallize with the same structure is mäkinenite, NiSe (Vuorelainen *et al.* 1964).

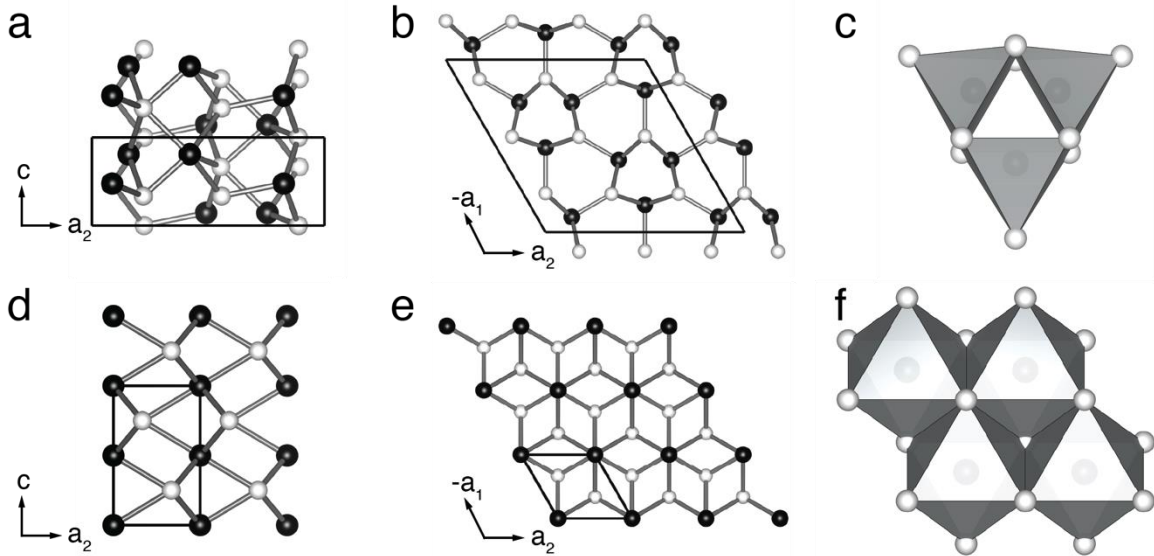


**FIG. 1.1.** Crystal structures of the two NiS polymorphs. The Ni atoms are shown in black and S atoms in white. Both materials are drawn with hexagonal axes, and unit-cell edges are given in black lines. (a) The crystal structure of millerite ( $\beta$ -NiS) projected along  $[10\bar{1}0]$ . Note the layered-like appearance resulting from the offset Ni and S atoms. (b) The crystal structure of millerite projected along  $[0001]$ . (c) Coordination polyhedra in millerite as edge-sharing tetragonal pyramids forming Ni<sub>3</sub>S<sub>9</sub> clusters. Ni atoms are located inside the pyramids, whereas S atoms are located at the vertices. (d) The crystal structure of crowningshieldite ( $\alpha$ -NiS) projected along  $[10\bar{1}0]$ , again note the stacked layers of Ni and S atoms. (e) The crystal structure of crowningshieldite projected along  $[0001]$ . (f) Coordination polyhedra in crowningshieldite as edge-sharing octahedra. The Ni atoms are located at the centre of the octahedra, whereas S atoms are at the vertices.

The natural form of  $\alpha$ -NiS, crowningshieldite, was only recently discovered to occur naturally as inclusions within a type IIa diamond from Letseng mine, Lesotho (Smith *et al.* 2018). Previously it was only known from studies on synthetic analogues. It crystallizes in the space group  $P6_3/mmc$  (No. 194) with  $a = 3.44(1)$  Å and  $c = 5.36(1)$  Å and  $Z = 2$  (Smith *et al.* 2018). It adopts the NiAs structure type where Ni atoms occupy Wyckoff position  $2a$   $(0,0,0)$  and  $(0,0,\frac{1}{2})$ .

while S atoms occupy position  $2c$  ( $\frac{1}{3}, \frac{2}{3}, \frac{1}{4}$ ) and ( $\frac{2}{3}, \frac{1}{3}, \frac{3}{4}$ ) (Vaidya 1976). Ni atoms are in 6-fold coordination with S atoms located at the corners of an octahedron. These polyhedra share edges to form an infinite 3-dimensional framework of NiS<sub>6</sub> octahedra (Fig. 1.1f). This structure is substantially different than that of millerite, although it can also be described as layered along [0001] reflected again by alternating layers of offset Ni and S atoms (Fig. 1.1d). The packing efficiency exhibited by this structure is superior to that of the millerite ( $D_{\text{csd}} = 5.87 \text{ g/cm}^3$ ,  $D_{\text{mlr}} = 5.37 \text{ g/cm}^3$ ), and may help to explain why the  $\alpha$ -type structure is so common in nature (and generally amongst crystalline inorganics) whereas the  $\beta$ -type is quite rare. The  $\alpha$ -NiS polymorph is stable above 379 °C, but is quenchable and thus may exist as a metastable phase below this temperature. Data from previous studies (Wang *et al.* 2006), and this current one indicate that  $\alpha$ -NiS may persist as a metastable phase for several years. While  $\alpha$ -NiS is generally believed to crystallize in the space group  $P6_3/mmc$ , previous studies indicate a metal to semimetal transition that occurs at -9 °C (Sparks & Komoto 1963), coinciding with a change in symmetry wherein  $\alpha$ -NiS adopts the non-centrosymmetric space group  $P6_3mc$  (No. 186) instead. Here, Ni atoms continue to occupy the  $2a$  site, but with S relocated to the  $2b$  site ( $\frac{1}{3}, \frac{2}{3}, z$ ) and ( $\frac{2}{3}, \frac{1}{3}, z$ ) (Trahan *et al.* 1970). However, as this structural change is minor and it does not influence the dimensions of the unit cell, it is not anticipated that this will have a profound effect on the external morphology of resultant crystals.

As NiS is a dimorph (*i.e.*, may exist as one of two structure types), it is an excellent candidate on which to evaluate the anticipated effects of growth-rate anisotropy through the application of The Law of Bravais. It is a chemically simple compound, consisting of only two entities, and the two polymorphs exhibit relatively simple structures with a high degree of symmetry, meaning that there are few crystallographically unique atomic sites. Finally, the contrasting axial ratios between  $\alpha$ -NiS and  $\beta$ -NiS (1.556 and 0.327, respectively) predict a pronounced morphological difference for resultant crystals based on the interplanar spacing.

The first case to be considered is millerite ( $\beta$ -NiS), given that it is the most common form of NiS in geological environments. Millerite has hexagonal unit-cell dimensions  $a = 9.607(1) \text{ \AA}$  and  $c = 3.143(1) \text{ \AA}$ , which implies that  $d_{0001} < d_{10\bar{1}0}$ . Considering these parameters, The Law of Bravais predicts that unit cells will be added faster along [0001]. In a small crystal ( $\leq 1 \text{ \mu m}$ ), it would be predicted that the pinacoid {0001} would dominate over the prism {10 $\bar{1}$ 0}, leading to the crystals exhibiting a platy morphology. However, as the crystal develops to a suitably large size ( $\geq 1 \text{ \mu m}$ ), the relative growth rates would cause a reversal in the relative dominance of the two forms, *i.e.*, prism {10 $\bar{1}$ 0} > pinacoid {0001}, which in turn would be expected to produce a crystal with a prismatic, or acicular morphology (Fig. 1.2a). The latter is precisely what is observed in the vast majority of millerite occurrences worldwide where millerite occurs as very elongated, slender needles with length-to-width ratios >20, and in turn suggests that The Law of Bravais is upheld in a general sense. However, millerite that develops in magmatic environments, such as those found in Sudbury, typically develop in large (cm-scale) cleavable masses wherein individual crystals develop with a pronounced platy morphology. Since the measured unit cell dimensions of material from these occurrences are consistent with those of millerite, the relationship  $d_{0001} < d_{10\bar{1}0}$  still holds, the implications being that The Law of Bravais is violated.

The second case to be considered is that of crowningshieldite ( $\alpha$ -NiS), which has the unit-cell dimensions  $a = 3.44(1)$  and  $c = 5.36(1) \text{ \AA}$ , meaning that  $d_{0001} > d_{10\bar{1}0}$ . For these dimensions, The Law of Bravais predicts that unit cells will be added faster along [10 $\bar{1}$ 0]. In a small crystal ( $\leq 1 \text{ \mu m}$ ), it would be predicted that the prism {10 $\bar{1}$ 0} would dominate over the pinacoid {0001}, leading to the crystals exhibiting a prismatic morphology. However, as the crystal develops to a suitably large size ( $\geq 1 \text{ \mu m}$ ), the relative growth rates would cause a reversal in the relative dominance of the two forms, *i.e.*, pinacoid {0001} > prism {10 $\bar{1}$ 0}, which in turn would be expected to produce a crystal with a platy morphology (Fig. 1.2b). Unfortunately, only anhedral crystals of crowningshieldite are noted to exist, none showing any type of pronounced

morphology. Therefore, no definitive statement can be made as to whether the Law of Bravais is upheld amongst naturally occurring material.

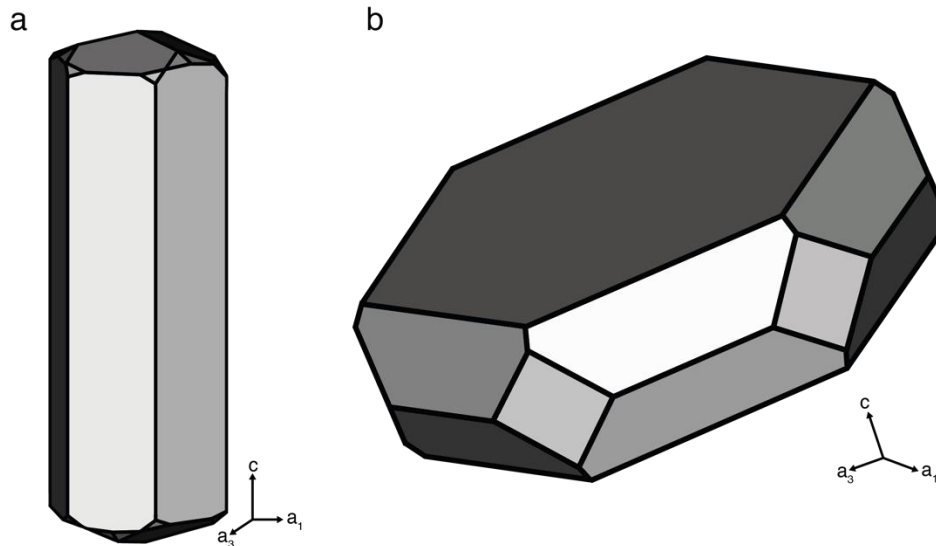


**FIG. 1.2.** Idealized 3D models of NiS crystals illustrating the common forms of the two polymorphs of NiS. (a) Millerite ( $\beta$ -NiS) often occurs as prismatic to acicular crystals elongated along  $[0001]$  where the prism  $\{10\bar{1}0\}$  is the dominant form (Goldschmidt 1920). (b) Hypothetical crystal of crowningshieldite ( $\alpha$ -NiS) drawn based on crystal chemical similarities with nickeline (NiAs) where crystals are flattened along  $[0001]$  and exhibit a platy habit with a dominant pinacoid  $\{0001\}$  (after Goldschmidt 1920).

It is interesting to note that the morphology of millerite from magmatic environments (such as Cu-Ni-PGE footwall veins in the Sudbury area) has a distinctive platy morphology, *i.e.* pinacoid  $\{0001\} >$  dipyrmaid  $\{10\bar{1}0\}$ . This is precisely the morphology that would be predicted for a large crystal of crowningshieldite ( $\alpha$ -NiS) based on the Law of Bravais.

### 1.1.3 Phase Equilibrium

In order to better understand the conditions under which NiS forms in nature, a discussion of the experimental data pertaining to the Fe-Ni-S, Fe-Ni-Cu-S, and Ni-S systems needs to be considered.

#### 1.1.3.1 THE FE-NI-S TERNARY SYSTEM

Within the Fe-Ni-S system, the first phase to develop is the *monosulphide solid-solution* (Mss), and it does so at 1192 °C (Kullerud *et al.* 1969). This phase adopts a pyrrhotite-like crystal

structure, and exhibits a wide range in both  $Me:S$  and  $Fe:Ni$  values. The  $Mss$  appears first on the Fe-S join, and the  $Fe:Ni$  value decreases with decreasing temperature as the compositional field of  $Mss$  approaches the Ni-S join. Simultaneously, vaesite ( $NiS_2$ ) appears along the Ni-S join at  $\sim 1000$  °C. Below 992 °C the compositional field of  $Mss$  spans the Fe-S and Ni-S joins, effectively dividing the system into S-rich and S-poor regions (Fig. 1.3a). The emergence of the ternary *heazlewoodite solid-solution* ( $H_{z_{ss}}$ ) with the composition  $(Ni,Fe)_{3\pm x}S_2$  occurs at 862 °C with the solubility of Fe in this compound decreasing rapidly upon further cooling and by 806 °C this compound is stable along the Ni-S join (Vaughan & Craig 1978). At 650 °C, the liquid field in the lower portion of the system has retreated towards the Ni-S join, and subsequently disappears at 635 °C (Fig 1.3b) (Kullerud *et al.* 1969). Below 610 °C, a reaction between  $Mss$  and  $H_{z_{ss}}$  results in the stabilization of pentlandite,  $(Fe,Ni)_9S_8$ , in the central portion of the S-poor region. Godlevskite,  $Ni_9S_8$ , appears along the Ni-S join at 573 °C, and at 556 °C heazlewoodite,  $Ni_3S_2$ , inverts and separates from  $H_{z_{ss}}$ , stabilizing along the Ni-S join. However, the coexistence of heazlewoodite with the rest of the system is prohibited by the surrounding compositional field of  $H_{z_{ss}}$  (Kitakaze *et al.* 2011). At 550 °C  $Mss$  still spans the Fe- and Ni-S joins (Fig. 1.3c). The compositional field of pentlandite begins to spread laterally as temperatures decrease, allowing for greater variation in the  $Fe:Ni$  values, but the S content remains relatively unchanged. At 400 °C, the  $Mss$  field continues to span the width of the system, but has narrowed to a more constrained  $Me:S$  content (Fig 1.3d). At 356°C the binary phase polydymite  $Ni_3S_4$  appears along the Ni-S join. The  $Mss$  field continues to narrow upon further cooling, and separates from the Ni-S join at 273 °C, retreating rapidly towards the Fe-S join (Fig. 1.3e) (Vaughan & Craig 1978). This allows millerite ( $\beta$ - $NiS$ ) to finally stabilize along the Ni-S join. Below 250 °C, the lateral expanse of the pentlandite compositional field narrows, and at 130 °C it is the only S-bearing phase exhibiting a significantly variable chemistry present in the system (Fig. 1.3f).

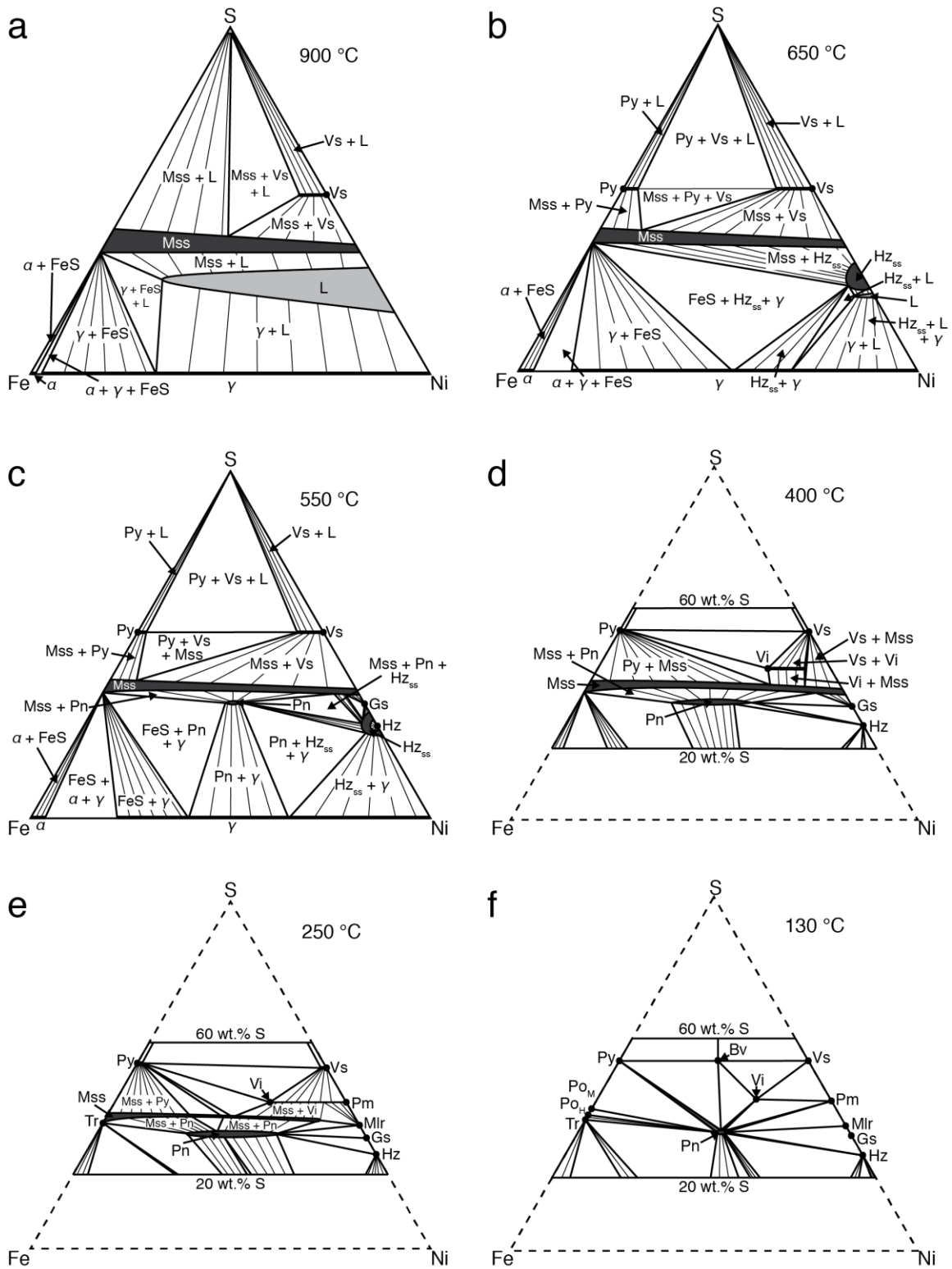


**FIG. 1.3.** Ternary diagram illustrating equilibrium in the Fe-Ni-S system (redrawn from Kullerud & Yund 1969, and Vaughan & Craig 1997). See text for details.

### 1.1.3.2 THE FE-NI-CU-S QUATERNARY SYSTEM

Information pertaining to phase relations in the Fe-Ni-Cu-S quaternary system is generally based on extrapolations from the Fe-Ni-S, Cu-Fe-S, and Cu-Ni-S subsystems. Of particular importance to this study are the effects of Cu on the phase relations and stability fields of Ni-bearing minerals and compounds as millerite is often observed in Cu-Ni-PGE veins in the Sudbury area.

As was observed in the Fe-Ni-S system, Mss is the earliest forming solid phase and does so at approximately 1200 °C. Similarly, it first emerges on the Fe-S join and extends towards the Ni-S join upon further cooling, forming a complete solid solution between  $\text{Fe}_{1-x}\text{S}$  and  $\text{Ni}_{1-x}\text{S}$  by approximately 1000 °C. Despite spanning the Fe-Ni continuum, Mss contains only limited concentrations of Cu, but a reaction between Mss and the residual sulphide liquid at 960 °C stabilizes the *intermediate solid-solution* (Iss) in the central portion of Fe-Cu-S space, which expands rapidly upon further cooling (Kullerud *et al.* 1969). At approximately 850 °C,  $\text{Hz}_{\text{ss}}$  appears the Ni-S join, and stabilizes along this boundary by approximately 800 °C. The *bornite solid-solution* ( $\text{Bn}_{\text{ss}}$ ) also coexists with the previously described phases at this temperature. In addition to these four ternary phases, a quaternary solid solution exists between Iss and  $\text{Hz}_{\text{ss}}$ , and is referred to as the *heazlewoodite-intermediate solid-solution* (Hz-Iss) (Peregoedova & Ohnenstetter 2002). It is a non-quenchable phase that stabilizes through a reaction between Mss and sulphide liquid at approximately 850 °C (Fleet & Pan 1994). The precise temperature at which Hz-Iss initially crystallizes is a direct function of the Cu content of the system, forming between 873 and 795 °C for Cu-poor systems, and between 908 and 877 °C for Cu-rich systems (Peregoedova & Ohnenstetter 2002). At 760 °C, Hz-Iss represent a complete solid solution between Mss and Iss that coexists with the four ternary phases Mss, Iss,  $\text{Hz}_{\text{ss}}$ , and  $\text{Bn}_{\text{ss}}$  in addition to vaesite ( $\text{NiS}_2$ ), S liquid, and an Fe-Cu-Ni alloy within the Fe-Ni-Cu-S tetrahedron (Fig. 1.4).

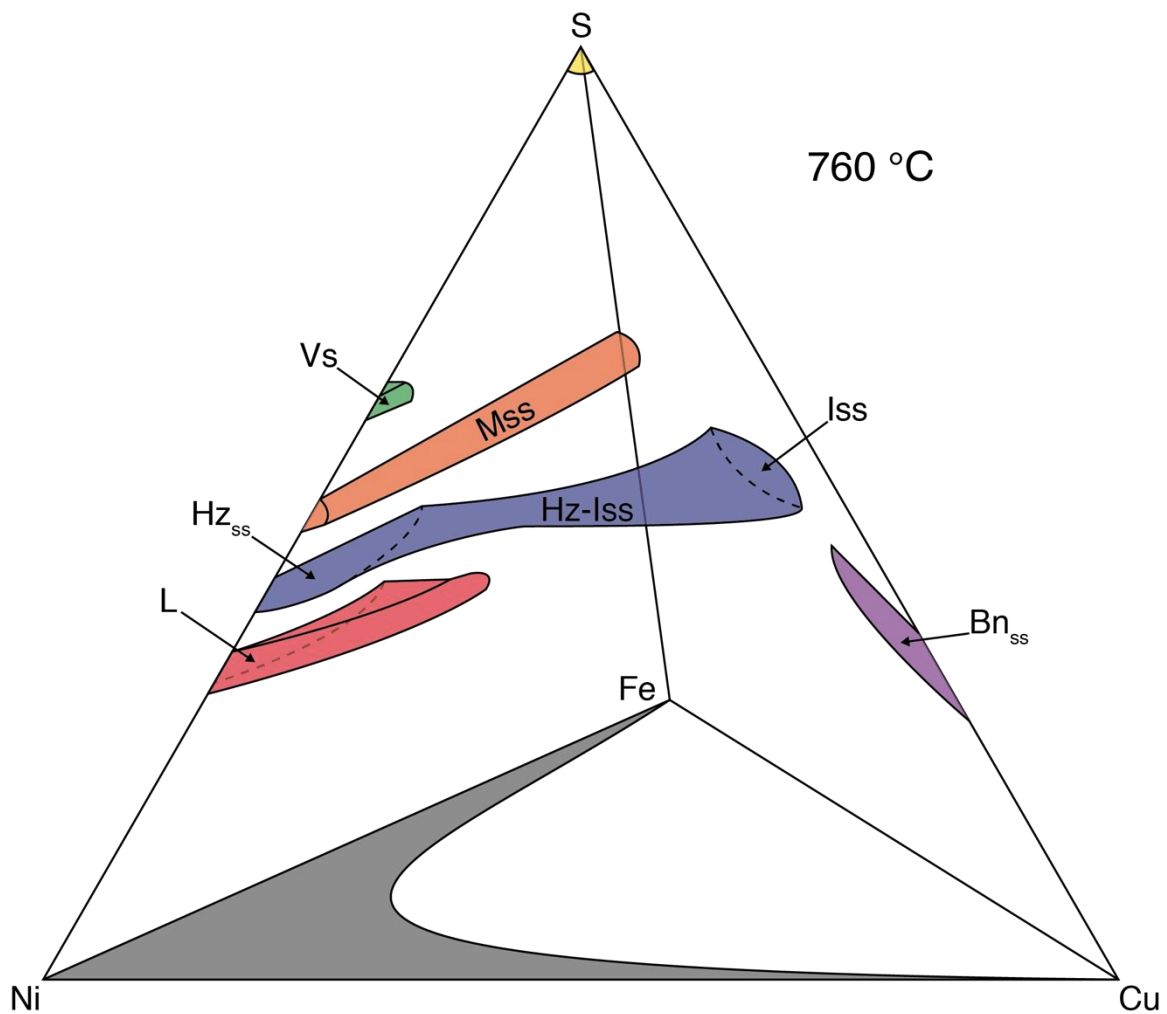


**FIG. 1.4.** Compositional fields in the Fe-Ni-Cu-S quaternary system at 760 °C (redrawn from Peregodova & Ohnenstetter 2002).

The presence of this Hz-Iss phase spanning Fe-Ni-S and Fe-Cu-S space is significant as it provides a repository for Ni in Cu-rich systems from which later Ni-sulphides may crystallize. Little work has been conducted on the phase relations in the Fe-Ni-Cu-S system below 760 °C, and therefore the temperature at which subsequent process occur and the stable assemblages during cooling of the system can only be inferred based on extrapolation from the relevant subsystem, and observations of natural systems. However, it has been proposed that the development of Hz-Iss may have a significant impact on the formation of Cu-rich systems such as those present in the Sudbury area and in Noril'sk (Fleet & Pan, 1994).

### 1.1.3.3 THE Ni-S BINARY SYSTEM

While complete details from high-temperature to low-temperature in the Ni-rich portion of the Fe-Ni-Cu-S system remain poorly constrained, those specifically pertaining to the phase relations in the Ni-S system have been well studied and are better understood. As this study is focused on the formation of millerite, further discussion of the Ni-S system will be constrained to the region between ~32 to 37 wt. % S.

Initial crystallization of  $\alpha$ -NiS can begin at temperatures as high as 1000 °C (in a pure Ni-S system), but considering natural systems and the phase relations presented in the previous sections, it likely develops as a discrete phase at much lower temperatures, possibly around 500 °C following separation from either Mss or Hz-Iss. The composition of the melt exerts significant control over the stability of  $\alpha$ -NiS, which is stable above 379 °C for melts between ~32 and 35 wt. % S, but for concentrations between 35 and 37 wt. % S may persist as a stable phase to temperatures as low as 282 °C, at which point it inverts to  $\beta$ -NiS (millerite) (Fig. 1.5).

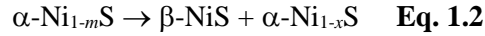
Furthermore,  $\alpha$ -NiS crystallizes in the space group  $P6_3/mmc$ , and similar to the Fe-analogue (pyrrhotite)  $\alpha$ -NiS may exhibit a non-stoichiometric formula, and is thus expressed as  $\alpha$ -Ni<sub>1-x</sub>S. While the upper limit of this metal deficiency has not been precisely determined ( $\geq 0.1$ ), it is known to have a significant impact subsequent phase transformations (Wang *et al.* 2006).

Stoichiometric  $\alpha$ -NiS inverts to  $\beta$ -NiS at 379 °C (Fig 1.5) where the reaction is simple, and proceeds in a congruent manner as:



However, as the structure of  $\alpha$ -NiS can accommodate a greater degree of metal deficiency than that of  $\beta$ -NiS, if the starting composition of the material is non-stoichiometric, then the  $\alpha \rightarrow \beta$  inversion must be accompanied by the exsolution of an increasingly metal deficient

$\alpha$ -Ni<sub>1-x</sub>S compound (Kullerud & Yund 1962). This process is represented by the following chemical equation as:



Furthermore, the activation energy ( $E_a$ ) of the transition exhibits a marked increase for Ni-deficient  $\alpha$ -Ni<sub>1-x</sub>S. The  $E_a$  for stoichiometric  $\alpha$ -NiS ranges from 13.0(5) kJ/mol at 350 °C, to 16.0(5) kJ/mol at 70 °C. Conversely, the  $E_a$  for the Ni-deficient composition of Ni<sub>0.97</sub>S is much greater at 73.0(5) kJ/mol at 320 °C, and is expected to be higher at lower temperatures suggesting sluggish reaction rates and greater metastability with increasing metal deficiency (Wang *et al.* 2006).

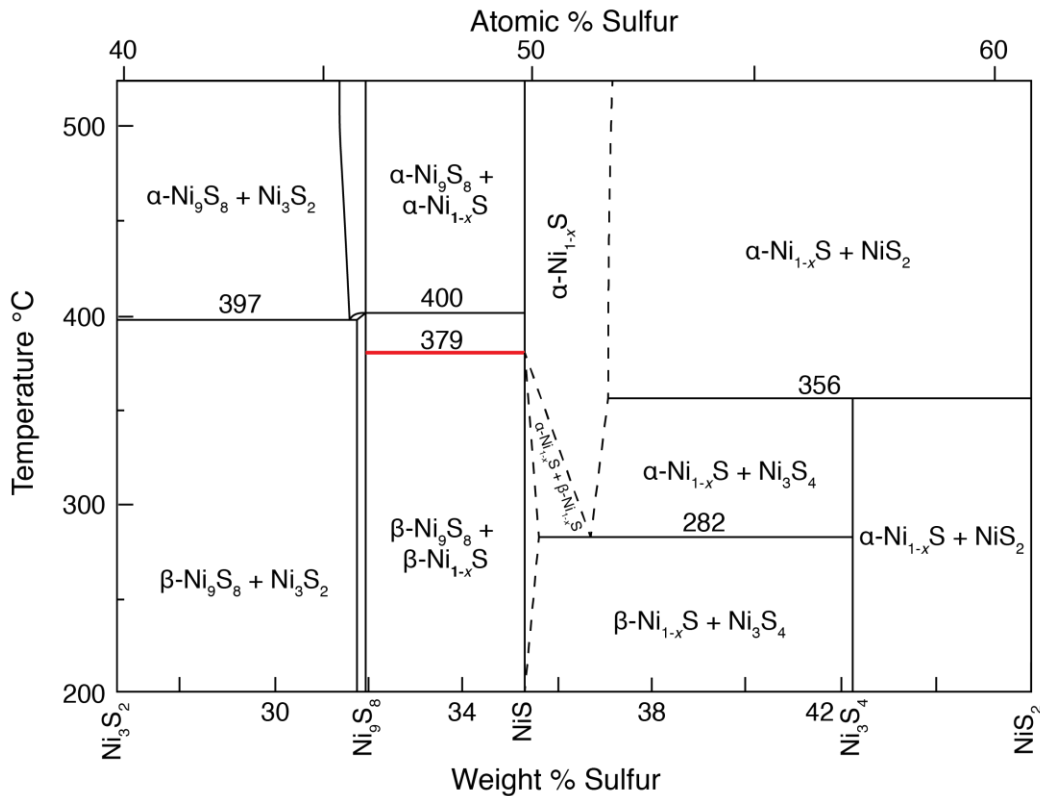


**FIG. 1. 5.** Phase diagram of the Ni-S system. The partial section represents the regions relevant to the formation of NiS. The  $\alpha \rightarrow \beta$  transition occurs along the horizontal boundary outlined in red at 379 °C (redrawn from Kullerud & Yund 1962).

Regardless of the starting composition of  $\alpha$ -NiS,  $\beta$ -NiS generally shows very little in the way of metal deficiency ( $\sim 0.01$  apfu) and for all intents and purposes should be considered stoichiometric (Kullerud & Yund 1962). The  $\alpha \rightarrow \beta$  phase transition is reconstructive, *i.e.* a process that involves the breaking and reforming of chemical bonds. This transformation also involves a change in the coordination of Ni, going from [6] in  $\alpha$ -NiS to [5] in  $\beta$ -NiS, a feature reflecting the fact that changes in the bonding character between the two polymorphs must be involved (Fig. 1.6) (Wang 2005b). This structural reorganization also results in a reversal of the unit-cell edges where  $a > c$  in  $\alpha$ -NiS, but  $a < c$  in  $\beta$ -NiS, and is accompanied by a unit cell expansion of 1.78 %. It is also noteworthy that this transition takes place readily between 150 and 379 °C, with the reaction reaching completion in a matter of hours (even for non-stoichiometric material (Wang *et al.* 2006). Furthermore, the low  $E_a$  for stoichiometric  $\alpha$ -NiS allows the reaction to take place even under ambient conditions. This has also been observed to occur for Ni-deficient  $\alpha$ -NiS, providing the initial energy barrier is overcome (Wang *et al.* 2006).

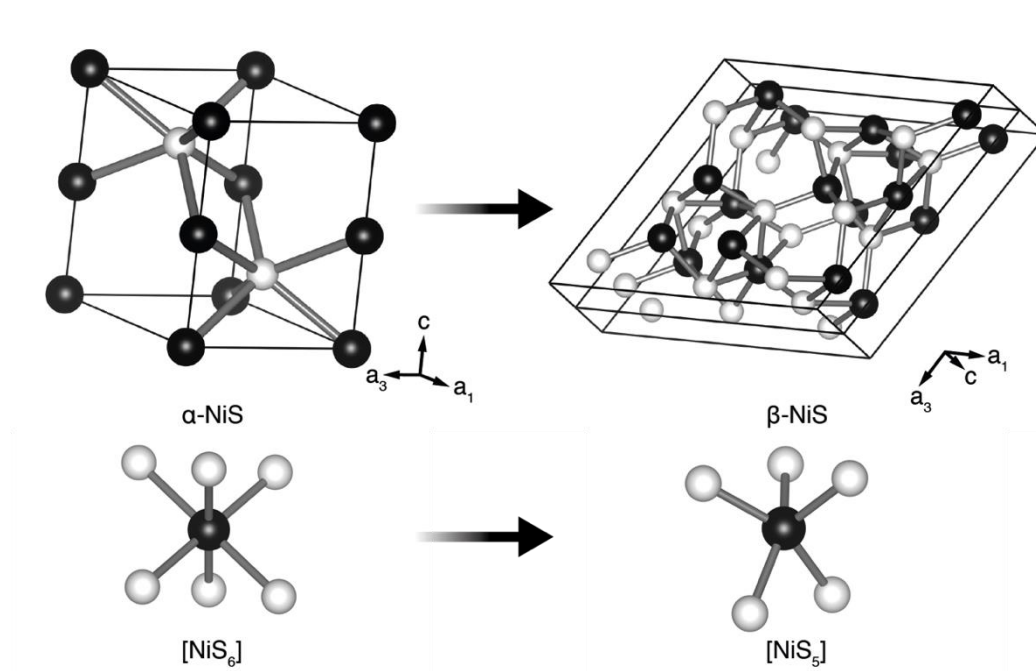


**FIG. 1.6.** Changes in the atomic structure of NiS during the  $\alpha \rightarrow \beta$  transition. The Ni atoms (black) are in [6] coordination with S (white) in  $\alpha$ -NiS, but are rearranged into [5] coordination in  $\beta$ -NiS (after Wang *et al.* 2006).

For these reasons, it is considered highly unlikely that  $\alpha$ -NiS would be expected to persist outside of its predicted stability field for any prolonged period. Certainly, on the geological time scale, which may range from millions to billions of years, any  $\alpha$ -NiS that initially crystallized under high-temperature conditions would naturally be expected to have completely inverted to  $\beta$ -NiS, *i.e.*, natural examples of a mineral corresponding  $\alpha$ -NiS would not be expected to be found, except under exceeding unusual geological occurrences or in extremely young rocks.

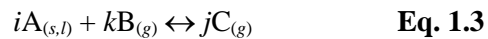
It is for this reason that millerite is so common and  $\alpha$ -NiS as a mineral had not been discovered until recently. It is quite interesting that the first discovery of crowningshieldite was made based on inclusions trapped within a diamond, the latter mineral known for its high resistance to chemical and physical weathering, as well as persistent metastability outside of the diamond stability field (*i.e.* ambient conditions), but also its development under very high pressure (12 to 25 GPa) (Smith *et al.* 2016). The effects of pressure on the stability of NiS have been examined by Sowa *et al.* (2004), indicating that the stability field of  $\alpha$ -NiS expands significantly with increasing pressure, up to the point where it may remain stable even under ambient conditions at the pressures at which the diamonds are suggested to have formed. While the exact reason that  $\alpha$ -NiS was stabilized within the diamond remains unknown, certainly the role of confining pressure must be considered as potentially playing an important role.

#### 1.1.4 Synthesis of $\alpha$ -NiS

As the only known samples of crowningshieldite are extremely small (~50  $\mu\text{m}$ ) and anhedral, it was not possible to evaluate the morphological features of this material. Since no morphological information could be derived from these crystals, and as one of the key goals of this study was to investigate the impact of growth-rate anisotropy on the morphology of both polymorphs of NiS, a series of experiments designed to synthesize  $\alpha$ -NiS were conducted. The primary goal was to produce euhedral crystals of  $\alpha$ -NiS and secondarily, to investigate the impact of growth-rate anisotropy on the morphology of both polymorphs of NiS. A variety of synthesis

methods were considered taking into account the following conditions: (1) Crystallization would occur at temperature  $>400$  °C to ensure that all NiS present in the system forms as  $\alpha$ -NiS; (2) the chemistry of the system would be strictly regulated so a polymineralic product is not formed; and (3) the resultant crystals must be euhedral such that analysis of their morphology could be conducted. Ultimately, chemical-vapour transport (CVT) was selected as: (1) it fit the above criteria; (2) did not require excessive growth periods; and (3) permitted the use of natural millerite as a starting reagent. The final point was considered to be important as it allowed for a more direct comparison between the synthetic crystals and natural systems and permitted the observation of how Fe and Co may substitute in  $\alpha$ -NiS.

Chemical vapour transport is a crystal growth technique that involves a series of chemical reactions in which a solid or liquid precursor (A) reacts with a gas (B) to form a gaseous complex (C), which then migrates to a different location in the system wherein the redeposition of A is favoured (Fig. 1.7). This process is described by the reversible general reaction (Schäfer 1964):



The use of the gas (B) as a *transport reagent* is typically required to volatilize the reactants as these generally do not possess sufficient vapour pressure, under the desired physical conditions to spontaneously form a gas (Binnewies *et al.* 2013). Additionally, in order to facilitate the transport of the gaseous complex, a compositional gradient must be established in the system. This can be achieved by creating a temperature gradient across the system, wherein the reagents are volatilized at one temperature and then redeposited at another (Binnewies *et al.* 2012). The use of the symbols  $T_1$  and  $T_2$  are universally used to define the two temperature regions in the system, with  $T_1$  representing the lower value and  $T_2$  representing the higher one. The temperature difference between the two zones varies depending on the desired reaction, but is generally between 50 and 300 °C for inorganic materials. Furthermore, the notation  $T_2 \rightarrow T_1$  also denotes a

transport towards the cooler zone (Schäfer 1964). These experiments are generally conducted in evacuated silica capsules, where the amount and type of transport reagent that may be utilized is variable, but typically are selected so as to produce an internal capsule pressure of approximately 1 atm when the system is brought up to the desired temperature (Schmidt *et al.* 2013).

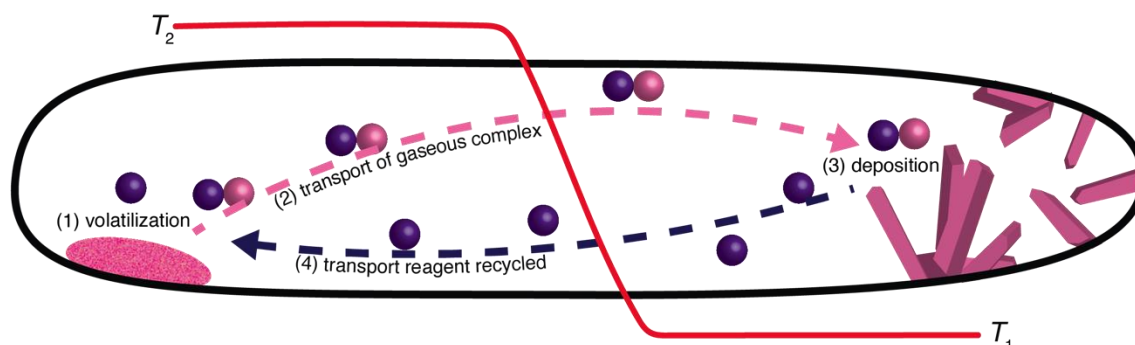


**FIG. 1.7.** Schematic cross section of CVT occurring within a sealed capsule. The process illustrated above is an endothermic reaction wherein the reaction proceeds  $T_2 \rightarrow T_1$ . The reactants (pink spheres) are (1) volatilized at  $T_2$  (hot zone) forming a gaseous complex with the transport reagent (purple spheres). This compound then (2) migrates across the temperature gradient where the reactants are (3) redeposited as euhedral crystals at  $T_1$  (cool zone). The transport reagent is then (4) recycled in a reverse fashion across the temperature gradient back towards the reactants and the cycle continues (after Schmidt *et al.* 2009).

### 1.1.5 Notes on Magmatic vs. Hydrothermal Millerite

A key aspect of this study was to compare and contrast millerite coming from different geological environments. Broadly speaking, these encompass two types described as *magmatic* (referring to the derivation of a melt arising from magmatic processes) and *hydrothermal* (referring to derivation from a non-magmatic precursor, such as low-temperature fluids or alteration). While the terms may not be overly definitive, they will be used for discussion purposes. The use of these terms as they apply in the context of this study is defined below.

The term *magmatic* is applied to NiS that crystallized as the product of a cooling sulphide magma. While it is understood that the system will have undergone significant re-equilibration and may have experienced interaction with hydrothermal fluids subsequent to the initial crystallization, the defining feature of this type of NiS is having been derived from a high-

temperature (>1000 °C) magmatic source, generally through phase separation from a Fe-Ni-Cu-rich sulphide melt (Hz-Iss) and its subsequent crystallization (Fleet & Pan 1994; Peregoedova & Ohnenstetter 2002; Mungall 2007). In these instances, the NiS is co-genetic with the associated primary mineral assemblage. This type of genesis is anticipated in magmatic Cu-Ni-PGE systems observed in localities such as the Sudbury area, or Fe-Ni systems such that at the Marbridge mine.

The term *hydrothermal* is applied to NiS that crystallized from a low-temperature fluid (<250 °C) containing significant Ni and S in solution (Heyl *et al.* 1959). Contrary to the occurrence of NiS in magmatic systems, this millerite is not necessarily co-genetic with the host country rock, nor is source of the Ni- and S-bearing fluid the same as for associated minerals, as they may have formed as the result of unrelated hydrothermal events. The key point being that millerite is the product of a process such as alteration or remobilization of pre-existing Ni-bearing minerals and is not the product of a crystallizing magma. This is the type of genesis proposed for the formation of millerite in sedimentary basins such as those at Halls Gap, Kentucky (Medici 1981). This description of hydrothermal NiS may also be extended to include millerite forming as the result of supergene enrichment of mafic and ultramafic system such as those described by (Fin'ko & Mohkov 1985) and (Holwell *et al.* 2017), although no such samples were examined over the course of this study.

#### *1.1.6 Sample Locations*

Geological samples representative of magmatic samples used in this study were obtained from operating mines in the Sudbury area, including Coleman (COL) (Vale; North Range) and Nickel Rim South (NRS) (Glencorp; East Range) (Fig. 1.8). A total of 85 samples were collected over several levels including the 1470 to 1740 m levels at Coleman mine and the 1200 to 1680 m levels of the Nickel Rim South mine. All were obtained from Cu-Ni-PGE veins hosted in the footwall of the Sudbury Igneous Complex (SIC), these being considered as products of fractionated Hz-Iss that was injected into mafic and felsic gneisses that constitute the footwall

environment. All can be described as narrow-vein sulphides ranging from 30 to 100 cm in width (Fig. 1.9) that are dominated by chalcopyrite and millerite with lesser pyrrhotite, pentlandite, bornite, magnetite, and a host of trace constituents. Detailed descriptions of the samples are provided below in section 1.3.

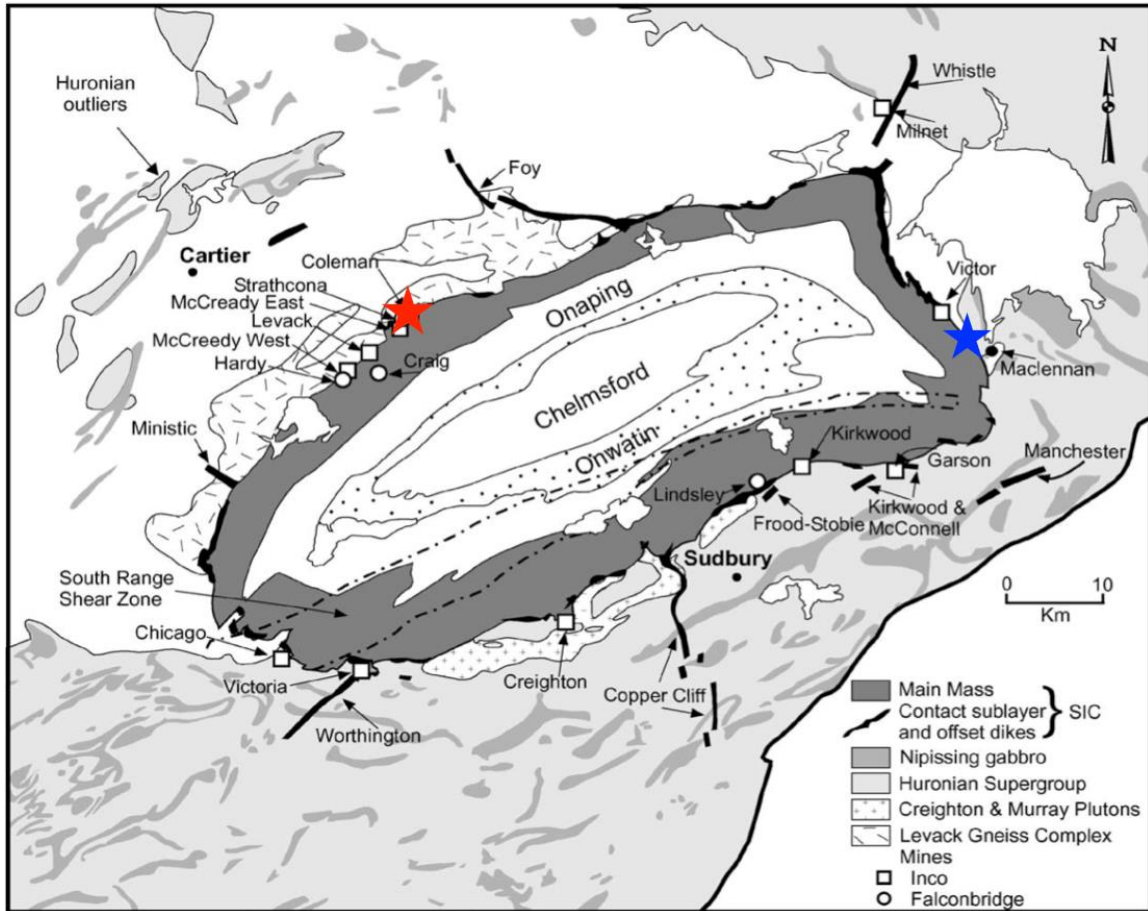


**FIG. 1.8.** Plan view map of the Sudbury Basin showing the locations of some major mines including Coleman mine (red star) and Nickel Rim South mine (blue star) (after Rousell *et al.* 2003).

Supplementing these is an additional suite of six samples from various occurrences of hydrothermal millerite worldwide. All of these samples are interpreted as late-stage precipitates crystallizing within vugs in sedimentary basins. The localities for all samples along with additional information regarding their occurrences are presented in Table 1.1.

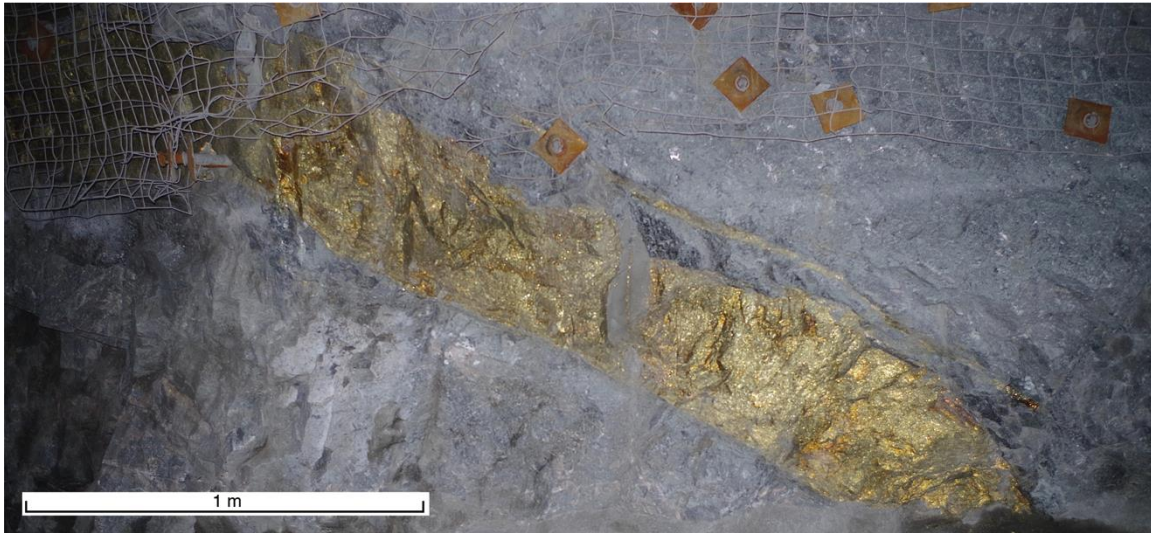


**FIG. 1.9.** Massive sulphide vein underground at the 1740 m level of Coleman mine consisting primarily of chalcopyrite and millerite (~10:1 abundance). This is the typical of vein style Cu-Ni-PGE mineralization present in the footwall environment of the Sudbury area.

**Table 1.1: Information Relating to Millerite Examined**

Locality	Total No. of Samples	Depth Collected (m)	Origin
Nickel Rim South Mine (Sudbury, Ontario, Canada)	48	1200 to 1600	Magmatic
Coleman Mine (Sudbury, Ontario, Canada)	37	1470 to 1740	Magmatic
Morrison Deposit (Sudbury, Ontario, Canada)	5	1250 to 1400	Magmatic
Dumbarton Mine, Bird River (Manitoba, Canada)	1	Unknown	Hydrothermal
Halls Gap (Kentucky, USA)	1	Surface	Hydrothermal
Gap Mine (Pennsylvania, USA)	1	Surface	Hydrothermal
Orford Nickel Mine (Québec, Canada)	1	Unknown	Hydrothermal
Sterling Mine (New York, USA)	1	Surface	Hydrothermal
Pafuri Deposit (Northern Transvaal, South Africa, Africa)	1	Unknown	Hydrothermal

Terms regarding origin are defined using the criteria outline in section 1.1.5. See Appendix D for a comprehensive list of samples.

## 1.2 METHODS

### 1.2.1 Chemistry

Chemical data were collected using a JEOL-6400 scanning electron microscope (SEM) with a PMT-based detector *via* energy-dispersive spectroscopy (EDS) with an accelerating voltage of 20 kV, and a current of 1.0 nA. Standards that were employed (line used) include chalcopyrite ( $\text{FeK}\alpha$ ,  $\text{CuK}\alpha$ ,  $\text{SK}\alpha$ ), Ni wire ( $\text{NiK}\alpha$ ), and Co wire ( $\text{CoK}\alpha$ ). Only Ni, Fe, Co, and S were analyzed for, as no other elements were detected in preliminary scans. Data acquisition and processing were facilitated using INCA analytical software (Oxford Instruments 2011). The points for which EDS data were collected were obtained from line scans with an average lengths of  $\sim 150\ \mu\text{m}$ , a beam diameter of  $\sim 5\ \mu\text{m}$ . A carbon coat was applied to all polished sections prior to analysis *via* SEM-EDS.

### 1.2.2 CVT Synthesis

Crystals of  $\alpha$ -NiS were synthesized using chemical-vapour transport (CVT) in evacuated silica capsules with an internal diameter of 7 mm and a length of approximately 20 cm. Three such experiments were conducted with the precise parameters for each individual experiment being listed in Table 1.2.

The starting reagent was natural millerite collected from Coleman mine the with the average chemical composition  $(\text{Ni}_{0.976}\text{Fe}_{0.013}\text{Co}_{0.003})_{\Sigma 0.992}\text{S}$ . Natural millerite was used as opposed to sintered NiS for simplicity, accessibility, and given that it is a more accurate analogue with which to portray the chemical composition of NiS in a natural system. Furthermore, while this material contains Ni, Fe, and Co, the total Fe+Co is minimal, and the composition is very near end-member NiS. Seeding material was extracted from a polymineralic massive sulphide samples consisting primarily of millerite (80%), with subordinate chalcopyrite (18%) and pentlandite (2%). It was crushed to a visually estimated grain size of  $<250\ \mu\text{m}$ . Pure, crystalline  $\text{I}_2$  (99.9%; Alfa Aesar) was used as the transport reagent. The crushed millerite and  $\text{I}_2$  crystals were placed in

a silica capsule, which was then evacuated and sealed with an oxyacetylene torch. The section of the tube containing the millerite and  $I_2$  was cooled with liquid nitrogen during the sealing process to prevent premature volatilization and loss of the  $I_2$ . The capsules were positioned in a horizontal tube furnace with a temperature gradient of approximately 100 °C over ~20 cm, with the charge in the hot end of the furnace. Experiments were conducted over a variable period between 12 and 45 days. Following the termination of the growth period, the capsules were removed from the furnace and immediately quenched in cold water.

**Table 1.2: Parameters for CVT Synthesis**

<b>Parameters</b>	<b>Run No. 1</b>	<b>Run No. 2</b>	<b>Run No. 3</b>
<b>Temperature (°C)</b>	700 → 600	800 → 700	800 → 700
<b>*Reactant (g)</b>	1.0053	0.9231	1.3300
<b>Transp. Reagent (g)</b>	0.0267	0.0283	0.0333
<b>Sealed at (mtorr)</b>	68	69	68
<b>Duration (days)</b>	21	12	45

\*All runs used natural millerite from Coleman mine as the reactant and crystalline  $I_2$  as the transport reagent. Arrows indicate the motion of the gas from  $T_2$  to  $T_1$ .

### 1.2.3 X-Ray Diffraction

Powder X-ray diffraction (PXRD) data for material from Nickel Rim South and Coleman mines were collected using a Scintag ADS-200 diffractometer configured in Bragg-Brentano geometry using Fe-filtered  $CuK\alpha_{avg}$  ( $\lambda = 1.5418 \text{ \AA}$ ) radiation, and operating at 40 mA and 30 kV. Samples were analyzed over a range of 5 to 100° 2 $\theta$  with a step size of 0.02°, and a counting time of 4 s per step. The selected material was crushed using a hammer, and then ground into a fine powder using a steel ring mill that was cleaned between samples with soap and water. Powdered material was then placed into sample holders, and the surface flattened with a frosted glass slide.

Powder X-ray diffraction data for synthesized material were collected using a Bruker AXS Discover 8 microdiffractometer equipped with a Hi-Star 2-D area detector, using  $CuK\alpha_{avg}$  ( $\lambda = 1.5418 \text{ \AA}$ ) radiation operating at 40 mA and 40 kV, with a sample-to-detector distance of 16.0 cm. A total of six grains were mounted around the circumference of a glass filament to

ensure multiple grain orientations were presented. Data were collected over a range of 20 to 100° 2θ with a frame width of 10° and a counting time of 4 h per frame. The sample was rotated about the φ axis during exposure to maximize randomization of grain orientations.

### **1.3 OBSERVATIONS**

#### *1.3.1 Hand Samples*

Individual samples ( $n = 85$ ) ranged in size from 2.0 × 2.0 × 4.0 cm to 10.0 × 30.0 × 30.0 cm. The major sulphide mineralogy of the samples consists of chalcopyrite, millerite, pyrrhotite, pentlandite, and bornite in varying proportions, although the majority of the samples were dominated by chalcopyrite and millerite. Magnetite was also present, and observable macroscopically as euhedral octahedra up to 1 mm in diameter.

Chalcopyrite forms the bulk of the massive sulphide in the majority of the samples, accounting for >50% of the total sulphide present in a given samples, and acts as a host for the other opaque phases with the exception of bornite (Fig. 1.10a-c). It does not exhibit any physical properties beyond those characteristic for the mineral.

When present, millerite accounts for between 10 to 50 % of the total sulphide mineralogy, and two distinct textural populations are present: (1) The first, which dominates, includes millerite present as coarse, anhedral to subhedral platy crystals up to 5 cm in diameter. These crystals often form clusters that are visible as large, cleavable masses (Fig. 1.10a, d-f). The faces of these crystals display a strong, mirror-like metallic lustre. These faces converge in numerous samples, and the interfacial angles are visually estimated to approximate 60°/120°, although they were not directly measured. These angles correspond to the {10 $\bar{1}$ 1} cleavage present in millerite (Dana 1949). As such, the highly reflective faces are not true crystal faces, but rather, represent cleavage planes. Clearly visible on larger faces of these millerite crystals are parallel striations that are sharp, approximately 1 mm wide, and span the entire length of the

cleavage plane. A second, less prominent set of these lamellae is oriented approximately 20° to the dominant set. These lamellae are finer (<0.5 mm wide) and are truncated by the dominant set of lamellae, so are not continuous across the entire cleavage plane (Fig. 1.10e). (2) The second population of millerite includes that having a granular texture and a smaller average grain size of ~1 mm. These grains lack discernable faces of any kind, and neither lamellae nor cleavage are noted in any of the samples. This second population of millerite is rare, being observed only locally in samples from the two mines, and is particularly well developed in a single sample collected from the 1480 m level of Nickel Rim South mine (Fig. 1.10e).

Pyrrhotite generally comprises only a small portion of the total sulphide mineralogy, <5 modal % and occurs as veinlets ~1 cm thick in chalcopyrite (Fig. 1.10b), or as isolated blebs ranging in size from 0.5 to 2.0 cm in diameter (Fig. 1.10c). All pyrrhotite observed throughout the samples is magnetic, and is assumed to be the monoclinic polytope. It is frequently in close association with pentlandite. It is not observed to coexist in any samples with millerite.

Pentlandite generally accounts for a small portion of the total sulphide mineralogy at <5 modal %, and occurs as coarse blebs ~1.0 cm in diameter in association with pyrrhotite (Fig. 1.10c). A pervasive octahedral parting is observed, producing grains with planar surfaces, similar to those observed in millerite. The resemblance of the two minerals in hand sample (particularly under the poor lighting during underground sampling) resulted in the collection of a number of purely pentlandite samples that were initially mistaken for millerite, until they were examined more closely above ground. Collection of the pentlandite-rich samples was restricted to Coleman mine, and pentlandite was found to be extremely rare and in low concentrations (~1 modal %) at Nickel Rim South mine.

Bornite occurs as anhedral masses typically along the vein selvages. It is generally rare, representing >1 modal %. However, several samples collected from the margins of veins are composed largely or entirely of bornite (Fig. 1.10f). These samples may have also included variable proportions of chalcopyrite and/or millerite in addition to the dominant bornite.

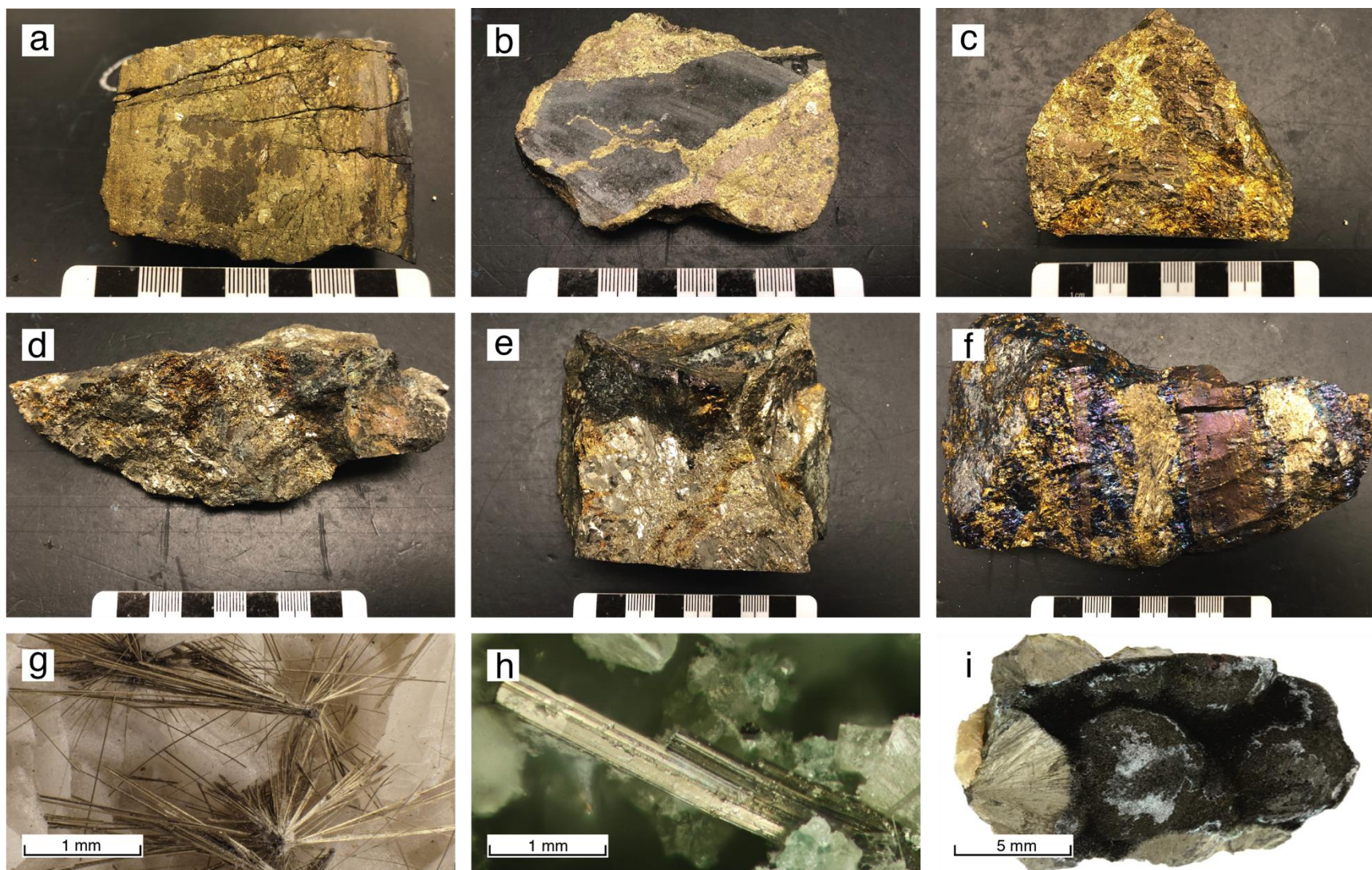


**FIG. 1.10.** Representative hand samples of mlr and associated minerals. Scale for images a-f is in cm. (a) Coarse mlr in ccp from COL (unknown depth). Individual crystals of mlr are up to 2 cm in diameter. (b) Po veins through ccp matrix from NRS (1480 m). (c) Coarse po/pn blebs in ccp matrix from COL (1740 m). (d) Coarse mlr with minor ccp from NRS (1480 m). (e) Coarse and granular mlr with minor ccp from NRS (1480 m). Note the planar cleavages face on the mlr crystals. (f) Bn-rich samples with mlr and ccp from COL (unknown depth). Note the banding of mlr-bn+ccp-mlr. (g) Acicular crystals of mlr on calcite from Dumbarton mine, Manitoba. Note that crystals are elongated along [0001] (Christophe Boutry). (h) Prismatic mlr on calcite from Orford Nickel mine, Québec. Again, note the elongation along [0001]. (i) Botryoidal clusters of mlr from Gap mine, Pennsylvania. The radiating clusters of acicular crystals are visible in cross section of the spheres (Dan & Diana Weinrich).

Representative samples of millerite representative of hydrothermal localities obtained for this study were examined using a binocular microscope at high magnification (100x). All samples consisted of isolated millerite grains in vugs containing no other visible sulphides. All of the millerite occurs as acicular crystals with exaggerated aspect ratios ( $l:w >20$ ) (Fig. 1.10g,h) that often form clusters or radiating aggregates. In some cases, the packing of individual crystals is so tight that these dense aggregates take on a botryoidal appearance (Fig. 1.10i). However, even in these cases, if a section through the sphere is observed, the fibrous habit exhibited by the individual crystals can still be observed clearly.

### 1.3.2 Reflected Light Petrography

A total of 30 polished thin sections were prepared and examined under reflected light, although only those found to contain millerite are discussed below.

The mineral assemblages for all thin section contained variable proportions of millerite and chalcopyrite, and may also include pentlandite/pyrrhotite, bornite, magnetite, galena, hessite, and gold. The paragenetic sequence, as deduced by macroscopic, optical microscopy, and electron microscopy is presented in Figure 1.11.



**FIG. 1. 11.** Idealized paragenetic sequence of millerite and associated minerals from footwall Cu-Ni-PGE footwall veins in the Sudbury area based on observations made from Coleman and Nickel Rim South mines.

Chalcopyrite forms the main mass of the vast majority of the observed thin sections. It simultaneously hosts the other phases (Fig. 1.12a-c), and is also present along fractures or at the

grain boundaries of millerite, pentlandite, and magnetite, suggesting that while the initial formation of chalcopyrite occurred early in the crystallization sequence, crystallization and possibly subsequent remobilization of the mineral continued well into the later stages of the sequence.

Millerite observed in the large majority of the thin sections occurs as coarse grains ranging in size from 0.25 to >1.0 cm in diameter (Fig. 1.12b). It is hosted within the chalcopyrite matrix, and the crystals frequently exhibit a pervasive rhombohedral  $\{10\bar{1}1\}$  cleavage. Numerous parallel lamellae that range in thickness from <1 to 350  $\mu\text{m}$  are present in a large portion of the samples, and are particularly evident in those where the grain size exceeds 1.0 cm. The lamellae exhibit a distinct pleochroism, varying between brass-yellow and bronze-yellow, under plane-polarized light (PPL), and alternatively go into extinction under cross-polarized light (XPL). These are interpreted as polysynthetic twins, and more detailed description of these lamellae is presented in Chapter 2. The samples of millerite that exhibited a granular texture when observed macroscopically were also examined in thin section. In these instances, millerite occurred as comparatively finer, equant grains that are on average 0.5 mm in diameter (Fig. 1.12e,f). These grains frequently meet at triple junctions (suggestive of recrystallization), both when adjacent to other millerite grains or chalcopyrite grains, and were generally devoid of any internal textures. The pervasive cleavage present in coarser samples was not observed, and the presence of lamellae was only rarely noted within these grains. Millerite grains exhibiting this texture also did not possess any appreciable inclusions apart from small (0.1 mm diameter) octahedra of magnetite. Consistent with macroscopic observations, this equigranular texture is only observed locally in thin section, and is not representative of the majority of millerite crystals.

Pentlandite occurs as coarse blebs ranging from 0.25 to 1.0 cm in diameter, and is hosted within chalcopyrite and millerite (Fig. 1.12a,c,h), suggesting that it crystallized before these two minerals. The grains typically show strong evidence of octahedral parting, a feature that can be induced through a volume reduction, concomitant with cooling (Ramdohr 1969). The space

created by the parting of adjacent pentlandite grains is frequently infilled by chalcopyrite. In certain thin sections, an intimate growth between pentlandite and pyrrhotite is observed wherein pyrrhotite is hosted within the larger pentlandite crystals (Fig. 1.12c). In such instances, pyrrhotite occurs as small (0.1 mm diameter) anhedral rounded grains or as flames. The nature of this intergrowth (coupled with the fact that pyrrhotite is confined to the boundaries of the pentlandite crystals) suggests that this texture may have developed as a result of immiscibility, *i.e.*, separation of the more Fe-rich discrete pyrrhotite phase from the host pentlandite. It should also be noted that when millerite is present in the mineral assemblage, pyrrhotite is not observed as an isolated mineral, but instead is only present in association with pentlandite as described above.

Bornite occurs almost exclusively along fractures in millerite (Fig. 1.12b), chalcopyrite, and pentlandite, suggesting that it is the latest of the major sulphide constituent to crystallize.

Magnetite is observed in nearly all polished thin sections, and can be divided into two distinct populations, both of which may be present simultaneously. These include: (1) Fine-grained (average diameter of 0.1 mm), euhedral crystals that occur ubiquitously throughout the entire suite of polished thin section, and exhibit no discernable internal textures or surface features. (2) Coarse magnetite (ranging in size from 0.25 to 1.0 mm), equant but anhedral (locally subhedral) crystals with heavily pitted surfaces, some of which exhibit oxyexsolution lamellae of ilmenite along {100} and {111} (Fig. 1.12f,g). In samples where ilmenite lamellae are present, the host magnetite is also intimately associated with chalcopyrite and bornite, appearing as if the magnetite were being dissolved and replaced by the sulphides. This population of magnetite is only observed in samples that were collected directly adjacent to the margins of Cu-Ni-PGE veins where there is evident assimilation of the country rock present. The textural relationships observed amongst these two populations of magnetite suggests that they represent two separate stages of magnetite formation, with population (1) being earlier, and (2) being later, the latter possibly resulting from interactions between the sulphide magma and the host country rock.

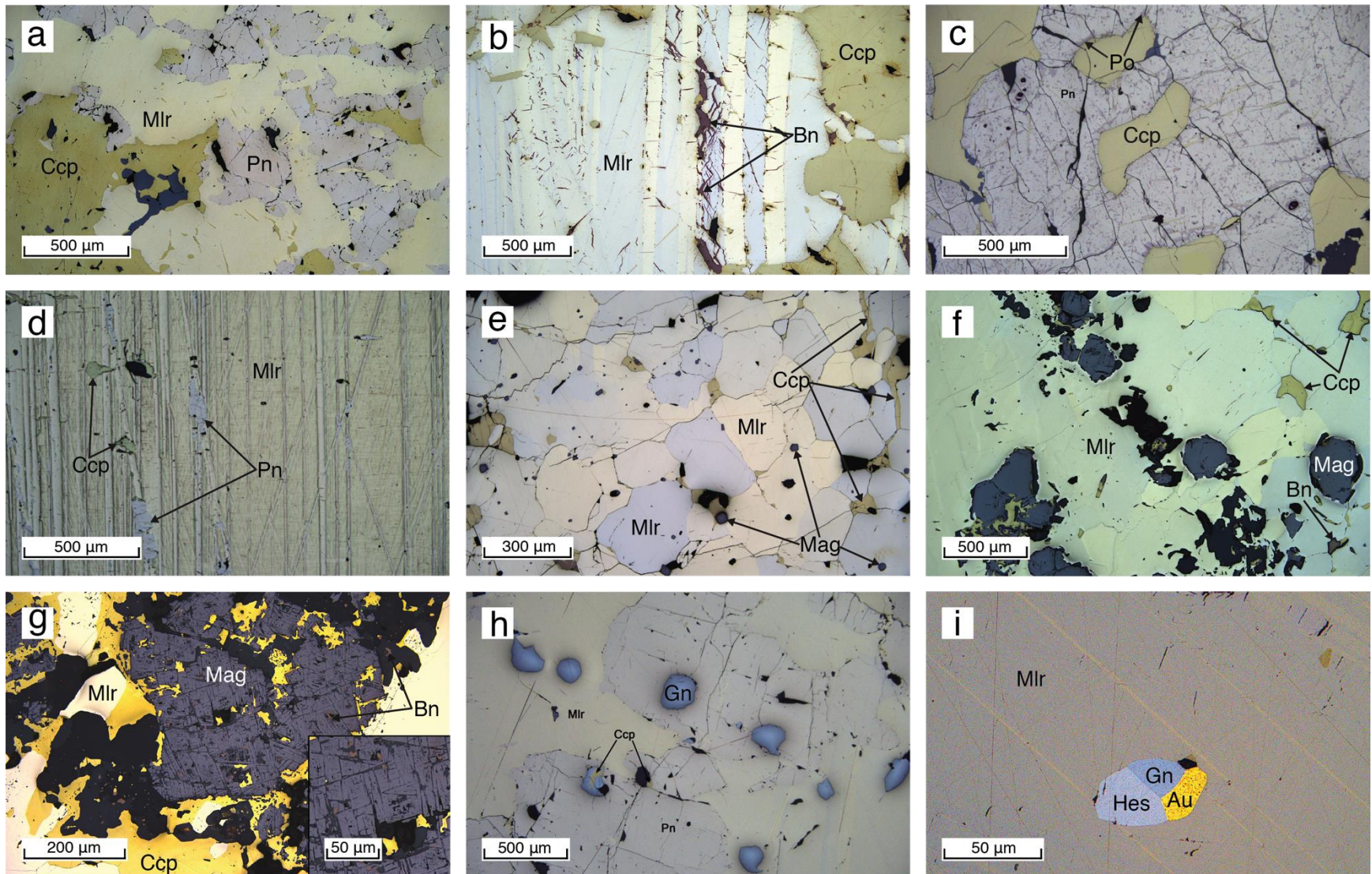


**FIG. 1.12.** Reflected-light images of mlr and associated minerals from magmatic systems. (a) Coarse pn surrounded by mlr and ccp from COL (1510 m). Note the absence of po from the assemblage. (b) Coarse mlr with ccp and bn from COL (unknown depth). Note the lamellar twins in mlr and the occurrence of bn along fractures. (c) Coarse pn hosting po in a ccp matrix from COL (1470 m). Note how the po is confined to the grain margins of the Pn. (d) Coarse mlr from COL (unknown depth) exhibiting pervasive lamellae. Note the presence of two distinct sets. (e) Granular mlr from NRS (1480 m). Note the pronounced development of triple junctions between grains. (f,g) Coarse mag hosted in mlr and ccp from NRS (1480 m). Note the ilm lamellae (dark grey) present in the mag (light grey), as well as the ccp filling in the original outline of the crystals. (h) Coarse mlr and pn with minor ccp from COL (1510 m) hosting equant gn grains. (i) Coarse mlr from COL (unknown depth) hosting a composite grain of hes, gn, and Au. Note the triple junction, and how the composite grain does not cause a distortion of the twin lamellae.

Galena and hessite ( $\text{Ag}_2\text{Te}$ ) occur in trace concentrations (<1 modal %) throughout many of the samples as trace minerals. The two occur as both isolated, euhedral, and equant grains ranging in size from 0.01 to 0.10 mm in diameter (Fig. 1.12h), and as irregular growths along fractures within grains or along grain boundaries. These minerals were frequently observed in close association with one another, and in one instance, an elliptical cross section of a composite grain was observed containing galena, hessite, and gold, all meeting at a triple junction (Fig. 1.12i). The boundary shared between the minerals within this composite grain may suggest the existence of a single homogeneous phase that separated during cooling.

In addition to the minerals described above, a number of other trace minerals were observed in thin section that could not be positively identified under the petrographic microscope (described below).

### *1.3.3 Electron Microscopy I – PGMs & Associated Trace Minerals*

A large number of trace minerals were observed petrographically amongst representative magmatic samples of millerite including platinum-group minerals (PGMs), tellurides, sulphides, alloys, and native metals. As the potential effects of the chemistry (including trace-elements) on the morphology of millerite is under investigation, documentation of particularly the PGMs is important, as platinum-group elements (PGEs) may be present in significant quantities in millerite. Furthermore, understanding the textural relationships between trace minerals and their host assemblage (or one another) can be used to constrain the paragenesis of the system and provide indications as to re-equilibration processes.

Michenerite,  $\text{PdBiTe}$ , was observed in over half of the millerite-bearing samples, and represented the most abundant of the PGMs observed. Grains are anhedral (locally subhedral) and range in size from 20 to 200  $\mu\text{m}$  in diameter. They typically occurs as isolated grains (>50 %) hosted within all of the major sulphides, rarely along microfractures in the host mineral. Michenerite is frequently in association with other PGMs and trace minerals such as moncheite

(Fig. 1.13a-d), hessite (Fig. 1.13b-i), froodite (Fig. 1.13f,g), niggliite (Fig. 1.13g), kotulskite (Fig. 1.13h), and sobolevskite (Fig. 1.13i). Many of these micro-assemblages comprise composite grains exhibit extremely complex intergrowth textures, suggestive of immiscibility and/or remobilization following the initial crystallization.

Moncheite,  $(\text{Pt,Pd})(\text{Te,Bi})_2$ , is the second most common PGM observed throughout the samples. Grains are anhedral (locally subhedral), and range in size from 10 to 50  $\mu\text{m}$  in diameter. They typically occur as isolated grains (>50 %), and rarely as irregular intergrowth along microfractures or grain boundaries. Moncheite is observed alone in some sections (Fig. 1.14a), but more common occurs in association with michenerite (Fig. 1.13a-d), and/or hessite (Fig. 1.13b,c).

Froodite,  $\text{PdBi}_2$ , occurs as anhedral and irregular grains ranging in size from 15 to 50  $\mu\text{m}$  in diameter. Froodite is not observed as an isolated mineral, but instead always occurs in textural association with other phases, and develops in complex intergrowths with at least two other trace minerals, including michenerite, niggliite, hessite (Fig. 1.13f,g), and parkerite (Fig. 1.14i).

Kotulskite,  $\text{Pd}(\text{Bi,Te})$ , occurs as anhedral, irregular (sometimes elongated) grains ranging in size from  $5 \times 10 \mu\text{m}$  to  $5 \times 30 \mu\text{m}$ . It is not observed alone, but only occurs in association with michenerite and/or hessite (Fig. 1.13h, Fig. 1.14e).

Niggliite,  $\text{PtSn}$ , is only observed in a single sample from Nickel Rim South mine (1480 m), and occurs as an anhedral, irregular grain approximately  $10 \times 70 \mu\text{m}$  in size. It is one of the several minerals in a texturally complex composite grain that also consists of michenerite, froodite, hessite, and galena (Fig. 1.13g).

Paolovite,  $\text{Pd}_2\text{Sn}$ , is only observed in a single sample from Nickel Rim South mine (1680 m), and occurs as an anhedral, irregular grain approximately  $10 \times 100 \mu\text{m}$  in size. It occurs along a microfracture in chalcopyrite and is not associated with any additional PGMs (Fig. 1.15a).

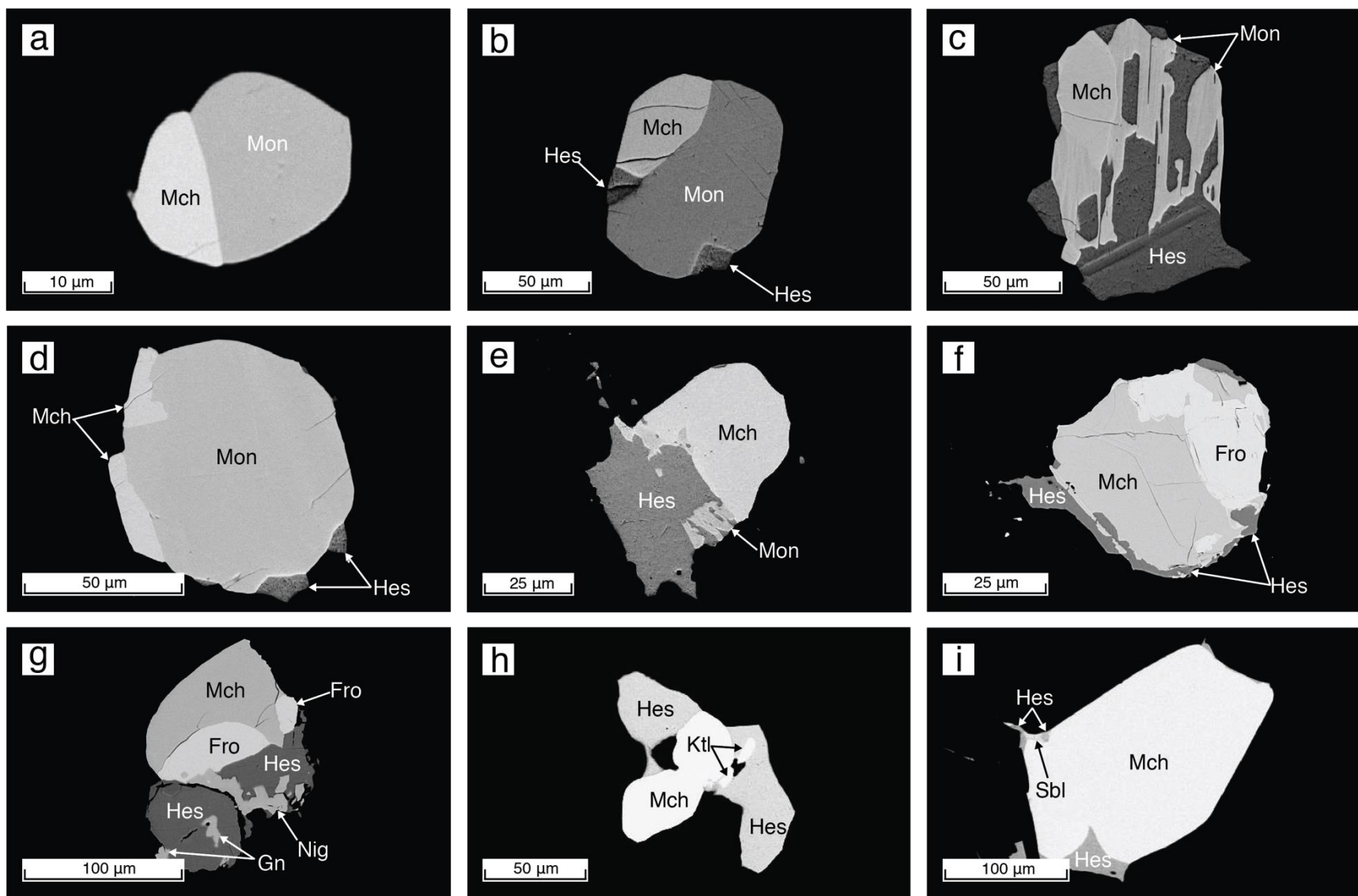


**FIG. 1.13.** Backscatter electron images of PGMs and associated minerals from magmatic systems. (a) Composite grain of mch and mon from COL. (b) Composite grain of mon, mch, and hes from COL. (c) Complex composite grain of hes, mon, and mch from COL. (d) Equant grain of mon with hes and mch present on the peripheries from COL. (e) Composite grain of hes, mon, and mch from COL. (f) Complex composite grain of hes, mch, fro, nig, and gn from NRS. (g) Complex composite grain of mch, fro, hes, gn, and nig from NRS. (h) Composite grain with a core of mch surrounded by hes and ktl from NRS. (i) Grain of mch with occurrences of hes and sbl on the peripheries from COL.

Sobolevskite, PdBi, is only observed in a single sample from Coleman mine (unknown depth), and occurs as an anhedral, irregular grain  $5 \times 10 \mu\text{m}$  in size. It is found in association with michenerite and hessite along the margins of a composite grain (Fig. 1.13i).

Sudburyite, (Pd,Ni)Sb, is only observed in a single sample from Nickel Rim South mine (1480 m), and occurs as anhedral, elongated grains approximately  $10 \times 60 \mu\text{m}$  in size. It occurs in association with hessite at grain boundaries between millerite and gangue minerals (Fig. 1.14f).

Gold is observed in two samples from Coleman mine (unknown depth), and occurs as anhedral, equant grains approximately  $15 \mu\text{m}$  in diameter. It occurs in association with hessite (Fig. 1.14g) and galena in isolated grains hosted within millerite.

Hessite,  $\text{Ag}_2\text{Te}$ , is the most common of the trace minerals amongst magmatic samples, and is observed in almost all thin sections. It occurs as isolated equant grains that are generally anhedral (although locally euhedral) equant grains ranging from 20 to  $150 \mu\text{m}$  in diameter (Fig. 1.14d). It is important to note that while hessite is observed as isolated euhedral crystals, it is much more common as a late-stage irregular intergrowths or overgrowths associated with other trace minerals including michenerite, moncheite, froodite, kotulskite, niggliite, sobolevskite, sudburyite, gold, and bismutohauchecornite (Fig. 1.13, 1.14). When present with any number of these minerals, the textures observed between hessite and the associated minerals may become quite complex, suggestive of multiple periods of crystallization, remobilization, or re-equilibration.

An unknown Ag-Se compound is only observed in a single sample from Coleman mine (unknown depth). It occurs as an intimate vermicular intergrowth with galena where veinlets of the Ag-Se range in thickness from 1 to  $5 \mu\text{m}$  (Fig. 1.15c). The textural relationship between the two appears to further indicate immiscibility between the phases. Additionally, galena examined in this study is Se-bearing, and based on qualitative EDS analyses, it is not uncommon for Se to be present as a major constituent of galena at between 5 and 10 wt. %.

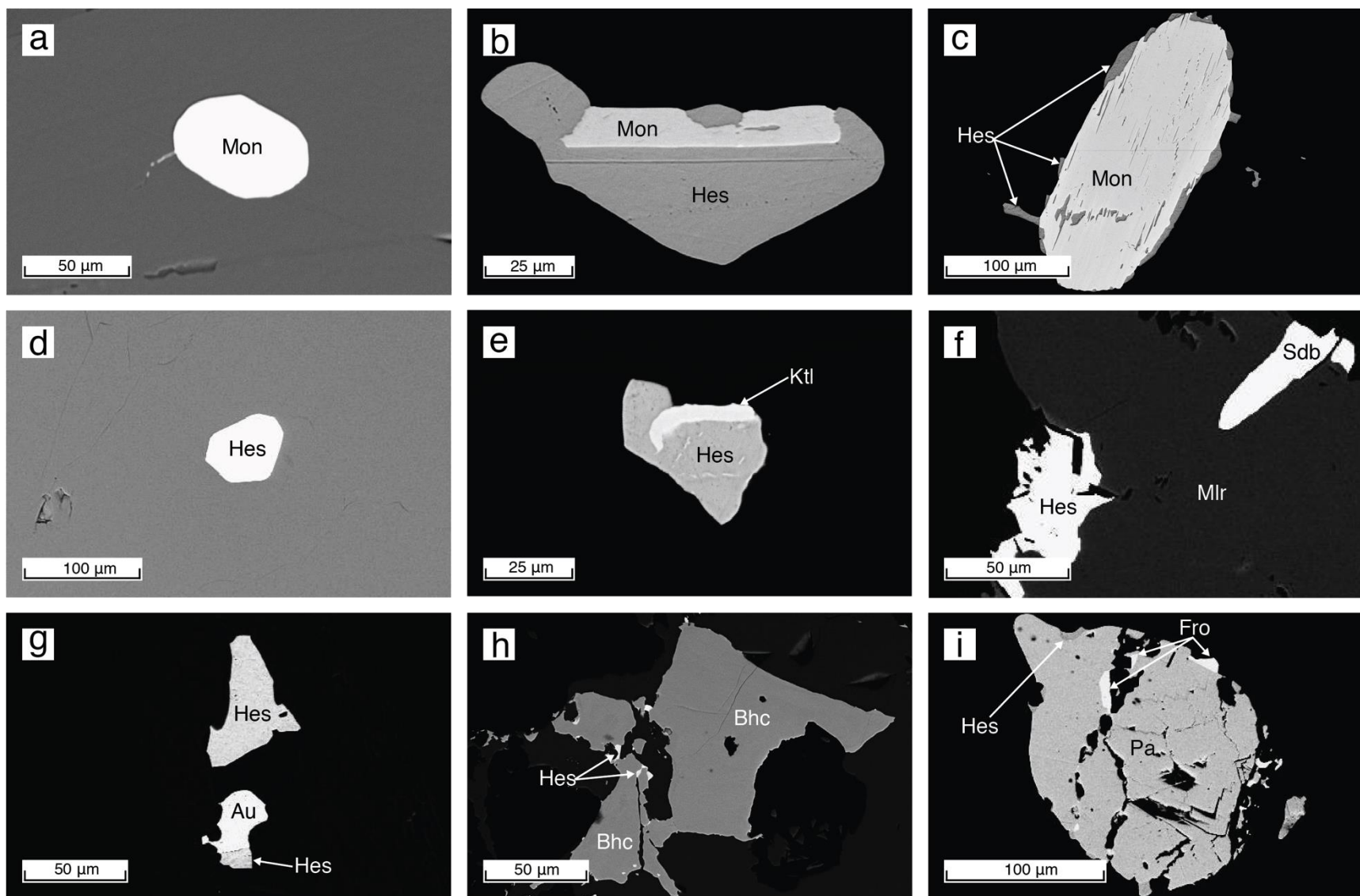


**FIG. 1.14.** Backscatter electron images of PGMs and associated minerals from magmatic systems. (a) Equant, subhedral grain of mon hosted in a mlr matrix from COL. (b) Composite grain of hes and mon from COL. (c) Composite grain of hes and mon from COL. (d) Euhedral grain of hes hosted in a mlr matrix from NRS. (e) Composite grain of hes and ktl from NRS. (f) Isolated grains of hes and sdb hosted along the grain boundaries of mlr from COL. (g) Au in association with hes from COL. (h) Large grain of bhc with minor hes occurring along grain boundaries in mlr from NRS. (i) Heavily fractured grain of pa with minor fro and hes from COL.

Bismutohauchecornite,  $\text{Ni}_9\text{Bi}_2\text{S}_8$ , occurs as anhedral grains that may be both equant or irregular in shape, and range in size from 5 to 250  $\mu\text{m}$ . Equant grains are smaller (10 to 50  $\mu\text{m}$  in diameter), are not associated with other trace minerals, and occur as isolated grains within the main sulphide mass (Fig. 1.15d,e). Grains exhibiting an irregular morphology show a wider range of sizes (5 to 250  $\mu\text{m}$ ) and occur along microfractures and grain contacts where they are sometimes in association with hessite (Fig. 1.14h), or may exist independently (Fig. 1.15f).

Hawleyite,  $\text{CdS}$ , is only observed in a single thin section from Coleman mine (1510 m), and occurs as a euhedral, equant grain approximately 5 $\mu\text{m}$  in diameter along the margin of a galena crystal (Fig. 1.15g).

Parkerite,  $\text{Ni}_3(\text{Bi,Pd})_2\text{S}_2$ , is only observed in a single thin section from Coleman mine (1510 m), and occurs generally as anhedral (locally euhedral) grains ranging in size from 15 to 100  $\mu\text{m}$  in diameter. It may occur as isolated grains (Fig. 1.15h), or in association with other mineral such as hessite, froodite (Fig. 1.14i), acanthite (?), and galena (Fig. 1.15i).

Acanthite (?),  $\text{Ag}_2\text{S}$ , is only observed in a single thin section from Coleman mine (1510 m), and occurs as an anhedral, equant grain approximately 5 $\times$ 10  $\mu\text{m}$  in diameter. It is observed along the margin of an isolated galena crystal also in association with parkerite (Fig. 1.15i).

#### 1.3.4 Electron Microscopy II – Synthetic Materials

Distances inside the capsule are reported as the total distance from the centre of the furnace (*i.e.*  $T_2$ ), with this point being defined as 0 cm. Therefore, distance referenced with respect to the capsule will increase from where the reactants are volatilized at  $T_2$  (0 cm) towards  $T_1$  (20 cm) where deposition is intended to occur (Fig. 1.16a). Two observations remained constant amongst all trials: (1) the grain size of individual crystals increases towards  $T_1$  and as distance approaches 20 cm in capsule; and (2) the development of euhedral crystals is enhanced towards  $T_1$  and as distance approaches 20 cm in the capsule. These observations suggest a direct relationship between crystal growth of NiS and temperature, specifically the nature of the

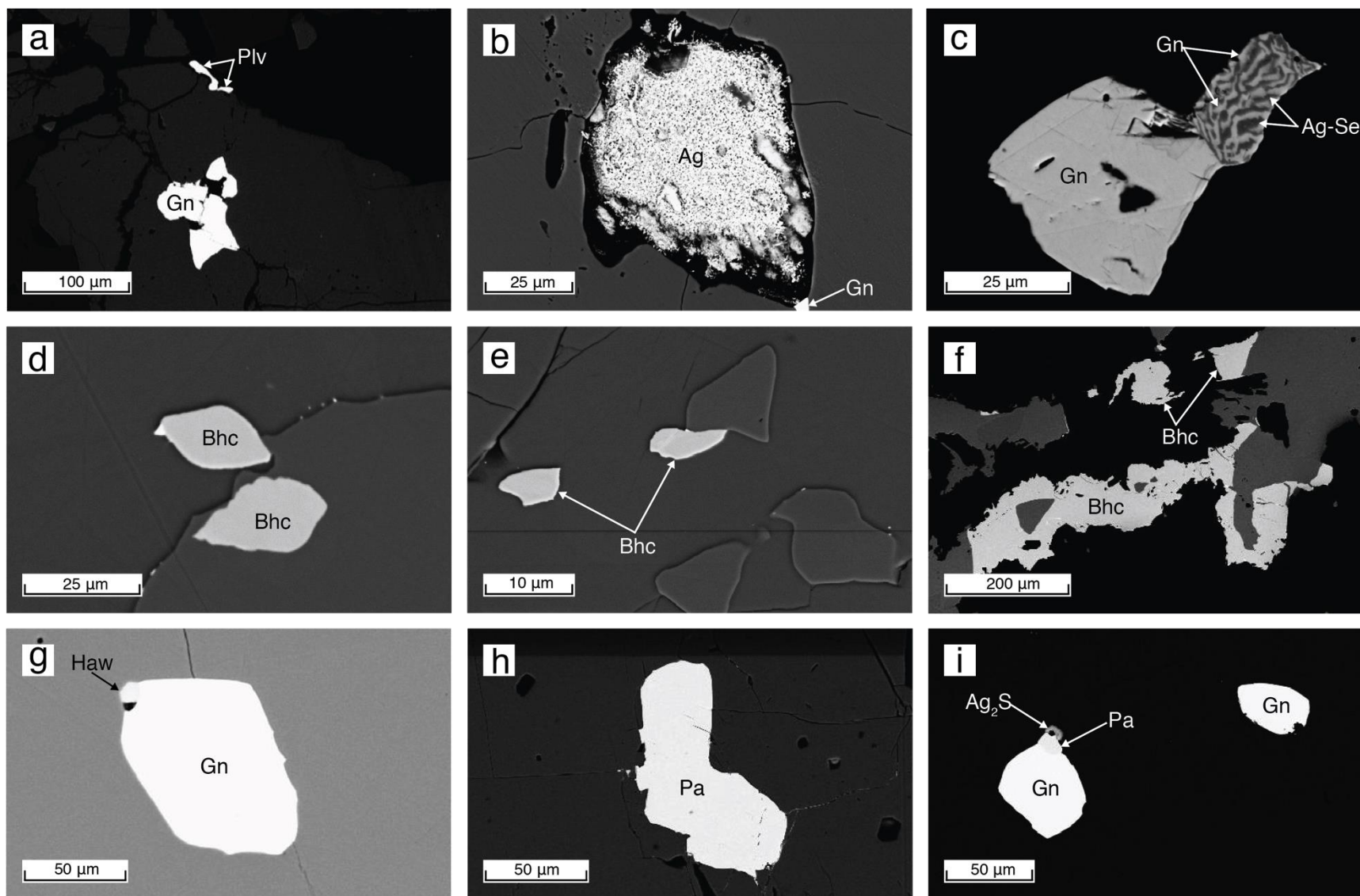


**FIG. 1.15.** Backscatter electron images of PGMs and associated minerals from magmatic systems. (a) Isolated grains of gn and plv occurring along fractures and grain boundaries in ccp from NRS. (b) Pitted Ag grain with gn from NRS. (c) Gn with an unknown Ag-Se from COL. Note the intergrown in the smaller grain indicating unmixing. (d,e) Isolated grains of bhc hosted in mlr from COL. (f) Coarse bhc hosted along fractures and grain boundaries from COL. (g) Isolated grain of gn with a small, euhedral haw crystal present on the edge from COL. (h) Isolated grain of pa from COL. (i) Isolated, equant grains of gn with pa and acanthite (?) on the edge from COL.

temperature gradient that exists. The greatest impact of temperature is expected to occur in runs No. 2 and No. 3 as these were conducted at higher temperatures ( $800\text{ }^{\circ}\text{C} \rightarrow 700\text{ }^{\circ}\text{C}$ ). The latter point is important, as it implies the bulk of the material in the capsule is likely to have been present above the melting point of NiS ( $797\text{ }^{\circ}\text{C}$ ), although this could have been further depressed owing to the presence of Fe and Co impurities in the starting material (albeit in very low concentrations). Such a situation would result in any material condensing from the gaseous state to likely form as droplets (Fig. 1.16b) rather than nucleating and developing as euhedral crystals. Further, the development of such crystals is likely to occur only towards 20 cm in the capsule, where the temperatures encountered would be the lowest for the system (Fig. 1.16c,d).

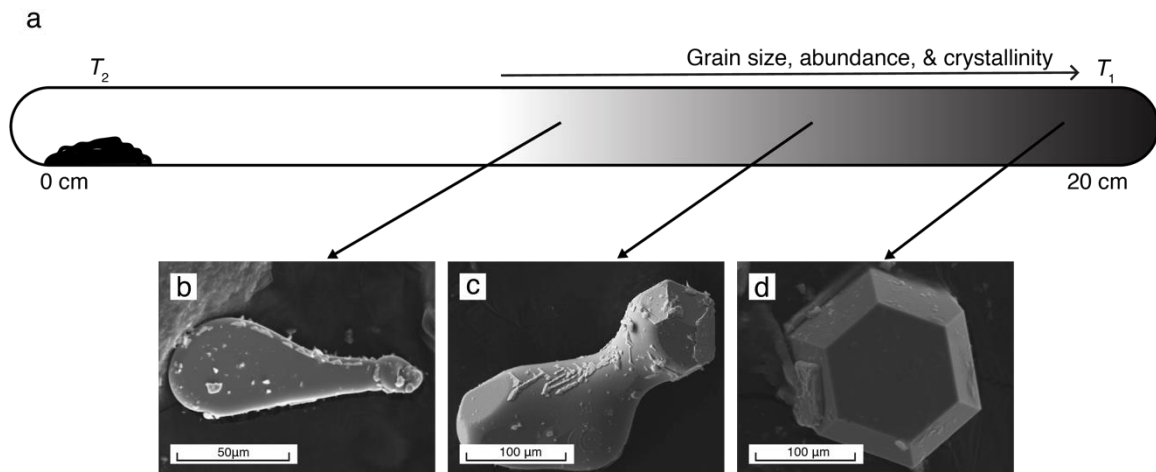


**FIG. 1.16.** (a) Schematic cross section of a silica capsule illustrating the increasing development of euhedral grains towards  $T_1$ . (b) Near the centre of the capsule, the grains are anhedral and form as liquid droplets along the inner walls. (c) Closer to  $T_1$ , the grains begin to exhibit crystal faces, but may not be fully developed. Some occur as subhedral grains attached to anhedral droplets that are dangling from the walls of the tube. (d) Along the final several cm of the capsule, the grains exhibit well-developed crystal faces, *i.e.*, are euhedral.

The initial CVT synthesis experiment was conducted for a period of 21 days and temperature gradient from  $700\text{ }^{\circ}\text{C} \rightarrow 600\text{ }^{\circ}\text{C}$ . This produced crystals ranging from 10 to  $100\text{ }\mu\text{m}$  in diameter from distances 10 to 20 cm in the capsule. No crystals were observed between 0 and 10 cm. From distances 10 to 17 cm, the crystals are platy in morphology, with the pinacoid  $\{0001\}$  being dominant, and a minor dipyrmaid  $\{10\bar{1}1\}$  being present (Fig. 1.17a). Crystal faces

are overall well developed, but may be individually distorted, owing to differences in the relative sizes of the crystal faces present. In general, this differential growth preferentially impacts the faces of the dipyrmaid  $\{10\bar{1}1\}$  rather than those of the pinacoid  $\{0001\}$  (Fig. 1.17b) and is likely the result of differential nutrient flow. From distances 17 to 20 cm, the crystals are prismatic in morphology, with crystals exhibiting just the dipyrmaid  $\{10\bar{1}1\}$  (Fig. 1.17c) or a combination of the dipyrmaid  $\{10\bar{1}1\}$  and the pinacoid  $\{0001\}$  roughly equally developed (Fig. 1.17d). Crystals are euhedral with well-developed faces, although some grains do show slight distortion from their ideal geometric form. In general, the total population of grains in the capsule is represented by largely by equant crystals exhibiting a combination of the dipyrmaid  $\{10\bar{1}1\}$  and pinacoid  $\{0001\}$  in equilibrium (60%), prismatic crystals exhibiting just the dipyrmaid  $\{10\bar{1}1\}$  (30%), and platy crystals showing a dominant pinacoid  $\{0001\}$  with minor dipyrmaid  $\{10\bar{1}1\}$  (10%).

The second CVT synthesis experiment was conducted over a period of 12 days with a temperature gradient from 800 °C  $\rightarrow$  700 °C. This produced coarser crystals than those in the first experiment, ranging in size from 20 to 300  $\mu\text{m}$  in diameter, with most being concentrated between 15 and 20 cm in the capsule. No crystals were observed from 0 to 15 cm. Although no correlation between distance and form is present, crystals do increase in grain size towards 20 cm. Grains are prismatic to platy in habit, and the dominant forms observed again are the dipyrmaid  $\{10\bar{1}1\}$  and the pinacoid  $\{0001\}$ . Crystals are predominantly euhedral and show evidence in some cases of twinning (Fig. 1.17e) as well as distortion from their ideal geometric form (Fig. 1.17f). Examination of the run products reveals that the proportion of grains showing the pinacoid  $\{0001\}$  to be dominant is lower than that observed in the first synthesis experiment by  $\sim 15\%$  based on visual estimates. In general, the total population of grains in the capsule is represented largely by equant crystals exhibiting the dipyrmaid  $\{10\bar{1}1\}$  and pinacoid  $\{0001\}$  showing equal development (50%), prismatic crystals exhibiting just the dipyrmaid  $\{10\bar{1}1\}$  (45%), and platy crystals showing a dominant pinacoid  $\{0001\}$  with minor dipyrmaid  $\{10\bar{1}1\}$  (5%).

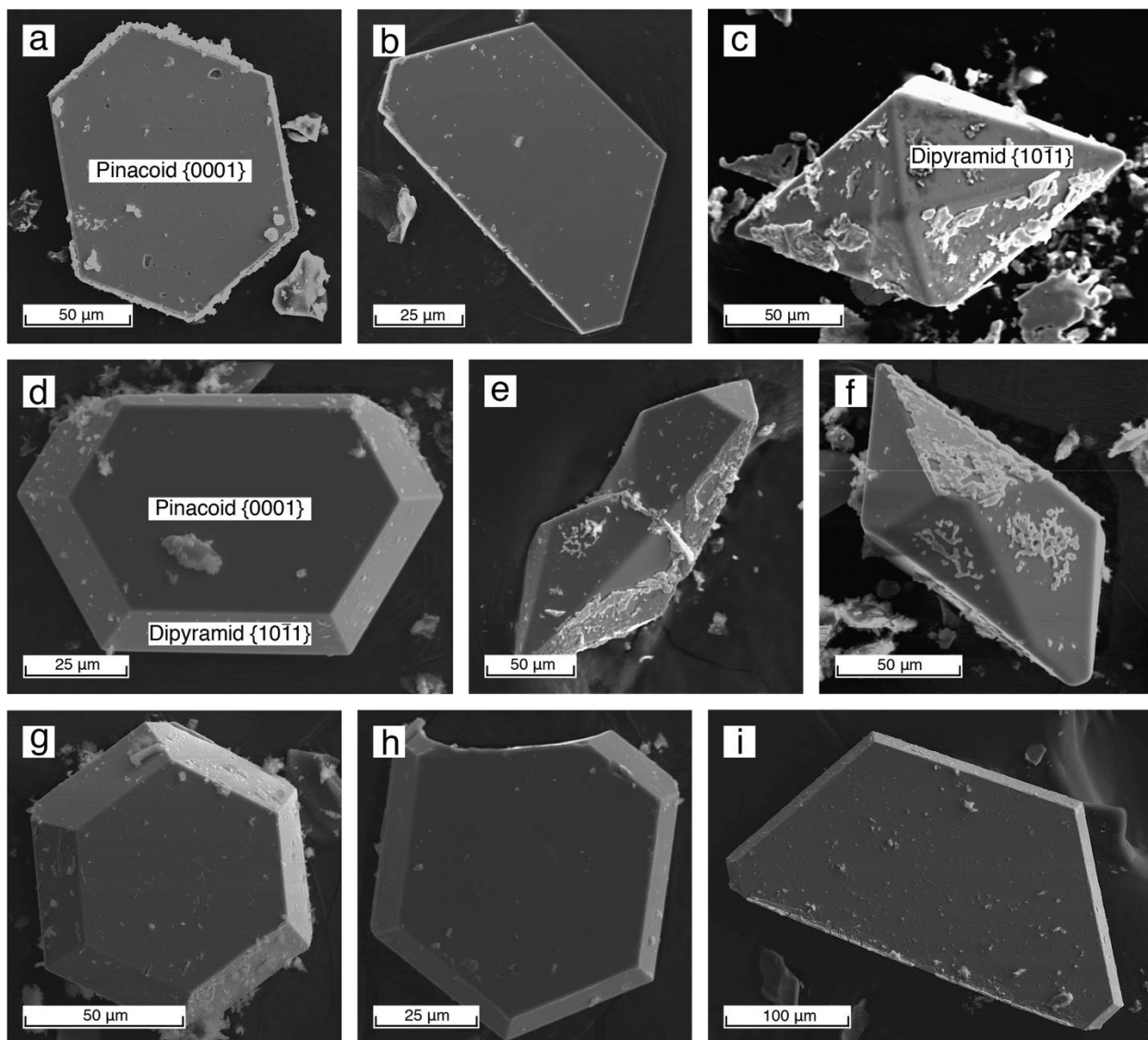


**FIG. 1.17.** Secondary electron images of synthetic crystals of  $\alpha$ -NiS grown using chemical vapour transport. (a) Platy crystal exhibiting the dominant pinacoid  $\{0001\}$  and minor dipyramid  $\{10\bar{1}1\}$ . This crystal is only  $\sim 5 \mu\text{m}$  in thickness. (b) Platy crystal exhibiting dominant pinacoid  $\{0001\}$  and minor  $\{10\bar{1}1\}$ . Note the distortion the two hexagonal edges leading to the development of a near trapezoidal shape. This crystal is only  $\sim 5 \mu\text{m}$  in thickness. (c) Prismatic crystal showing the dipyramid  $\{10\bar{1}1\}$  exclusively. Note the perfection of the crystal. (d) Equant crystal exhibiting the pinacoid  $\{0001\}$  and dipyramid  $\{10\bar{1}1\}$  present in equilibrium. The distortion of the upper edge is representative of where the crystal nucleated on the interior of the silica capsule. (e) Twinned crystal exhibiting only the dipyramid  $\{10\bar{1}1\}$ . (f) Prismatic crystal with only the dipyramid  $\{10\bar{1}1\}$  present. Note the distortion from the ideal dipyramid form. (g) Equant crystal showing both the pinacoid  $\{0001\}$  and dipyramid  $\{10\bar{1}1\}$  in equilibrium with one another. Note the perfection of the crystal. (h) Platy crystal showing the dominant pinacoid  $\{0001\}$  with minor dipyramid  $\{10\bar{1}1\}$ . The distorted upper edge is where the crystal was attached to the interior of the silica capsule. (i) Relatively large, platy crystal exhibiting major pinacoid  $\{0001\}$  and minor dipyramid  $\{10\bar{1}1\}$ . Note the distortion from the ideal hexagonal shape.

The third CVT synthesis experiment was conducted over a period of 45 days with a temperature gradient of  $800 \rightarrow 700$  °C. This produced crystals that were dimensionally similar to those of the second run, but in some cases these are slightly larger, ranging from 20 to 400  $\mu\text{m}$  in diameter. However, it is of note that the crystals from this run only developed from 19 to 20 cm in the capsule, and there is no division of the capsule based on the morphology of the crystals over this interval. No grains were observed along the remaining length of the capsule. Grains are platy to equant in habit, and the dominant forms observed are the pinacoid  $\{0001\}$  and the dipyrmaid  $\{10\bar{1}1\}$ . Most show cases where the two forms are equally developed (Fig. 1.17g) or cases where the pinacoid  $\{0001\}$  is dominant (Fig. 1.17h). Unlike the previous two experiments no grains were found to exhibit the dipyrmaid  $\{10\bar{1}1\}$  exclusively. Crystals are predominantly euhedral, although as was observed in the previous two experiments, some exhibit deviations from the ideal geometric form (Fig. 1.17i). The increase in the relative dominance of the faces that constitute the pinacoid  $\{0001\}$  may be a function of the time over which crystallization occurs, *i.e.*, NiS crystallizing over a relatively short period may favour crystals dominated by the dipyrmaid  $\{10\bar{1}1\}$ , whereas crystallization over slower periods favours the pinacoid  $\{0001\}$ .

Notably absent from the list of observed forms in the prism  $\{10\bar{1}1\}$ , which is the dominant form present in crystals of millerite of hydrothermal origin (Goldschmidt 1920). Given that both the dipyrmaid  $\{10\bar{1}1\}$  and pinacoid  $\{0001\}$  are observed in synthetic crystals, it is possible that elongated crystals may develop (although none were observed), but certainly not ones that are comparable with the extreme length-to-width ( $l:w$ ) ratios ( $>20$ ) as are observed in acicular millerite.

## 1.4 RESULTS

### 1.4.1 Chemistry

A total of 325 analyses ( $n = 180$  magmatic millerite,  $n = 145$  hydrothermal millerite) were collected from a total of 18 unique samples ( $n = 12$  magmatic,  $n = 6$  hydrothermal). The only elements detected in millerite throughout the entirety of the investigation were Ni, Fe, Co, and S. Formula

calculations were based on the assumption of one S per formula unit, and these data are presented in Figure 1.18.

Analyses normalized to 100% Ni+Fe+Co all plot >95% Ni *apfu*, *i.e.*, the compositions of the grains analyzed are all near end-member regardless of the respective environment of formation (magmatic vs. hydrothermal). The data show that the chemistry of millerite from magmatic environments cluster at  $\geq 98\%$  Ni *apfu*. That from hydrothermal environments shows moderate evidence for the existence of two trends, one relatively enriched in Fe and the other in Co.

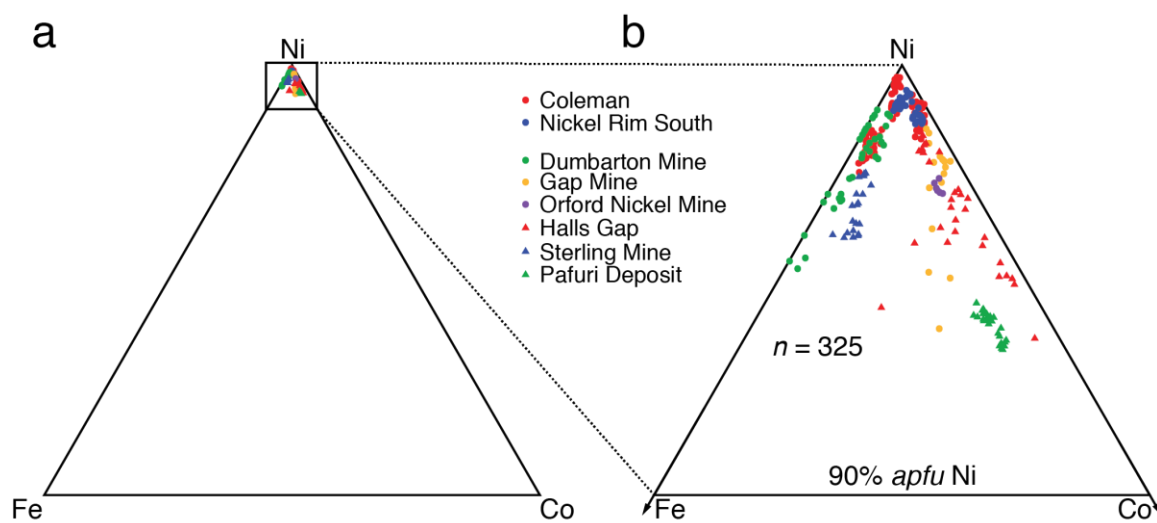


**FIG. 1.18.** Ternary diagram representing the comparative data normalized to 100 % Ni+Fe+Co in millerite. Colours and symbols given in the legend remain consistent through this section. (a) Entirety of Ni-Fe-Co ternary space, note the extremely tight grouping of data near the Ni-apex. (b) Upper section of the ternary showing the region 90 to 100 % *apfu* Ni. Magmatic samples from Coleman and Nickel Rim South mine cluster tightly, exhibiting very low Fe + Co substitution ( $\leq 2\%$  *apfu*). Data for hydrothermal samples show a more moderate spread in the Fe + Co substitution ( $\leq 5\%$  *apfu*).

The average chemical composition of millerite from magmatic localities is  $(\text{Ni}_{0.974}\text{Fe}_{0.007}\text{Co}_{0.004})_{\Sigma 0.985}\text{S}$ , and considering the extremely narrow compositional range that these samples represent, millerite from Coleman mine and Nickel Rim South mine are chemically indistinguishable. Given the both range in distances between the mines (45 km), and those related to vertical distances over which sampling occurred (230 m at Coleman and 480 m at Nickel Rim South), it is truly remarkable that the chemical composition of the millerite remains so fixed.

The average chemical composition of millerite from hydrothermal localities is  $(\text{Ni}_{0.934}\text{Co}_{0.021}\text{Fe}_{0.013})_{\Sigma 0.969}\text{S}$ , and minor variations in chemistry were noted between localities in these instances. On a broad scale, the substitution of  $\text{Fe} + \text{Co} \leftrightarrow \text{Ni}$  is greater than that seen from millerite from magmatic environments. However, in terms of total substitution, the average value of 3.4% *apfu* for total  $\text{Fe} + \text{Co}$  is still an extremely minor component of the overall chemistry. This attests to the fact that millerite, in general, does not show high concentrations of Fe or Co regardless of the environment in which it forms.

Data for *Me:S* values and additional statistics of millerite from Coleman and Nickel Rim South mine are presented in Figure 1.19. All of the data plot within  $3\sigma$  of the mean (0.985), indicating a very high degree of chemical homogeneity and very little in the way of vacancies (*i.e.*, a defect structure). The range of the data is also quite narrow (0.969 to 1.001) further indicating that there is very little in the way of absolute variations with respect to the *Me:S* values for all samples. Nearly all (>99%) of the non-normalized data show near perfect stoichiometry despite the fact that NiS can show a minor deviation from stoichiometry (avg. 0.015). This is in agreement with previous studies that have shown  $\beta$ -NiS to exhibit a defect structure, albeit to a very limited degree (Wang *et al.* 2006).

Equivalent information on the *Me:S* values obtained for hydrothermal occurrences of millerite are presented in Figure 1.20. All of the data plot within  $3\sigma$  of the mean (0.969) indicating that there is a high degree of chemical homogeneity and still generally minimal occurrence of vacancies. Millerite from Dumbarton mine and Halls Gap are shown to be slightly more metal deficient in comparison to the average, whereas samples from Gap mine, Sterling mine, and the Pafuri deposit exhibit higher *Me:S* values, closer to the ideal stoichiometric ratio. However, despite the range of the data (0.944 to 0.999) being slightly larger than that of millerite of magmatic origin, the variations in *Me:S* values are still minor in comparison to the cumulative average (0.969). Furthermore, as all of the data plot within  $3\sigma$  of the mean, the *Me:S* values are considered homogeneous, just as is observed in the case of millerite of

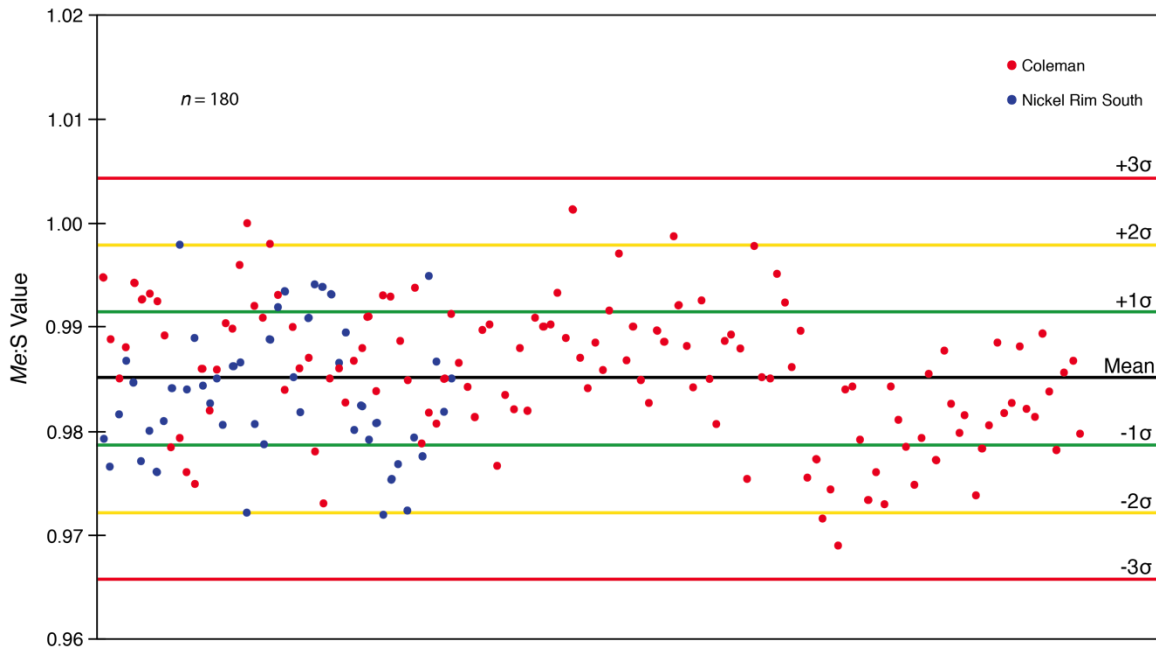


**FIG. 1.19.** *Me:S* value for non-normalized samples ( $n = 180$ ) of magmatic millerite from Nickel Rim South and Coleman mine. Note how all of the data points fall between  $3\sigma$  of the mean, indicating a high degree of chemical homogeneity within the dataset. The  $x$ -axis on this graph is arbitrary, and simply lists the analyses in numerical order.

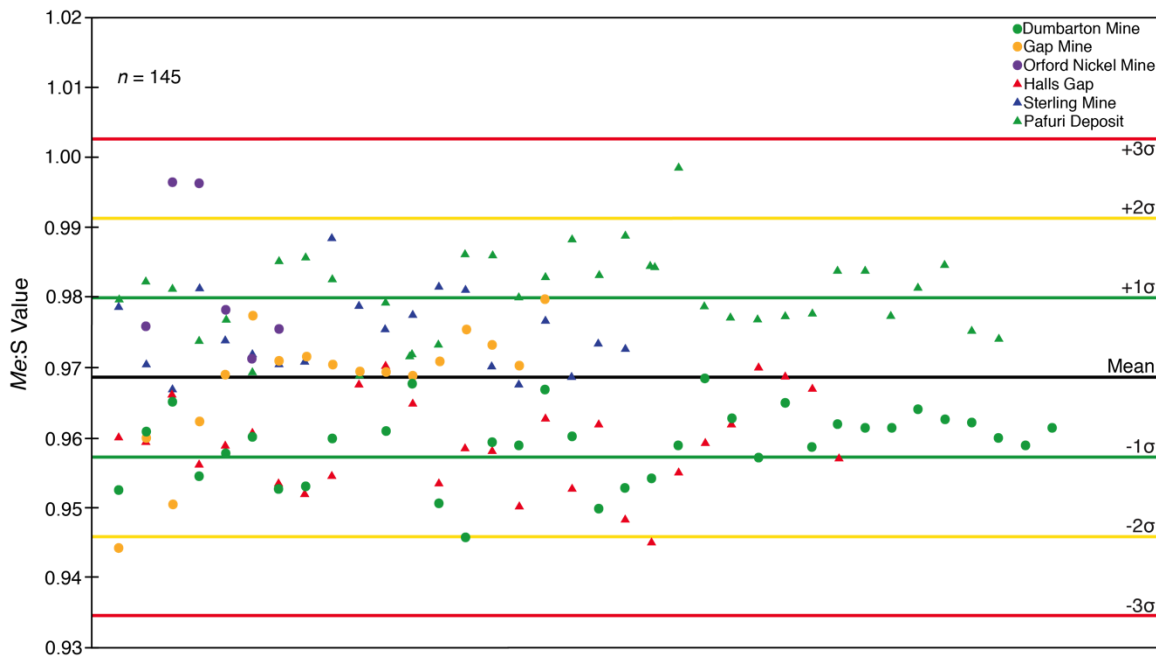


**FIG. 1.20.** *Me:S* values for non-normalized samples ( $n = 145$ ) of hydrothermal millerite of hydrothermal origin. Note how all of the data points fall between  $3\sigma$  of the mean, indicating chemical homogeneity within the dataset. The  $x$ -axis on this graph is arbitrary, and simply lists the analyses in numerical order.

magmatic origin. Consistency with respect to metal deficiency was also observed throughout samples representative of hydrothermal occurrences of millerite.

The Distribution of the  $Me:S$  values of both hydrothermal and magmatic occurrences are presented in Figure 1.21. The data for millerite from both geological settings show a relatively normal distribution, where the majority of the data plots near the mean, with a significant degree of overlap between the two datasets. However, it is evident that the data for magmatic samples exhibits a narrower compositional range that those of hydrothermal origin. This is to be expected as the hydrothermal samples, while all being representative of similar geological conditions, represent a total of six different localities from around the world whereas those of magmatic origin share the same progenitor (the SIC). That being said, the homogeneity of the data for samples from both localities is truly remarkable.

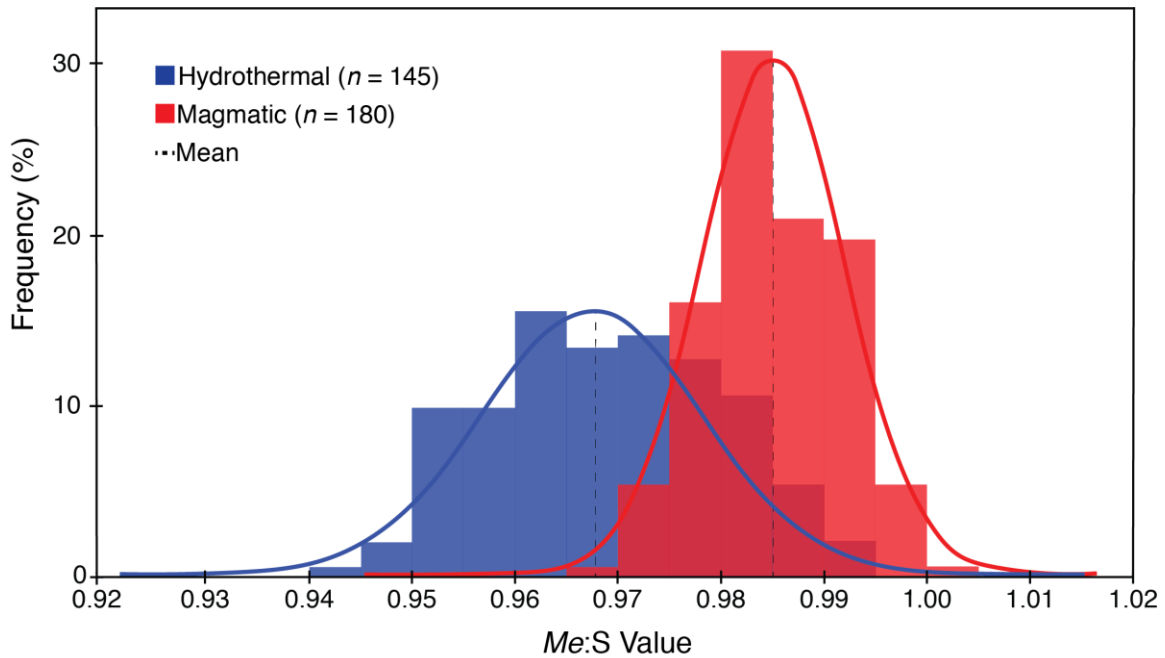


**FIG. 1.21.** Comparative histograms for the  $Me:S$  values of magmatic (red) and hydrothermal (blue) millerite. Note the symmetry exhibited by the two curves, as well as the significant overlap between the two fields.

### 1.4.2 X-Ray Diffraction

Owing to the significant structural differences between  $\alpha$ - and  $\beta$ -NiS, distinguishing between the two polymorphs is achieved with ease through the use of X-ray diffraction techniques (Fig. 1.22). Data from room-temperature X-ray diffraction analyses of magmatic occurrences of millerite as well as synthetic NiS is presented below.

Data collected on synthetic NiS crystals immediately after quenching confirmed it to be  $\alpha$ -NiS (Fig. 1.23a). All major peaks were successfully indexed to  $\alpha$ -NiS, although several minor peaks attributed to CuI were also noted (Fig. 1.23a). The latter are likely products of Cu derived from the breakdown of chalcopyrite and the  $I_2$  used as the transport reagent for the experiments. This material was reanalyzed after approximately one year (samples stored under ambient conditions) and the results show: (1) no evidence for the material having transformed to  $\beta$ -NiS or (2) the presence of any additional diffraction peaks beyond those observed in the initial analysis (Fig. 1.23b). These results are contrary to those of Wang *et al.* (2006) who reported a conversion of approximately 3 to 4% of the  $\alpha$ -NiS to  $\beta$ -NiS over a six-month period where the samples were also stored under ambient conditions. It is not clear as to the exact reason(s) for the observed differences between the experiments, but factors influencing the  $\alpha \rightarrow \beta$  transformation of NiS are discussed in section 1.5.4.

X-ray Diffraction analyses of all material of magmatic origin indicates that millerite ( $\beta$ -NiS) is the only NiS polymorph present. Additional peaks attributed to pentlandite were also noted. As has been previously seen, small amounts of pentlandite were noted as inclusions within millerite lamellae (Fig. 1.12d). Confirmation that millerite is the only NiS polymorph present is consistent with what has previously been reported in the geological literature with respect to the occurrences of NiS in the Sudbury area (Wawrzonkowski 2015) and other magmatic systems (Grice & Ferguson 1974; Krivolutskaya *et al.*, 2012).

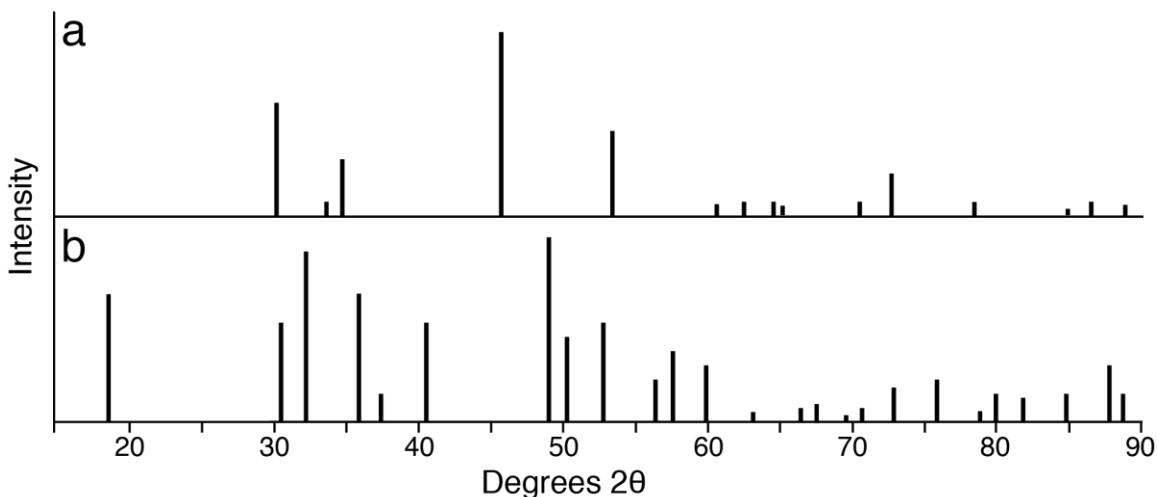


**FIG. 1.22.** Calculated X-ray diffraction powder patterns for (a) crowningshieldite ( $\alpha$ -NiS) and (b) millerite ( $\beta$ -NiS) using  $\text{CuK}\alpha_{\text{avg}}$  ( $\lambda = 1.5418 \text{ \AA}$ ) radiation. Note the difference in both peak intensity, and location between the patterns. Profiles were calculated using the program Powdercell (Nolze & Kraus 1998), based on the crystal-structure data of Trahan *et al.* (1970) and Grice & Ferguson (1974), respectively.

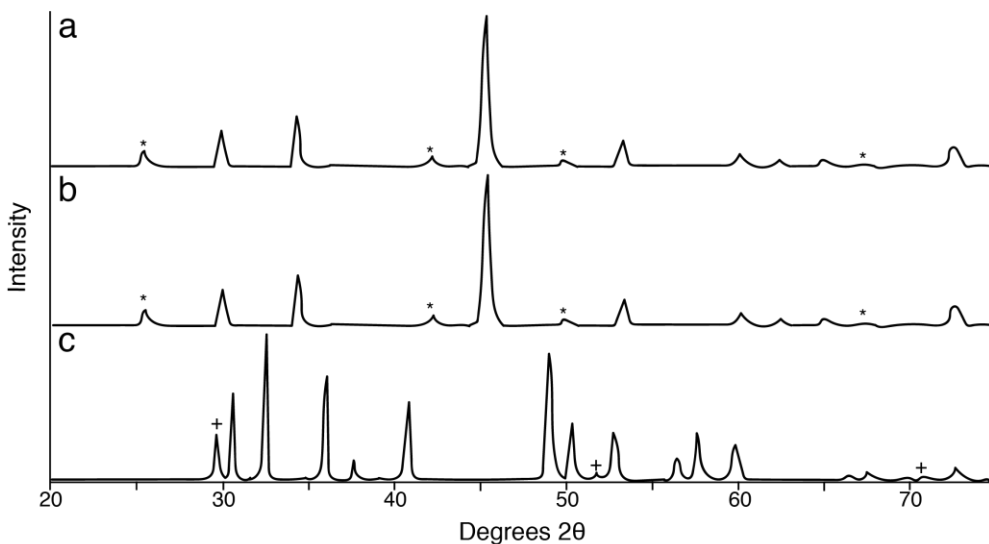


**FIG. 1.23.** Diffractograms for synthetic  $\alpha$ -NiS and millerite from Coleman mine. (a) Profile obtained from synthetic  $\alpha$ -NiS immediately after quenching. All of the major peaks are attributed to  $\alpha$ -NiS, and no peaks corresponding to  $\beta$ -NiS or any other Ni-compound are present. The less intense peaks indicated by (\*) were all matched to a CuI presumed to have formed through the interaction of chalcopyrite impurities in the starting material and  $\text{I}_2$  used as the transport reagent. (b) Profile obtained from the same sample of synthetic  $\alpha$ -NiS approximately one year later. The patterns remain identical, and peaks corresponding to  $\beta$ -NiS are not present. (c) Polyphase powder pattern obtained on natural millerite from Coleman mine consisting primarily of millerite and pentlandite (+). All NiS peaks were successfully indexed as millerite, and the pattern does not reflect the presence of  $\alpha$ -NiS.

## 1.5 DISCUSSION

### 1.5.1 Genesis of Cu-Ni-PGE Veins in the Sudbury Basin

Experimental evidence suggests that the process of crystallization for a Cu-Ni-PGE melt begins with the exsolution of Iss from an Mss dominant precursor at approximately 950 °C (Kullerud *et al.* 1969), and the subsequent establishment of the Hz-Iss at approximately 850 °C (Fleet & Pan 1994; Peregoedova & Ohnenstetter 2002). Following Hz-Iss formation, it is envisioned that in the case of Sudbury footwall Cu-Ni-PGE deposits, the melt is injected into the footwall, probably along pre-existing zones of weakness (Nelles 2012). The exact mechanism driving the injection is not clear, but may involve a combination of density differences between the sulphide and silicate melt, local changes in pressure, and the presence and re-activation of existing structures. With increasing distance from the contact with the SIC, an observable change in mineralogy is noted. The first sulphide phase to develop is chalcopyrite, followed by pentlandite (often only a very minor component of the overall mineralogy in footwall-type systems), the composition of which becomes increasingly Ni-rich as crystallization continues and Ni becomes concentrated in the system. When the residuum becomes significantly enriched in Ni through fractional crystallization, NiS will crystallize as the dominant Ni-bearing phase. The final minerals to crystallize are bornite and an extensive suite of PGMs and other associated precious minerals (such as native Au and Ag) often concentrated at or towards the ends of veins (splays). However, these initial mineral assemblages are then subjected to extensive sub-solidus re-equilibration, likely involving further exsolution, polymorphic transformations, and interactions between the sulphide melt and the host country rock. This is exemplified by numerous textural relationships in the present mineral assemblages.

Exsolution between pentlandite and pyrrhotite (and *vice-versa*) is observed and occurs as discontinuous lamellae, veinlets, or specks of pyrrhotite contained within larger pentlandite grains. Exsolution of pentlandite from pyrrhotite is almost ubiquitous amongst contact-style

deposits, but is uncommon in footwall settings, and the reverse of pyrrhotite exsolving from pentlandite is even less common (Ramdohr 1969). It is noteworthy that the only samples found to contain both millerite and pyrrhotite are those in which the pyrrhotite appears to be an exsolution product related to the breakdown of pentlandite indicating that these two minerals did not coexist in the initial mineral assemblage.

Furthermore, the development of pervasive ilmenite lamellae hosted in magnetite provides additional evidence supporting continued changes in temperature and  $fO_2$ , possibly in relation to progressive, slow cooling of the system. The ilmenite lamellae did not form as a direct result of simple exsolution from the host magnetite, but through a more complicated process of oxyexsolution entailing the initial exsolution of ulvöspinel from magnetite, and subsequent oxidation of these lamellae to ilmenite (Buddington & Lindsley 1964). Between the two distinct populations of magnetite observed throughout the magmatic samples, ilmenite lamellae are only observed amongst the larger magnetite grains that are found to occur along the contact of the veins with the footwall, and are thought to be products of later-stage interaction of sulphide melt with the host country rock. Had all of the magnetite formed simultaneously and early in the system, it is expected that the chemistry amongst the samples would be homogeneous, and the presence of any subsequent exsolution during re-equilibration would have been ubiquitous amongst all the grains. However, as this is not the case, it suggests that the population of magnetite hosting ilmenite lamellae formed as the result of a separate process involving the incorporation of external Ti, possibly being derived from assimilated country rock or an external fluid.

Further evidence of re-equilibration amongst these samples is illustrated by the extensive suite of trace minerals observed. Many of these minerals do not occur as isolated grains of a single mineral, but as complex intergrowths consisting of two to five distinct minerals. The presence of features such as triple junctions, and the coexistence of several individual minerals within these composite grains suggests that they initially formed as a single homogeneous phase

or solid solution at higher temperatures, and that unmixing between the presently individual phases occurred in the solid state as the system cooled slowly.

The paragenetic relationships observed between minerals can be used to construct a rough temperature regime for the system, and will be used to estimate the conditions under which NiS formed. An upper temperature limit can be set by the stabilization of Hz-Iss at approximately 850 °C. It is observed ubiquitously throughout the samples that the initial crystallization of chalcopyrite and the formation of pentlandite occur before that of millerite, although the continued crystallization and/or remobilization of chalcopyrite is observed throughout the samples. Although there is no direct information suggesting the temperature at which chalcopyrite and pentlandite separate from Hz-Iss, experimental studies in the Cu-Fe-S and Fe-Ni-S system indicate that chalcopyrite separates from the Iss at 557 °C, and that pentlandite first stabilizes at approximately 650 °C (Kullerud *et al.* 1969). In addition to the major minerals, numerous grains of michenerite are hosted within millerite suggesting that these formed prior to the crystallization of millerite, or at least while the NiS phase was still plastic or malleable. Experimental studies in the Pd-Bi-Te system indicates that michenerite crystallizes at 489 °C (Hoffman & MacLean 1976), suggesting an upper limit for the formation of NiS at approximately 489 °C. At these temperatures, crowningshieldite ( $\alpha$ -NiS) is the stable phase, and upon further cooling below 379 °C would rapidly have inverted to millerite ( $\beta$ -NiS). This is supplemented by previous studies (Kullerud & Yund 1962; Sowa *et al.* 2004; Wang *et al.* 2006), and experimental data presented herein that show  $\alpha$ -NiS to be the stable phase at temperatures in excess of 379 °C. While this regime does not provide a precise temperature at which NiS crystallizes, it provides a framework suggesting a temperature range in which NiS and the other mineral present in the assemblage may have developed. Furthermore, the effects of pressure on the stability fields of these phases must also be considered, as there is a tendency for increasing confining pressure to decrease the compositional range of sulphide solid solutions, and thus increase the temperature at

which these discrete mineral crystallize. Experimental data indicate this relationship is reflected by an increase in crystallization temperature of approximately 10 °C/kb (Kullerud *et al.* 1969).

### 1.5.2 Chemical Influences (or Lack Thereof) on Morphology

Studies have been conducted showing that chemical substitution in minerals can directly impact the crystal morphology of that mineral. For example, the length-to-width ratio of arsenopyrite ( $\text{FeAs}_{1-x}\text{S}_{1+x}$ ) correlates directly with the As:S value of a given crystal. Specifically where higher values (more S-rich) favour stout or equant crystals, and lower values (S-poor) result in the development of elongated crystals. Large variations in the As:S value are responsible for these variations, ranging from 0.73 to 1.12 (Kerestedjian 1997).

In light of this precedent, it was considered plausible that the morphological differences between millerite of magmatic *vs* hydrothermal origin could be explained by chemical differences in one of two ways: (1) With respect to the concentration of vacancies present, *i.e.* the *Me*:S value given that millerite can exhibit a defect structure ( $\text{Ni}_{1-x}\text{S}$ ); and (2) the presence of elements substituting for Ni and/or S.

Considering the effects of metal-deficiency, there is a slight difference in terms of the range and average *Me*:S values between millerite of magmatic *vs* hydrothermal origin, but the vast majority of the samples still expressed ratios near unity (*i.e.* 1:1). The field illustrated by the distribution curve for magmatic samples overlaps directly with, and is contained within the range of the hydrothermal curve, meaning that both types of millerite exhibit the same ratios, albeit with differing frequencies (Fig. 1.21). This implies that the concentration of vacancies present in all millerite is generally quite low, and the mineral is nearly stoichiometric in most instances. Furthermore, no difference is noted in the *Me*:S values for millerite from Coleman or Nickel Rim South mines (Fig. 1.19).

Similarly, when considering the effects of a substituting anion or cation, the differences are insignificant. No elements were observed to substitute for S, and only low concentrations of

Fe and Co substituted for Ni, ranging from 0.15 to 1.46 wt. % (total Fe+Co) for magmatic millerite, and from 0.59 to 4.02 wt. % (total Fe+Co) for hydrothermal millerite. There are small differences in the concentration of total Fe+Co between the two varieties, but overall the values are very similar (Fig. 1.18), and there are no significant correlations observed between chemistry, geological setting, and morphology of the crystals. Furthermore, as the ionic radii of Ni, Fe, and Co are all very similar ( $^{[5]}Ni^{2+} = 0.63 \text{ \AA}$ ,  $^{[5]}Fe^{3+} = 0.58 \text{ \AA}$ ,  $^{[5]}Co^{2+} = 0.67 \text{ \AA}$ ) (Shannon 1976), substitution amongst them would not be expected to cause significant distortions or changes to the overall millerite crystal structure. Just as was observed with reference to the *Me:S* values for millerite from Coleman and Nickel Rim South mine, there are no differences noted between the chemistry of millerite from the two mines.

It is clear, based on this information, that there is no correlation between either the stoichiometry of millerite (*Me:S* value), or the chemistry (major, minor, and trace) and the observed morphology of the crystals. Regardless of whether the millerite formed in a magmatic or hydrothermal setting, both data sets show a direct overlap amongst the samples that were analyzed, indicating that while there may be generalities applied to both environments, there exist no definitive factors to distinguish one from the other. Therefore, it is highly unlikely that fluctuations in the *Me:S* value or the substitution of certain chemical entities in millerite play a significant role in determining the external morphology of the crystals.

### *1.5.3 Structural & Genetic Influences on Morphology*

Having demonstrated that variations in chemistry, be they ones involving major, minor, or trace elements in millerite cannot be invoked to explain the observed differences in morphology of millerite from the two principle geological environments, the role and impact of the unit cell and crystal structure needs to be considered. This concept is encapsulated by The Law of Bravais wherein growth-rate anisotropy is directly related to the relative dimensions of the unit cell of a crystal, and it in this context that further discussion occurs.

The resemblance between synthetic crystals of  $\alpha$ -NiS and those from magmatic environments (*i.e.*, crystals that exhibit a platy morphology) has been noted in earlier studies (Kullerud & Yund 1962). The hypothesis of an  $\alpha \rightarrow \beta$  transition being a factor in the observed morphology of millerite from Cu-Ni-PGE footwall veins in the Sudbury area has also been proposed relatively recently (Wawrzonkowski 2015). However, beyond this proposition, which has been largely based upon conceptual evidence, no further detailed investigations to confirm the hypothesis have been undertaken until now. The Law of Bravais states that the most prominent faces of a crystal will be those parallel to shortest crystallographic axis, and based on this, crystals of crowningshieldite ( $\alpha$ -NiS) would develop with a platy morphology (similar to what is observed in the Sudbury area and other magmatic systems) as  $d_{0001} > d_{10\cdot1}$ . Such a conclusion is consistent with the findings of this current study wherein crystals of  $\alpha$ -NiS are found to develop with a pronounced platy morphology (*i.e.*, the pinacoid {0001} is found to dominate in larger crystals) as well as those from previous studies of Kullerud & Yund (1962) where synthetic crystals of  $\alpha$ -NiS adopt a platy to blocky habit.

Conversely, The Law of Bravais predicts an elongated morphology for crystals of millerite ( $\beta$ -NiS) as  $d_{0001} < d_{10\cdot10}$ . This habit is consistent with the observed acicular morphology of all millerite coming from hydrothermal occurrences (Bagrowski 1940; Dana 1949; Heyl *et al.* 1959; Ramdohr 1969; Medici 1981; Fin'ko & Mohkov 1985; Young 2011; Tauson *et al.* 2018), including those examined in the present study, and crystals of  $\beta$ -NiS produced by low-temperature synthesis (Pan *et al.* 2008).

The prominence of features indicating post-crystallization processes such as exsolution of pyrrhotite from pentlandite, rimming on magnetite grains by chalcopyrite and bornite, and the numerous complex intergrowths noted amongst PGMs and other trace minerals all suggest that cooling of the system occurred progressively. This would have permitted ample time for the complete inversion of crowningshieldite to millerite to take place (considering the low  $E_a$ , and

rapid pace at which the transformation occurs at temperatures within approximately 250 °C and 379 °C) (Wang *et al.*, 2006), providing a straightforward explanation for the ubiquitous presence of platy millerite observed within the final mineral assemblage in magmatic systems. Additionally, the pervasive development of a perfect rhombohedral cleavage along  $\{10\bar{1}1\}$ , and/or parting along the  $\{01\bar{1}2\}$  twin plane likely exacerbates the occurrence of platy crystals of millerite developing from a crowningshieldite precursor.

The correlations thus drawn between the morphology and the genetic history of millerite can be used as a first-order indication of the geological/genetic history of the associated mineral assemblage, and thus the system as a whole. The presence of platy millerite in a system is suggestive of primary magmatic textures, and the formation of the Ni-sulphide crowningshieldite at temperatures in excess of 379 °C. Conversely, a mineral assemblage containing acicular millerite can be considered as indicative of direct hydrothermal precipitation, or the alteration and recrystallization of previous Ni-bearing mineral assemblages, the millerite having been derived through hydrothermal activity. These latter processes probably occur under conditions of low temperature, likely <250 °C.

#### *1.5.4 Comments on the Stability & Inversion of NiS*

While the  $\alpha$ - and  $\beta$ -NiS polymorphs are often referred to as the high- and low-temperature polymorphs respectively, this is not an entirely accurate connotation. While temperature is generally regarded as the most significant influence on the stability of one structure type over the other, the stability fields for the two phases are also strongly influenced by pressure. Under atmospheric conditions, the  $\alpha \rightarrow \beta$  transition occurs at 379 °C, but this boundary experiences a sharp decrease in temperature with increasing confining pressure (Fig. 1.24) (Sowa *et al.* 2004). However, considering the large range of pressure over which the  $\alpha \rightarrow \beta$  transition is observed to decrease, it is unlikely that pressure would exert measurable control on the transition temperature for the systems of interest. Graterol & Naldrett (1971) suggested formation of the

magmatic Ni-Fe ores of the Marbridge mine (Québec) at approximately 0.1 GPa (1 kbar), with this pressure reflecting essentially no change in the transition temperature of NiS. The highest estimated temperature of formation for hydrothermal millerite (250 °C) according to the data of Holwell *et al.* (2017) is plotted in Figure 1.24 and intersection with the  $\alpha$ - $\beta$  boundary occurs at ~6 GPa. Barring the presence of unfathomably high confining pressures, this suggests that all NiS forming in hydrothermal systems crystallizes as millerite, and that in all near-surface geological environments, pressure will have little to no effect on the  $\alpha \rightarrow \beta$  transition of NiS.

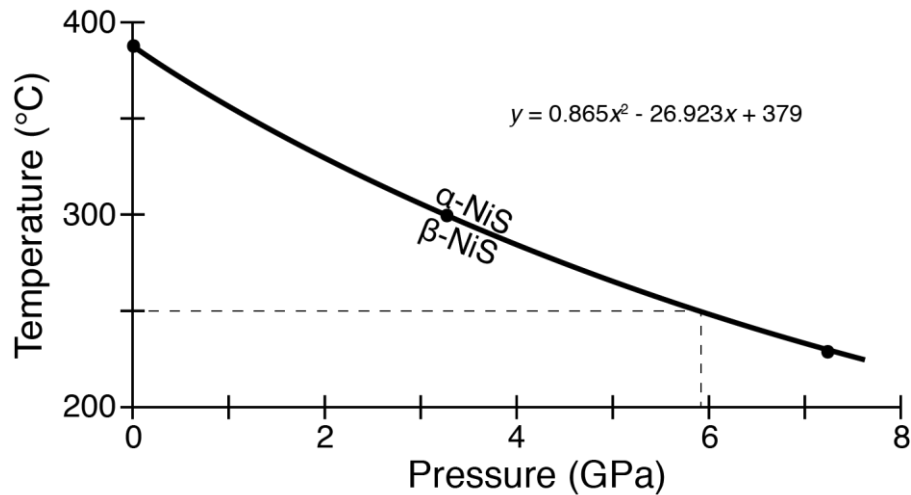


**FIG. 1.24.** Diagram illustrating the negative correlation between the  $\alpha \rightarrow \beta$  transition temperature and the pressure of the system based on the data of Sowa *et al.* (2004). The original data (black dots) have been fit with a polynomial line of best fit (equation shown on graph) representing the boundary between the stability fields of the NiS polymorphs. The dashed line indicates the highest estimated temperature of formation for hydrothermal NiS based on the data of Holwell *et al.* (2017).

In an impure system (*i.e.* natural setting) the presence of impurities such as Fe and Co may also exercise control on the  $\alpha \rightarrow \beta$  inversion. The maximum concentration of Fe that may be present in  $\alpha$ -NiS has not been precisely determined, but chemical analyses of the only known occurrence of crowningshieldite indicate the presence of 10 % *apfu* of Fe (Smith *et al.* 2018). This value is much higher than any of the total Fe+Co concentrations observed in either

magmatic or hydrothermal millerite over the course of this study, and suggest that  $\alpha$ -NiS can accommodate much more Fe than can  $\beta$ -NiS. In turn, this means that during the inversion of a more Fe-rich  $\alpha$ -NiS, the presence of more Fe than can be incorporated into the  $\beta$ -NiS will be accommodated by the exsolution of an additional Fe-rich phase. While the potential Fe concentrations of  $\alpha$ -NiS in magmatic systems are unknown, there is empirical evidence suggesting the exsolution of an Fe-bearing compound represented by samples of millerite from the Sudbury area. Rarely, an association of pentlandite and millerite is observed wherein pentlandite occurs as elongated inclusions concentrated along polysynthetic twin lamellae in millerite. The presence of pentlandite along compositional planes within another Ni-sulphide suggests that it may have formed *via* exsolution during the phase inversion of crowningshieldite to millerite. Exsolution of pentlandite from millerite occurring in magmatic systems has also been suggested by Graterol & Naldrett (1971). However, it is unlikely that this process exercises control on the stability of  $\alpha$ -NiS, or the rate at which the  $\alpha \rightarrow \beta$  transition occurs. The determining factor in this phase transition has been attributed to the total  $Me:S$  content of the system, in that at higher  $fS_2$  the formation of metal-rich embryos for the nucleation of the metal-rich (stoichiometric)  $\beta$ -NiS is more difficult, resulting in a higher  $E_{act}$  (Wang 2005b). Therefore, while the presence of Fe in the initial  $\alpha$ -NiS and the resultant exsolution of pentlandite may complicate the inversion process (from a mineralogical standpoint), it does not influence the  $E_{act}$  of the reaction, and thus does not aid in the stabilization of  $\alpha$ -NiS at temperatures below 379 °C.

## 1.6 CONCLUSIONS

Based on the information presented herein regarding the crystal chemistry of millerite from magmatic and hydrothermal systems, it is concluded that:

(1) Millerite from magmatic environments exhibits a distinctive platy morphology, whereas millerite from hydrothermal systems forms as acicular crystals. Magmatic millerite often forms large masses exhibiting a perfect  $\{10\bar{1}1\}$  cleavage, and frequent, multiple  $\{01\bar{1}2\}$  twins.

(2) Substitution of elements amongst the samples observed is limited to Fe+Co for Ni, and no substitution was observed for S. The average composition for millerite of magmatic origin is  $(\text{Ni}_{0.974}\text{Fe}_{0.007}\text{Co}_{0.004})_{\Sigma 0.985}\text{S}$ , whereas that for millerite of hydrothermal origin is  $(\text{Ni}_{0.934}\text{Co}_{0.021}\text{Fe}_{0.013})_{\Sigma 0.969}\text{S}$ . Average *Me*:S values are 0.985 for magmatic millerite ( $n = 180$ ) and 0.969 for hydrothermal millerite ( $n = 145$ ). Hydrothermal material does exhibit a slightly greater range in both chemistry and stoichiometry than magmatic material, but the differences between the two are relatively minor, and the direct overlap between the fields indicates no correlation between morphology and chemistry.

(3) Crystals of  $\alpha$ -NiS are easily synthesized using CVT, with crystals exhibiting the forms pinacoid  $\{0001\}$  and the dipyrmaid  $\{10\bar{1}1\}$ . The dipyrmaid  $\{10\bar{1}1\}$  was generally dominant on smaller crystals, while the pinacoid  $\{0001\}$  was the dominant form on larger crystals, suggesting that the morphological significance between the two forms share an inverse relationship as crystal size increases. In general, crystal developed a platy morphology with increasing size, in agreement with what is observed amongst samples of millerite from magmatic systems.

(4) The occurrence of platy millerite in magmatic systems is the result of paramorphism between the NiS polymorphs crowningshieldite ( $\alpha$ -NiS) and millerite ( $\beta$ -NiS). The estimated temperatures ( $\sim 500$  °C?) of the footwall Cu-Ni-PGE environments suggest that NiS initially crystallizes as crowningshieldite, this mineral developing as coarse, platy crystals. This was followed by the inversion of crowningshieldite to millerite, which takes place through a reconstructive  $\alpha \rightarrow \beta$  phase transition beginning at 379 °C and reaches completion due to the slow and progressive cooling of the host system. As this is a solid-state reaction, the external platy morphology of the crowningshieldite is retained, and the subsequent occurrence of platy millerite in magmatic system is likely exacerbated by the development of a perfect rhombohedral cleavage on  $\{10\bar{1}1\}$  and/or parting on the  $\{01\bar{1}2\}$  twin plane.

## 1.7 REFERENCES

- AMES, D.E., DAVIDSON, A., & WODICKA, N. (2008) Geology of the Giant Sudbury Polymetallic Mining Camp, Ontario, Canada. *Economic Geology* **103**, 1057–1077.
- BAGROWSKI, B.P. (1940) Occurrence of Millerite at Milwaukee, Wisconsin. *American Mineralogist* **25**, 556–559.
- BINNEWIES, M., GLAUM, R., SCHMIDT, M., & SCHMIDT, P. (2012) *Chemical Vapor Transport Reactions*. 1<sup>st</sup> Edition. De Gruyter, 645 pp.
- BINNEWIES, M., GLAUM, R., SCHMIDT, M., & SCHMIDT, P. (2013) Chemical Vapor Transport Reactions - A Historical Review. *Zeitschrift Fur Anorganische Und Allgemeine Chemie* **639**, 219–229.
- BRAVAIS, A. (1850) *On the Systems Formed by Points Regularly Distributed on a Plane or in Space*. 113 pp.
- BRAVAIS, A. (1866) *Études crystallographiques*. 1<sup>st</sup> Edition. Gauthier-Villars, 290 pp.
- BUDDINGTON, A.F., & LINDSLEY, D.H. (1964) Iron-Titanium Oxide Minerals and Synthetic Equivalents. *Journal of Petrology* **5**, 310–357.
- DANA, E.S. (1949) *A Textbook of Mineralogy*. 4<sup>th</sup> Edition. Wiley, 851 pp.
- EINSTEIN, T.L. (2015) Equilibrium Shape of Crystals. *In Handbook of Crystal Growth*. 1<sup>st</sup> Edition, Elsevier, 215-264.
- ENDO, Y., & SUNAGAWA, I. (1973) Positive and Negative Striations in Pyrite. *American Mineralogist* **58**, 930–935.
- FIN'KO, V.I., & MOHKOV, A.V. (1985) Supergene Millerite from the Lateritic Weathering Zone of a Cuban Serpentinite. *International Geology Review* **27**, 1365–1369.
- FLEET, M.E., & PAN, Y.M. (1994) Fractional Crystallization of Anhydrous Liquid in the System Fe-Ni-Cu-S, With Applications to Magmatic Sulfide Deposits. *Geochimica Et Cosmochimica Acta* **58**, 3369–3377.
- GIBBS, G.V., DOWNS, R.T., PREWITT, C.T., ROSSO, K.M., ROSS, N.L., & COX, D.F. (2005) Electron density distributions calculated for nickel sulfides millerite, vaesite, and heazelwoodite and nickel metal: A case for the importance of Ni-Ni bond paths for electron transport. *Journal of Physical Chemistry B* **109**, 21788–21795.
- GOLDSCHMIDT, V.M. (1913a) *Atlas der Krystallformen I*. Vols. 1-9, Vol. 1. 1<sup>st</sup> Edition. Universitätsbuchhandlung Heidelberg, 244 pp.
- (1913b) *Atlas der Krystallformen II*. Vols. 1-9, Vol. 2. 1<sup>st</sup> Edition. Universitätsbuchhandlung Heidelberg, 251 pp.
- (1916) *Atlas der Krystallformen III*. Vols. 1-9, Vol. 3. 1<sup>st</sup> Edition. Universitätsbuchhandlung Heidelberg, 247 pp.

- (1918a) *Atlas der Krystallformen IV*. Vols. 1-9, Vol. 4. 1<sup>st</sup> Edition. Universitätsbuchhandlung Heidelberg, 133 pp.
- (1918b) *Atlas der Krystallformen V*. Vols. 1-9, Vol. 5. 1<sup>st</sup> Edition. Universitätsbuchhandlung Heidelberg, 123 pp.
- (1920) *Atlas der Krystallformen VI*. Vols. 1-9, Vol. 6. 1<sup>st</sup> Edition. Universitätsbuchhandlung Heidelberg, 144 pp.
- (1922a) *Atlas der Krystallformen VII*. Vols. 1-9, Vol. 7. 1<sup>st</sup> Edition. Universitätsbuchhandlung Heidelberg, 159 pp.
- (1922b) *Atlas der Krystallformen VIII*. Vols. 1-9, Vol. 8. 1<sup>st</sup> Edition. Universitätsbuchhandlung Heidelberg, 149 pp.
- (1923) *Atlas der Krystallformen IX*. Vols. 1-9, Vol. 9. 1<sup>st</sup> Edition. Universitätsbuchhandlung Heidelberg, 128 pp.
- GRATEROL, M., & NALDRETT, A.J. (1971) Mineralogy of Marbridge No. 3 & No. 4 Nickel-Iron Sulfide Deposits - with Some Comments on Low Temperature Equilibration in Fe-Ni-S System. *Economic Geology* **66**, 886–900.
- GRICE, J.D., & FERGUSON, R.B. (1974) Crystal structure refinement of Millerite (beta -NiS). *The Canadian Mineralogist* **12**, 248–252.
- HARTMAN, P. (1958) The Equilibrium Forms of Crystals. *Acta Crystallographica* **11**, 459–464.
- HARTMAN, P., & PERDOK, W.G. (1955a) On the Relations Between Structure and Morphology of Crystals. I. *Acta Crystallographica* **8**, 49–52.
- (1955b) On the Relations Between Structure and Morphology of Crystals. II. *Acta Crystallographica* **8**, 521–524.
- (1955c) On the Relations Between Structure and Morphology of Crystals. III. *Acta Crystallographica* **8**, 525–529.
- HEYL, A.V., MILTON, C., & AXELROD, J.M. (1959) Nickel Minerals from Near Linden, Iowa County, Wisconsin. *American Mineralogist* **22**, 995–1009.
- HOFFMAN, E.L., & MACLEAN, W.H. (1976) Phase relations of michenerite and merenskyite in the Pd-Bi-Te system. *Economic Geology* **71**, 1461–1468.
- HOLWELL, D.A., ADEYEMI, Z., WARD, L.A., SMITH, D.J., GRAHAM, S.D., MCDONALD, L., & SMITH, J.W. (2017) Low temperature alteration of magmatic Ni-Cu-PGE sulfides as a source for hydrothermal Ni and PGE ores: a quantitative approach using automated mineralogy. *Ore Geology Reviews* **91**, 718–740.
- KEPLER, J. (1611) *The Six-Cornered Snowflake*. 74 pp.
- KERESTEDJIAN, T. (1997) Chemical and morphological features of arsenopyrite, concerning its use as a geothermometer. *Mineralogy and Petrology* **60**, 231–243.

- KIRKPATRICK, R.J. (1975) Crystal-Growth from Melt - A Review. *American Mineralogist* **60**, 798–814.
- KITAKAZE, A., SUGAKI, A., ITOH, H., & KOMATSU, R. (2011) A revision of phase relations in the system Fe-Ni-S from 650 °C to 450 °C. *Canadian Mineralogist* **49**, 1687–1710.
- KULLERUD, G., & YUND, R.A. (1962) The Ni-S System and Related Minerals. *Journal of Petrology* **3**, 126–175.
- KULLERUD, G., YUND, R.A., & MOH, G.H. (1969) Phase Relations in the Cu-Fe-S, Cu-Ni-S, and Fe-Ni-S Systems. In *Magmatic Ore Deposits - A Symposium Vol. 4. Society of Economic Geologists*, 323–343.
- MEDICI, J.C. (1981) The Halls Gap Millerite Locality. *Rocks & Minerals* **56**, 104–108.
- MUNGALL, J.E. (2007) Crystallization of magmatic sulfides: An empirical model and application to Sudbury ores. *Geochimica Et Cosmochimica Acta* **71**, 2809–2819.
- MUROWCHICK, J.B., & BARNES, H.I. (1987) Effects of Temperature and Degree of Supersaturation on Pyrite Morphology. *American Mineralogist* **72**, 1241–1250.
- NELLES, E.W. (2012) Genesis of Cu-PGE-rich Footwall-Type Mineralization in the Morrison Deposit, Sudbury. *Unpublished M.Sc. Thesis*, Laurentian University, Sudbury, 96 pp.
- PAN, Q., HUANG, K., NI, S., YANG, F., & HE, D. (2008) Synthesis of flower- and rod-like nickel sulfide nanostructures by an organic-free hydrothermal process. *Materials Research Bulletin* **43**, 1140–1147.
- PEREGOEDOVA, A., & OHNENSTETTER, M. (2002) Collectors of Pt, Pd and Rh in a S-poor Fe-Ni-Cu sulfide system at 760 degrees C: Experimental data and application to ore deposits. *Canadian Mineralogist* **40**, 527–561.
- PUPIN, J.P. (1980) Zircon and Granite Petrology. *Contributions to Mineralogy and Petrology* **73**, 207–220.
- RAJAMANI, V., & PREWITT, C.T. (1974) The crystal structure of millerite. *The Canadian Mineralogist* **12**, 253–257.
- RAMDOHR, P. (1969) *The Ore Minerals and Their Intergrowths*. 1<sup>st</sup> Edition. Elsevier, 1193 pp.
- SCHÄFER, H. (1964) *Chemical Transport Reactions*. 1<sup>st</sup> Edition. Academic Press, 182 pp.
- SCHMIDT, P., BINNEWIES, M., GLAUM, R., & SCHMIDT, M. (2013) Chemical Vapor Transport Reactions—Methods, Materials, Modelling. *Advanced Topics on Crystal Growth*, 80 pp.
- SHANNON, D. (1976) Revised effective ionic radii and systematic studies of interatomic distances in halides and chalcogenides. *Acta Crystallographica Section A* **32**, 751-767.

- SMITH, E.M., SHIRLEY, S.B., NESTOLA, F., BULLOCK, E.S., WANG, J., RICHARDSON, S.H., & WANG, W. (2016) Large gem diamonds from metallic liquid in Earth's deep mantle. *Science* **354**, 1403–1405.
- SMITH, E.M., NESTOLA, F., PASQUALETTO, L., ZORZI, F., SECCO, L., & WANG, W. (2018) Crowningshieldite, IMA 2018-072. CNMNC Newsletter No. 45, October 2018, page 1043. *European Journal of Mineralogy* **30**, 1037–1043.
- SOWA, H., AHSBAHS, H., & SCHMITZ, W. (2004) X-ray diffraction studies of millerite NiS under non-ambient conditions. *Physics and Chemistry of Minerals* **31**, 321–327.
- SPARKS, J.T., & KOMOTO, T. (1963) Neutron Diffraction Study of NiS. *Journal of Applied Physics* **34**, 1191–1192.
- STENO, N. (1669) *De solido intra solidum naturaliter contento*. 86 pp.
- SUNAGAWA, I. (1953) *Variations in Crystal Habit of Calcite*. Geological Survey of Japan, 66 pp.
- (1957) *Variations in Crystal Habit of Pyrite*, Geological Survey of Japan, 41 pp.
- (1999) *Growth and Morphology of Crystals*.
- TAUSON, V.L., LIPKO, S.V., SMAGUNOV, N.V., KRAVSTOVA, R.G., & ARSENT'EV, K.Y. (2018) Distribution and segregation of trace elements during the growth of ore mineral crystals in hydrothermal systems: geochemical and mineralogical implications. *Russian Geology and Geophysics* **59**, 1718–1732.
- TRAHAN, J., GOODRICH, R.G., & WATKINS, S.F. (1970) X-ray diffraction measurements on metallic and semiconducting hexagonal NiS. *Physical Review B-Solid State* **2**, 2859–2863.
- VAUGHAN, D.J., & CRAIG, J.R. (1978) *Mineral Chemistry of Metal Sulfides*. 1<sup>st</sup> Edition. Cambridge University Press, 493 pp.
- (1997) *Ore Microscopy & Ore Petrography*. 2<sup>nd</sup> Edition. John Wiley & Sons, Ltd., 434 pp.
- VUORELAINEN, Y., HUHMA, A., & KLI, A.H.A. (1964) Sederholmite, wilkmanite, kullerudite, mäkinenite and trüstedite, five new nickel selenide minerals. *Bulletin de la Commission géologique de Finlande* **215**, 113–126.
- WANG, H. (2005a) Decomposition and phase transition of NiS/Ni<sub>1-x</sub>S in the temperature range 323-973 K. *Journal of Sulfur Chemistry* **26**, 233–243.
- (2005b) Kinetics of some solid-state reaction of metal sulfides. *Unpublished Ph.D. Thesis*, University of Adelaide, Adelaide, 121 pp.
- WANG, H.P., PRING, A., NGOTHAI, Y., & O'NEILL, B. (2006) The kinetics of the  $\alpha \rightarrow \beta$  transition in synthetic nickel monosulfide. *American Mineralogist* **91**, 171–181.

WAWRZONKOWSKI, P. (2015) The Mineralogy, Textures, and Formation of Cu-Ni-Fe-S Footwall Stringers in the McCreedy Mine, Onaping. *Unpublished B.Sc. Thesis*, Laurentian University, Sudbury, 54 pp.

WILSON, T.D. (2004) *Strangers to Ourselves*. 1<sup>st</sup> Edition. Harvard University Press, 272 pp.

YOUNG, B. (2011) Millerite from Coldberry Gutter and Great Egglehope Teesdale, County Durham. *Northumbrian Naturalist: Transactions of the Natural History Society of Northumbria* **70**, 111–114.

# **Chapter 2:**

## **Orientation Contrast & Twinning in Millerite from the Sudbury Basin**

## ABSTRACT

Samples of millerite ( $\beta$ -NiS) from several mines in Sudbury, Ontario, Canada exhibited contrasting grey-tones when examined *via* BSEI. Subsequent chemical analyses of the material failed to detect any measurable chemical variation between the regions, indicating that the differing response under BSEI was not a result of differences in  $Z_{avg}$ , and thus chemical composition. This suggests an alternative mechanism for the observed BSE response. The most prominent of such zones are interpreted as polysynthetic twinning of the millerite on  $\{01\bar{1}2\}$ , where lamellae exhibit rhythmic alternation between bright and dark zones. EBSD analyses of the lamellae confirmed that they are  $\{01\bar{1}2\}$  twins, and suggested that crystallographic orientation is responsible for the observed grey-tones. The stopping power of incident electrons between the adjacent twins differs owing to the presence of continuous channels along  $[10\bar{1}0]$  in millerite, eliciting a subdued BSE response in that and symmetrically equivalent orientations, resulting in a darker image. Simultaneously, the BSE response oblique to  $[10\bar{1}0]$  (adjacent twins) produces a stronger BSE response and generates a brighter image. The observed grey-tone variation is independent of chemistry, and is the result of orientation contrast *via* electron channelling, and the prominence of this feature in millerite is attributed to its highly anisotropic structure, and comparatively high backscatter coefficient ( $\eta$ ). The development of secondary  $\{01\bar{1}2\}$  twins in millerite is attributed to a post-crystallization increase in pressure arising through two potential mechanisms. (1) The application of external pressure ( $P_{ext}$ ) arising from metamorphism or a deformation event. (2) The application of internal pressure ( $P_{int}$ ) resulting from a volumetric expansion accompanying the  $\alpha \rightarrow \beta$  phase transformation in NiS. The development of twins may be the result of either one of these processes, or a combination of the two.

## 2.0 INTRODUCTION

Over the past several decades, the use of scanning-electron microscopy (SEM) has become an integral component in the analysis of geological materials, augmenting hand-sample observations and those made with the polarizing-light microscope. Direct uses of the SEM range from the micron to submicron levels, and include textural observations, secondary optical effects [*e.g.*, cathodoluminescence (CL)], and crystallographic investigations [*e.g.*, electron-backscatter diffraction (EBSD)] along with qualitative and quantitative chemical analyses. Of these, the use of backscattered-electron imaging (BSEI) likely receives the greatest attention as it is commonly used to interpret variations in the average chemical composition among minerals or changes in chemistry within a single mineral (*i.e.* chemical zonation). In terms of chemical variation,  $Z_{\text{avg}}$  is typically considered as the only parameter influencing the concentration of backscattered electrons produced through electron beam-mineral interactions, the total flux being influenced by both the energy and time over which the process occurs. Such changes in chemistry are commonly recorded as grey-tone variations, wherein the intensity of the grey-tone is taken to be proportional to the flux of BSE being produced. While chemical variations in a mineral are indeed a major factor influencing BSE production, there exist additional factors that can equally impact on BSE production, the most important of these being *orientation contrast* (OC). The latter, simply put, encompasses the idea that the orientation of a crystal relative to an incident electron beam can impact BSE production. The role of OC on BSE production, and hence imaging effects, has been noted previously (Neubert & Rogaschewski 1980), but has been relatively underappreciated in regards to studies of geological materials.

During the course of a study on millerite from Cu-Ni-PGE footwall veins in the Sudbury area (Ontario, Canada), noteworthy variations in BSE production were observed. These suggested the presence of important chemical variations, but subsequent chemical analyses failed to reveal any variations in the major-, minor-, and trace-element chemistries sufficient to explain the observed BSE variations. It was subsequently determined (and supported by EBSD methods

reported herein) that the actual process behind the observed variations in BSE production are not attributed to changes in the  $Z_{\text{avg}}$ , but instead, a combination of crystal-structure features including twinning and grain orientation. As the effect and influence of OC on BSE production is rarely reported in the mineralogical and geological literature, it was deemed important to provide a review of the relationship between OC and BSE production and to apply this to the observations made on millerite. In this contribution the impact of OC on BSE production in millerite is clarified, its use in the characterization of observed twinning is provided, and brief comments on the mineralogical and geological implications of OC in the genesis and evolution of platy millerite from Cu-Ni-PGE veins are provided.

## 2.1 BACKGROUND

### 2.1.1 Backscattered-Electron Imaging

Production of BSE in any material is largely controlled by the backscatter coefficient ( $\eta$ ), which in turn is a function of the average chemical composition of that material. The relationship between chemistry and  $\eta$ , also known as *Z*-contrast (Prior *et al.* 1999) (where  $Z_{\text{avg}}$  represents the average atomic number of the material), is expressed as (Reimer 1998):

$$\eta = -0.0254 + 0.016Z - 1.86 \times 10^{-4}Z^2 + 9.3 \times 10^{-7} Z^3 \quad \text{Eq. 2.1}$$

Simply put, as the  $Z_{\text{avg}}$  of a mineral increases, so does the proportion of BSE produced by that mineral (Fig. 2.1). However, it has been shown that the production of BSE can also be influenced by both the nature of the crystal structure of the material being analyzed and the orientation of said crystal structure with respect to that of the incident electron beam (Lloyd 1987). The combination of the latter effects is collectively referred to as OC, the most important aspect of which is termed *electron channelling*. Quite simply, electron channelling refers to the process that occurs when the path of incident electrons is coincident with a major crystallographic

direction (such as a zone or plane) in a material, these directions coinciding with major changes in atomic density. When coincident with a major crystallographic direction, the stopping power (atomic density) is comparatively lower, and incident electrons penetrate more deeply into the structure of the crystal, (Fig. 2.2). This significantly decreases the chance of these electrons being backscattered towards the detector, and results in a comparatively darker image under BSEI.

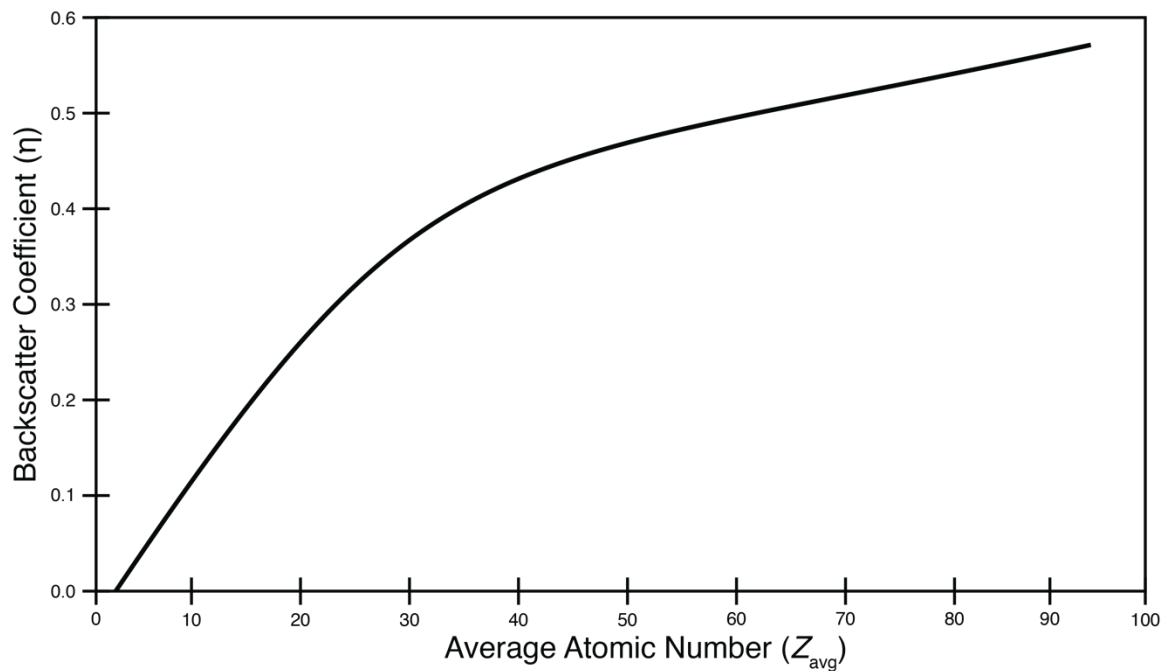


**FIG. 2.1.** Graphical representation of the theoretical correlation between  $\eta$  and  $Z_{avg}$  for normal incidence at an accelerating voltage of 20 kV. This function only considers the value of  $Z_{avg}$  for a given material, and does not take into account orientation effects such as electron channelling (after Reimer 1998).

Electron channelling is likely to be more characteristic of materials having layered crystal structures, simply as the stopping power within layers is significantly greater than that between layers (*i.e.*, the atomic density is not isotropic). The implication of OC then is that the  $\eta$  for crystalline materials (including minerals wherein crystal structure features such as channels are developed within the crystal structure) must be considered as being anisotropic with respect to the orientation of the lattice relative to the incident electrons (Joy *et al.* 1982; Zaefferer & Elhami

2014). It thus follows that the relative roles of OC in BSE production must be considered as inherent to all crystalline materials and thus, OC plays a role in affecting the total BSE production from a given mineral. In general, the relative role of  $Z$ -contrast and OC are not equivalent, with the impact of  $Z$ -contrast generally far exceeding that of OC in BSE production and thus  $\eta$ , for most materials during normal scanning. However, in cases where  $Z_{avg}$  is effectively fixed (as in a chemically homogeneous mineral), those with amenable crystal-structure features and having suitable orientations presented, OC can become the dominant process influencing BSE production. In such cases, important secondary features can be revealed, including grain boundary development, twinning, aggregate development, *etc.*

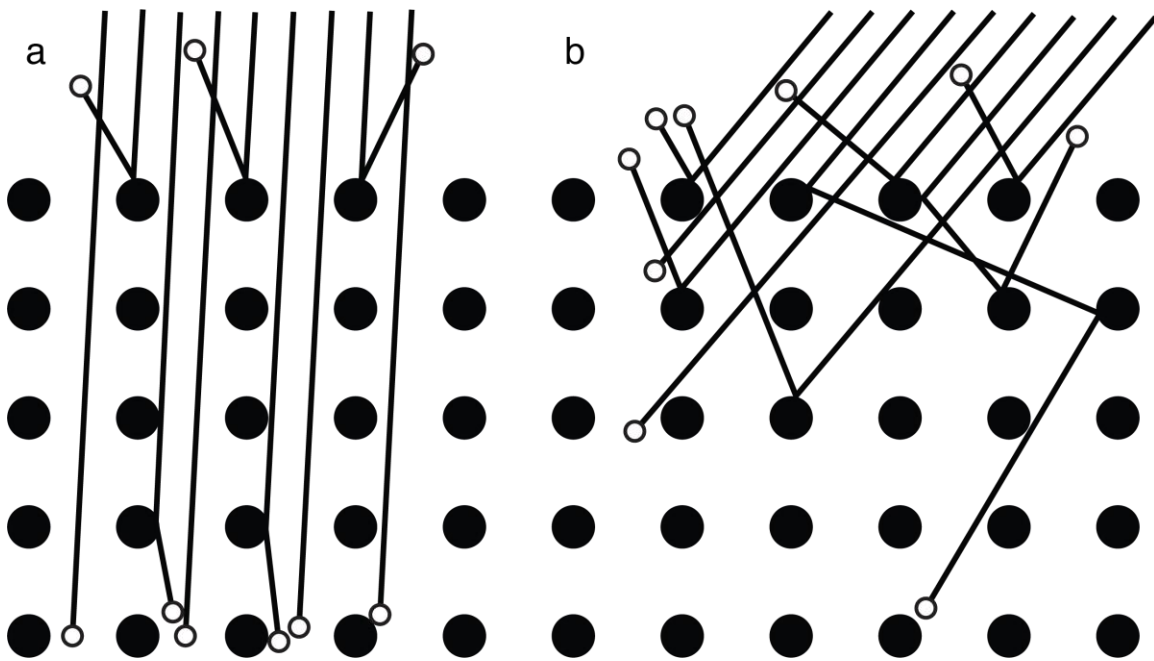


**FIG. 2.2.** Depiction of electron channelling through the particle theory model using a hypothetical 2D crystal lattice. Atomic nuclei are represented by the black spheres, electrons as open spheres, and the electron paths as black lines. (a) Incident electrons penetrate deeply into the sample along open channels between atomic nuclei. The resultant backscattering of fewer electrons produces a darker image. (b) Incident electrons are oblique to crystallographic channels, and most are reflected back towards the detector, resulting in a brighter image (after Kamaladasa & Picard 2010).

### 2.1.2 Sample Locations

Millerite-bearing samples used in this study were obtained from operating mines in the Sudbury area, including Coleman (Vale; North Range) and Nickel Rim South (Glencorp; East Range), and the Morrison deposit (KGHM; North Range). A total of 102 samples were collected over several levels including the 1470 to 1740 m levels at Coleman mine, the 1200 to 1680 m levels of the Nickel Rim South mine, and the 1250 to 1400 m levels of the Morrison deposit. All samples were obtained from Cu-Ni-PGE veins hosted in the footwall of the Sudbury Igneous Complex (SIC), these being considered as products of fractionated Hz-Iss melt that was injected into mafic and felsic gneisses that constitute the footwall environment. These can be described as narrow veins ranging, from 30 to 100 cm in width, where the mineral assemblage is dominated by chalcopyrite and millerite, with lesser pyrrhotite, pentlandite, bornite, magnetite, and a host of trace constituents (platinum-group minerals, alloys, native Au, *etc.*). As part of a broader study investigating the occurrence and formation of millerite in the footwall environment, samples from the Morrison deposit (McCreedy East mine) were previously examined, results of which are presented in Wawrzonkowski (2015). Reference will be made to some of the observations and findings of this study throughout the course of this present contribution.

## 2.2 METHODS

### 2.2.1 Chemistry

Chemical data were collected using a JEOL-6400 scanning electron microscope (SEM) *via* energy-dispersive spectroscopy (EDS) with an accelerating voltage of 20 kV and a current of 1.0 nA. Standards that were employed include: chalcopyrite ( $\text{FeK}\alpha$ ,  $\text{CuK}\alpha$ ,  $\text{SK}\alpha$ ), Ni wire ( $\text{NiK}\alpha$ ), and Co wire ( $\text{CoK}\alpha$ ). Only Ni, Fe, Co, and S were analyzed for, as no other elements were detected in preliminary scans. Data acquisition and processing were facilitated using INCA analytical software (Oxford Instruments, 2011). Chemical data were obtained *via* line scans with

an average length of ~150  $\mu\text{m}$ , a beam diameter of ~5  $\mu\text{m}$ . A carbon coat was applied to all polished sections prior to analysis *via* SEM-EDS.

### 2.2.2 Electron Backscatter Diffraction

Electron backscatter diffraction data (EBSD) were collected using an HKL system interfaced with the same JEOL-6400 system operating with an accelerating voltage of 20 kV, a current of ~3.0 nA, and a sample-to-detector working distance of 15 mm, with the sample tilted at 70° with respect to the electron beam. All thin sections were polished using colloidal silica for ~1 h to ensure a high-quality, defect-free, flat surface to the millerite being examined and the system was calibrated prior to data collection using Si. Frames were collected for 20 ms for a total of 64 frames per image. Maps reflecting the orientations of individual grains were constructed using a step size of 1  $\mu\text{m}$ , and individual Kikuchi patterns were indexed using five bands per pattern with a mean angular deviation (MAD) cutoff of 1.0. Channel 5 software was used to collect EBSD patterns along with pattern indexing and matching (Day & Trimby 2004). All analyses were conducted with uncoated polished thin sections, as the metallic nature of the samples minimized the effects of charging, and the absence of a carbon coat increased the quality of the resultant Kikuchi patterns.

## 2.3 OBSERVATIONS

Preliminary observations made on the millerite-bearing samples from each of the locations sampled showed a high degree of homogeneity in terms of mineralogy, modal abundances, and textures. As such, observations are presented on a single sample, being representative for that mine.

### 2.3.1 Hand Samples

The sample from Nickel Rim South mine has dimensions 20.0  $\times$  10.5  $\times$  9.5 cm and consists of 95% millerite, 2.5% chalcopyrite, 2.5% bornite, and trace amounts of magnetite based

on visual estimates (Fig. 2.3a). Millerite occurs primarily as anhedral coarse grains with a distinct platy morphology, these ranging from 0.5 to 2.0 cm in diameter, and exhibiting a pronounced rhombohedral  $\{10\bar{1}1\}$  cleavage. Locally, millerite occurs as massive aggregates up to 5 cm in diameter that are composed of granular crystals  $\leq 1$  mm in diameter. Chalcopyrite occurs throughout the main mass, enveloping millerite crystals, while bornite occurs only along footwall vein selvages, in margins up to 1 cm thick.

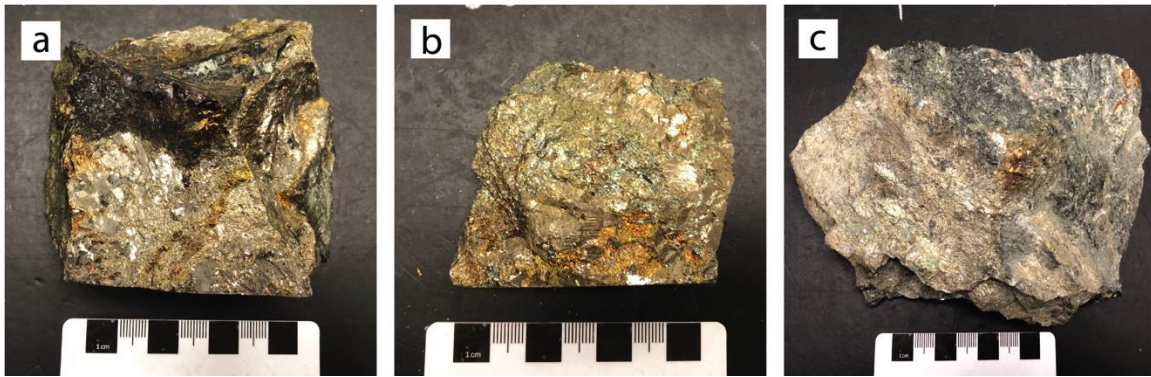


**FIG. 2.3.** Hand sample images of millerite examined in this study. Scale for all images is in cm. (a) Coarse mlr and with locally granular texture and minor ccp from Nickel Rim South mine. Note the planar cleavage face in the lower left-hand side of the sample. (b) Coarse mlr and accessory ccp from Coleman mine. Note the presence of planar cleavage faces. (c) Coarse mlr with interstitial ccp from the Morrison deposit. Note the lower lustre of this sample when compared to that in (a) and (b).

The sample from Coleman mine has dimensions  $13.5 \times 7.0 \times 3.5$  cm and consists primarily of chalcopyrite and millerite in approximately 1:1 proportions (Fig. 2.3b). The chalcopyrite is massive, exhibiting no notable features or discernable morphology, while millerite occurs as clusters of large plates, these ranging from 1.0 to 2.5 cm in diameter. The millerite crystals do not apparently exhibit any preferred orientation, *i.e.*, their pronounced basal surfaces are randomly oriented. Millerite grains exhibit rhombohedral  $\{10\bar{1}1\}$  cleavage, as well as the presence of numerous parallel lamellae  $\leq 1$  mm thick, that exhibit sharp boundaries between adjacent striae. Even in hand sample, individual lamellae can be readily discerned owing to relatively large variations in bireflectance that they exhibit. The sample from the Morrison deposit has dimensions  $14.5 \times 10.0 \times 5.5$  cm and consists of 90% millerite and 10% chalcopyrite

(Fig. 2.3c). Millerite occurs as coarse grains up to 3.0 cm in diameter, these exhibiting a pervasive rhombohedral  $\{10\bar{1}1\}$  cleavage. Cleaved surfaces of the millerite crystals are noticeably duller (lower reflectivity) than those from the other two localities, the cause of which is not known. Chalcopyrite is interstitial to millerite and its modal abundance increases towards the vein selvages.

### 2.3.2 Petrography of Millerite

All polished thin sections used in this study, regardless of the mine they were obtained from, are generally dominated by millerite (70 to 90 modal %), with lesser amounts (10 to 30 modal %) of chalcopyrite, pentlandite, bornite, and magnetite, with trace amounts ( $\leq 0.5$  modal %) of sphalerite, galena, hessite, gold, and PGM.

Millerite from Nickel Rim South mine occurs primarily as equant, sub-rounded to sub-angular grains that are on average 0.5 mm in diameter (Fig. 2.4a). As noted in the macroscopic observation of millerite samples, the granular texture is only observed locally in certain samples. However, the polished thin sections prepared in this case were expressly taken from these regions in order to provide a direct comparison between the two textures of millerite observed over the course of this study. These grains are typically devoid of any internal textures and often meet at triple junctions, suggesting possible recrystallization. Only rarely was the presence of parallel lamellae with sharp boundaries ranging from 30 to 200  $\mu\text{m}$  in thickness observed within the crystals. Individual grains exhibit a strong, distinct pleochroism between brass-yellow and bronze-yellow under PPL, and do not uniformly go extinct under XPL (Fig. 2.4b) indicating that they are randomly oriented.

Millerite from Coleman mine occurs as very large ( $\geq 1$  cm) grains that exhibit a pervasive rhombohedral  $\{10\bar{1}1\}$  cleavage and the presence of numerous lamellae (Fig. 2.4d). The lamellae range from  $< 1$  to 350  $\mu\text{m}$  in thickness, and two distinct types are observed, these termed Type I and Type II based on thickness, continuity and, interpreted order of formation. Type I lamellae

dominate the sample, appear as striae ranging from 10 to 350  $\mu\text{m}$  in thickness, and alternatively go into extinction when observed under XPL (Fig. 2.4e). Such lamellae are strongly reminiscent of the albite twins that characterize plagioclase feldspar. Type II lamellae are less pronounced, but still common, and consist of fine striations, ranging from  $<1$  to 10  $\mu\text{m}$  in thickness, and are observed to be oriented at an angle of approximately  $20^\circ$  to the Type I lamellae. Both Type I and Type II lamellae are optically continuous, but only along their respective lengths. While Type I lamellae span the entire length of the individual millerite grain, Type II lamellae are truncated at their intersections with the Type I lamellae (Fig. 2.4d,e). As such, the Type I lamellae are considered to have formed before the Type II lamellae. The Type I lamellae show strong, distinct pleochroism from brass-yellow to bronze yellow and despite a rigorous (yet gentle) polishing regime, topographical relief exists between adjacent lamellae, possibly due to the differential hardness of grains in differing orientations. Both Type I and Type II lamellae can be considered as polysynthetic twins formed by reflection across  $\{01\bar{1}2\}$ , a twin law that has commonly been referenced for millerite (Dana 1949; Ramdohr 1969; Grice & Ferguson 1974).

Millerite from the Morrison deposit develops as large ( $>1$  cm) grains exhibiting a pervasive rhombohedral cleavage similar to the material from Coleman mine, although the development of twins is less pronounced (Fig. 2.4g). Specifically, the observed twin/lamellae boundaries are more irregular and when present, these boundaries are observed to be undulatory (*i.e.* not sharp) and do not appear to sharply follow any single plane [although the lamellae do share a common orientation as evidenced by a common extinction angle (Fig. 2.4h)].

### 2.3.3 Electron Microscopy

As previously noted, preliminary observations of individual millerite grains using BSE imaging revealed notable grey-tone differences, these initially being interpreted to indicate intragrain differences in  $Z_{\text{avg}}$  (*i.e.*, mineral chemistry). Such variations were observed in all the millerite

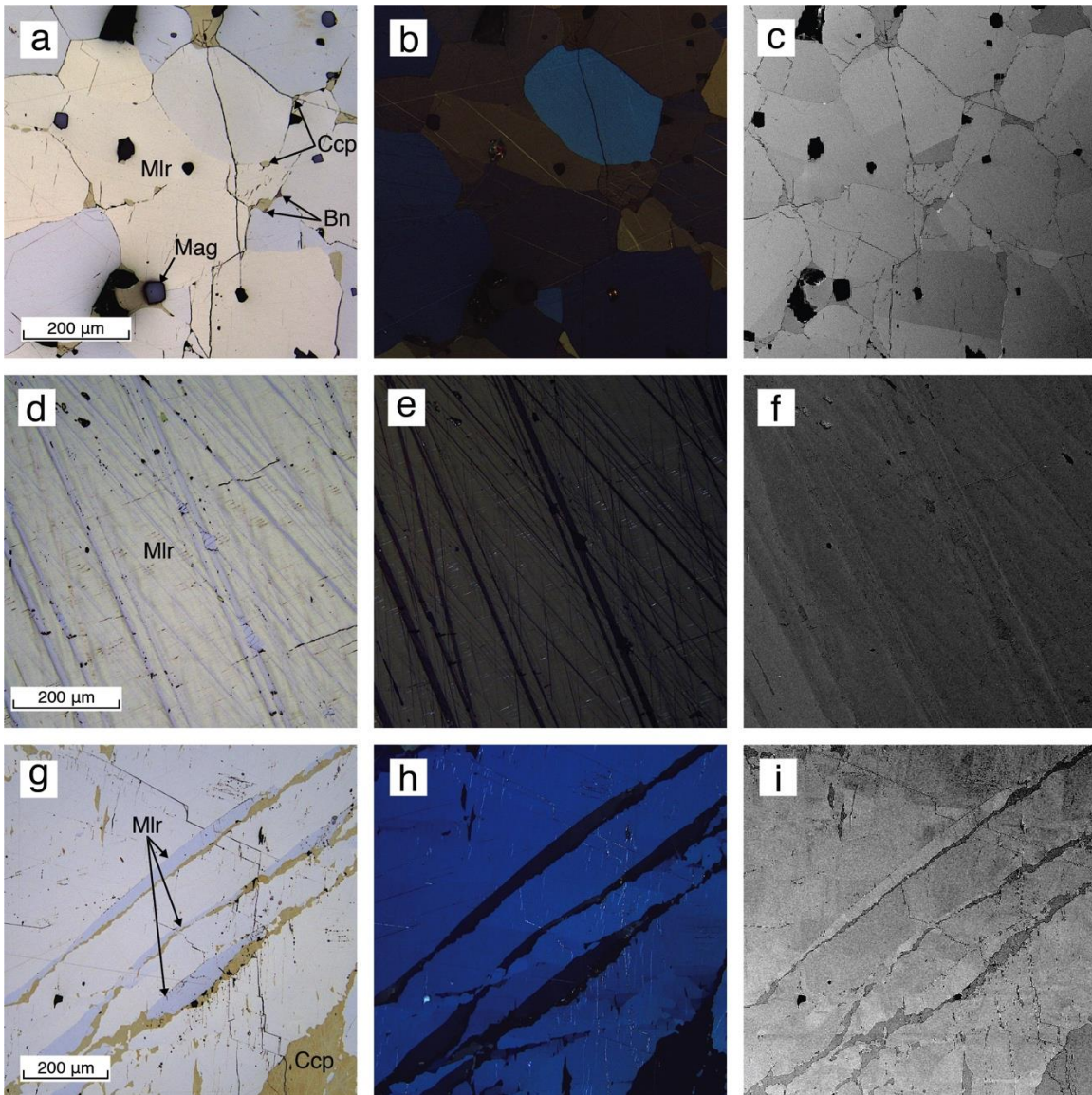


**FIG. 2.4.** Images in each row depict the same area of a thin section under plane-polarized light (PPL), cross-polarized light (XPL), and backscatter electron imaging (BSE) L-R. (a) Polished thin section (PTS) under from Nickel Rim south consisting primarily of equant grains of mlr with minor ccp, mag, and bn (PPL). Note the strong birefractive response of the mlr and the tendency for grains to meet at triple junctions. (b) Same section (XPL) where the grain boundaries are more easily visible owing to the strong anisotropic nature of the mlr. (c) Same section (BSE) illustrating the greytone variations between grains. (d) PTS from Coleman consisting of coarse, platy mlr with minor pn and ccp (PPL). Note the presence of two sets of lamellae: a thicker, dominant set (I), and a thinner subordinate set (II). (e) Same section (XPL) where the presence of the subordinate lamellae is accentuated. (f) Same section (BSE) illustrating the rhythmic nature of the greytone response of the lamellae under normal scanning. (g) PTS from Morrison consisting of coarse, platy mlr and minor ccp (PPL). Note the rhombohedral cleavage, and the relatively poor development of the lamellae. (h) Same section (XPL) where the subgrain boundaries in the mlr are more evident. Note how the lamellae exhibit simultaneous extinction, indicating they share a common orientation. (i) Same area imaged with BSE, illustrating the differences in BSE production as reflected in the grey-tone variations present. It is clear from this image that numerous subgrains have developed through the sample.

examined, regardless of the sample location and included both adjacent grains (Fig. 2.4c) as well as those that are considered to be twinned based on reflected-light observations (Fig. 2.4f,i).

Differences in BSE production, as reflected in grey-tone variations, are consistent with the observations made through reflected-light microscopy. While these variations were observed in all the millerite examined in the study, they were most prominent in material from Coleman mine. Furthermore, comparisons between the same region of a given polished thin section using reflected-light and electron microscopy clearly indicates that the grain boundaries observed (as denoted by pleochroism and anisotropism) correlate precisely with those defined by grey-tone differences (Fig. 2.4). This is particularly evident in the case of material from Coleman mine, where the occurrence of polysynthetic twinning is prevalent (Fig. 2.4d-f).

## 2.4 RESULTS

### 2.4.1 Chemistry

Although grey-tone variations are visible in many BSE images of millerite from the three mines (Fig. 2.5) data from EDS analyses made on the millerite in this study indicates all material is close to end member in composition, regardless of the mine and stratigraphic level that it was obtained from, *i.e.*, it close to NiS in composition, with only minor concentrations of Fe (< 1 wt. % or < 0.02 *apfu*) Co (<0.30 wt. % or < 0.005 *apfu*) being noted (Table 2.1). The high-degree of chemical homogeneity in the millerite examined is reflected in: (1) The consistency in the *Me*:S values of the millerite. Analyses indicate that the millerite is near stoichiometric, an important fact considering that NiS may be non-stoichiometric. (2) That it shows very low levels of Ni ↔ Fe + Co substitution, *i.e.* the millerite near end member composition (Fig. 2.6). Furthermore, no other elements beyond those noted (Ni, Fe, Co, and S) were detected. As the *Z* for Ni, Fe, and Co are all similar ( $Z_{\text{Ni}} = 28$ ,  $Z_{\text{Fe}} = 26$ , and  $Z_{\text{Co}} = 27$ ), this implies that the observed difference in BSE production and the resulting grey-tones produced cannot be strictly explained by variations in the

chemistry of millerite. Another explanation for the observations must exist; one not strictly based on chemistry.

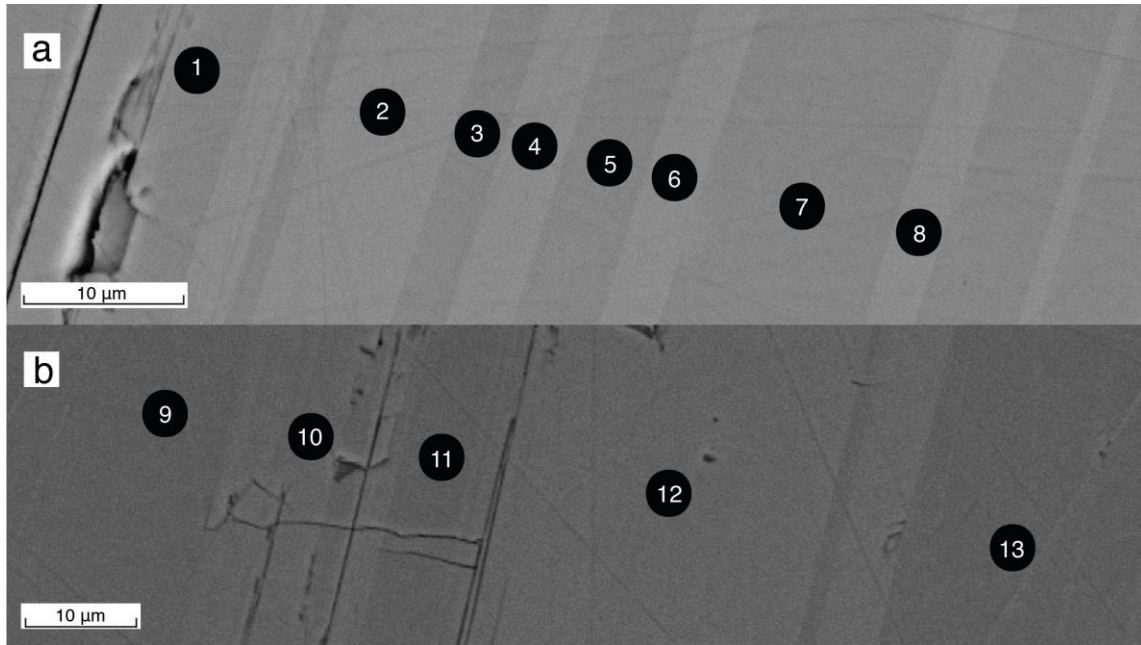


**FIG. 2.5.** BSE images of material collected at Coleman mine, indicating where SEM-EDS analyses were made across the lamellae (Table 2.1). Both (a) and (b) represent images of different areas taken from the same polished thin section. Note the grey-tone variations that are present, despite there being no associated chemical differences.

**Table 2.1: Mineral Chemistry of Millerite from Coleman Mine**

Spot	Element (wt. %)				Total	<i>apfu</i> (S=1)		
	Ni	Fe	Co	S		Ni	Fe	Co
1	63.01(26)	0.97(5)	0.12(6)	35.81(12)	99.91	0.961	0.016	0.002
2	63.56	0.94	0.10	35.98	100.58	0.965	0.015	0.002
3	63.31	0.84	0.16	35.85	100.16	0.965	0.013	0.002
4	63.53	0.94	0.09	35.84	100.40	0.969	0.015	0.001
5	63.79	0.97	0.24	35.86	100.86	0.972	0.016	0.004
6	63.57	0.99	0.15	35.87	100.58	0.968	0.016	0.002
7	63.63	0.89	0.07	35.89	100.48	0.969	0.014	0.001
8	63.37	0.95	0.18	35.94	100.44	0.963	0.015	0.003
9	63.80	0.90	0.22	35.91	100.84	0.971	0.014	0.003
10	63.41	0.95	0.15	35.78	100.29	0.968	0.015	0.002
11	63.71	0.90	0.19	35.73	100.53	0.974	0.014	0.003
12	63.88	0.92	0.08	35.58	100.46	0.981	0.015	0.001
13	63.70	0.90	0.12	35.86	100.58	0.970	0.014	0.002
<b>Avg.</b>	63.56	0.93	0.14	35.84	100.47	0.969	0.015	0.002
<b>Min.</b>	63.01	0.84	0.07	35.58	99.91	0.961	0.013	0.001
<b>Max</b>	63.88	0.99	0.24	35.98	100.86	0.981	0.016	0.004

\*Brackets indicate the error (+/-) associated with the respective analyses.

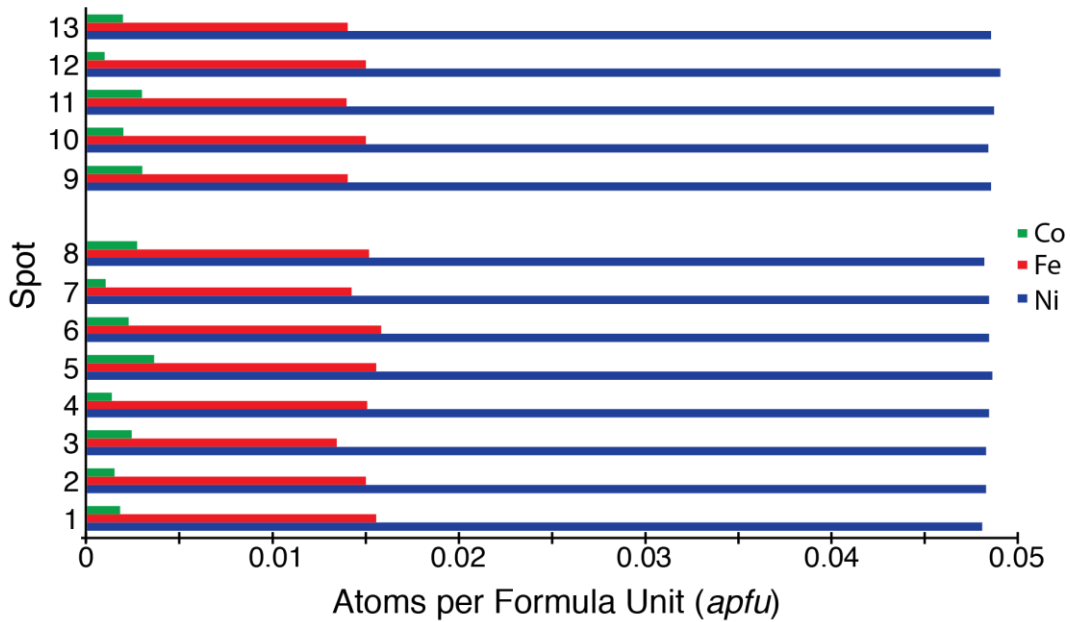


**FIG. 2.6.** Bar graph representing the total *apfu* of cations in millerite (normalized to  $S = 1$ ) in terms of Co, Fe, and Ni/20 corresponding to the data presented in Table 2.1. The Ni values have been scaled ( $/20$ ) in order to enable visual representation of all three elements. Note the minimal variability between individual profiles.

#### 2.4.2 Electron Backscatter Diffraction

Observations made on millerite-bearing hand samples and polished thin sections clearly indicate that millerite grains exhibit different crystallographic orientations. Evidence for this includes: (1) randomly orientated cleavage fragments in hand samples; (2) variations in colour from brass-yellow to bronze-yellow seen between adjacent grains under plane-polarized light; and (3) for lamellae features in the millerite to exhibit differential patterns in extinction consistent with twinning. In order to (1) investigate the nature of the variations in BSE production as a function of orientation; (2) evaluate the relationship of the inferred twins with the BSE variations; and (3) verify whether the lamellae truly represent multiple twins, EBSD data were collected using material from Coleman mine. Such material was chosen principally because it was found to exhibit the strongest evidence for the presence of polysynthetic twinning.

Initial EBSD analyses were made on grains where Type I twins were developed and Type II twins absent. This was done because preliminary EBSD analyses showed that when both types of twins were present in the same grain, indexing was highly problematic. In particular,

individual Type II twins could not be clearly resolved from one another presumably owing to their small size ( $\leq 1\mu\text{m}$ ). Therefore, focus was made on the Type I twins, these being the most well developed, most recognizable, and most easily discernable from one another.

Preliminary observations made on the Type I twins indicated that the EBSD patterns for millerite are well resolved. The sharpness of the Kikuchi bands suggests: (1) the millerite has a highly ordered atomic structure; and (2) the surface of the grains that were analysed is well polished and devoid of significant surface flaws. Individual lamellae appear to exhibit crystallographic continuity, *i.e.* Kikuchi patterns were not observed to vary significantly from point to point, consistent with them being twins. The high quality of the intragrain patterns that were produced was observed in all those obtained within an individual twin component. While EBSD analyses show that within lamellae the same crystallographic orientation is retained, between lamellae there is an angular variation with respect to  $c$  ( $\sim 20^\circ$ ). These results are entirely consistent with the presence of polysynthetic twinning in the millerite examined.

With the presence of polysynthetic twinning established, the data were then used to determine/verify the crystallographic relationship (*i.e.* the twin law) between adjacent twin components. Quantification of the orientation distribution of the lamellae was conducted using a 1200-point ( $\mu\text{m}^2$ ) map collected over a  $60 \times 20 \mu\text{m}$  area. A step size of  $1 \mu\text{m}$  was used, and the area examined included at least six discernible Type I twins. A total of 1185 out of 1200 of the patterns obtained were indexed successfully (98.75% success rate), matches being made using the EBSD pattern calculated using the crystal structure parameters of Grice & Ferguson (1974). To reinforce the alternating nature in the orientation of the twins, a false-colour overlay of a BSE image of the area over which the EBSD map was collected is presented in Fig. 2.7. As can be seen, there are two distinct coloured bands, each representing a specific crystallographic orientation. The continuity within a band, along with the regular oscillation between two, indicates the millerite occurs in two, alternating crystallographically unique orientations.

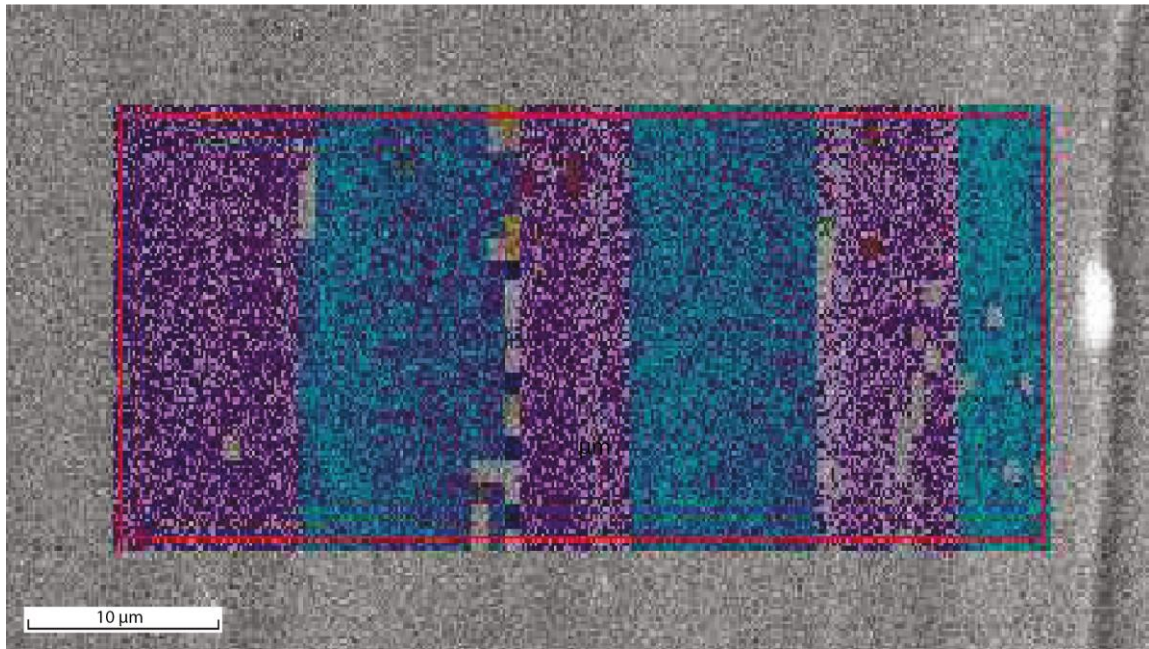


**FIG. 2.7.** False colour overlay of a 1200-point EBSD map on a BSE image of millerite from Coleman mine. A total of 98.75% of the points on this map were successfully indexed as millerite. Areas that have been coloured are successfully indexed. The blue and purple zones correspond to areas with different crystallographic orientations, and the points within each zone have a similar orientation to those around them. Note the discrete boundaries between the grains, and the alternation between blue and purple lamellae interpreted as polysynthetic twins.

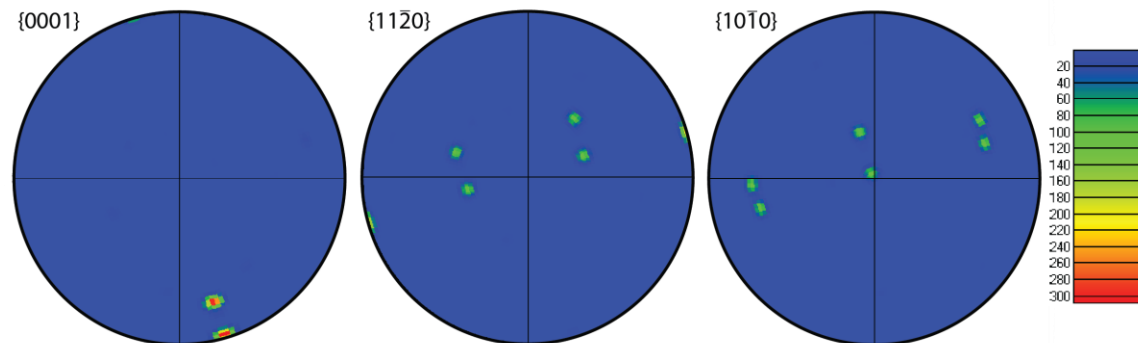


**FIG. 2.8.** Pole figures showing data collected from the EBSD map obtained on millerite from Coleman mine. The stereonets have been contoured in order to group the individual points. Hotter colours indicate a greater density of points, as indicated by the scale on the right-hand side of the figure. The projection on  $\{0001\}$  indicates two groups of points, one on the primitive circle, and another where the  $c$ -axis is tilted by  $\sim 20^\circ$ , these represent the twins viewed along  $[1\bar{1}00]$  and  $[1\bar{1}0\bar{5}]$  respectively. The projections on  $\{11\bar{2}0\}$  and  $\{10\bar{1}0\}$  also reflect the difference in  $c$ -axis orientation, but also show the positions of symmetrically equivalent crystallographic orientations resulting from the  $60^\circ$  repetitions caused by the 3-fold rotational axis in millerite.

The orientations of the twins are plotted on stereonet in Fig. 2.8 using the poles to each. The data are contoured to include all points within  $2^\circ$  and the presence of relatively tight groupings, in conjunction with the map in Fig. 2.7, provides unequivocal evidence that: (1) there is crystallographic continuity between alternating twins; (2) the continuity does not exist between adjacent twins; and (3) the precise angular relationship between adjacent twins varies only slightly from  $\sim 20^\circ$ , which can be measured directly from the pole figures.

The approximate value of  $\sim 20^\circ$  refers to the orientation of the twin *c*-axis with respect to the host *c*-axis, and is in agreement with the measured interfacial angle of  $21^\circ 23\frac{1}{2}'$  provided by Palache & Wood (1904) from their observation of  $\{01\bar{1}2\}$  twins in millerite.

## 2.5 DISCUSSION

### 2.5.1 Orientation Contrast

The positions and features of these twins are consistent when viewed with both reflected-light and BSE imaging, and their presence clearly explains why there are no associated changes in chemistry during normal scanning (*i.e.*, the millerite is chemically homogeneous and very close to end-member NiS). What remains unclear is the cause of the differences in BSE production (grey-tone variations) when moving across the twins. To explore this, it is necessary to understand the crystal structure of millerite, and how electron-beam interactions can be impacted by this, bearing in mind that twin lamellae represent zones of crystallographic continuity.

Since twin lamellae correspond to regions of crystallographic continuity, it follows that they also necessarily constitute regions having equivalent atomic environments when being viewed in a given orientation. The latter point is critical; in that it means that the interactions between the incident electrons and the mineral will necessarily be equivalent within a specific twin domain and between domains sharing the same exact (or symmetrically equivalent) crystallographic orientation. Results from the EBSD section of this study indicate that those twin components exhibiting the lowest flux of BSE (*i.e.*, the darker grey-tones; Fig 2.5) correspond to

those regions wherein the crystal is being viewed along  $[\bar{1}100]$ ,  $\pm 2^\circ$ . It is critical to note that this equates to viewing the crystal structure of millerite along  $[\bar{1}100]$ , which corresponds to open channels in the lattice being presented (Fig. 2.9a). This will mean that incident electrons impinging on a grain with such an orientation will encounter a comparatively lower stopping power, relative to electrons impinging on a grain oriented oblique to this zone axis (consider Fig. 2.2). This will result in a relatively lower flux of BSE, leading to darker grey tone when viewed under BSE imaging (Fig 2.5a). Conversely, those twin components corresponding to orientations that are oblique to the  $[\bar{1}100]$  direction (Fig. 2.9b) will encounter a comparatively higher stopping power, leading to a relatively greater flux of BSE, thus resulting in zones of lighter grey

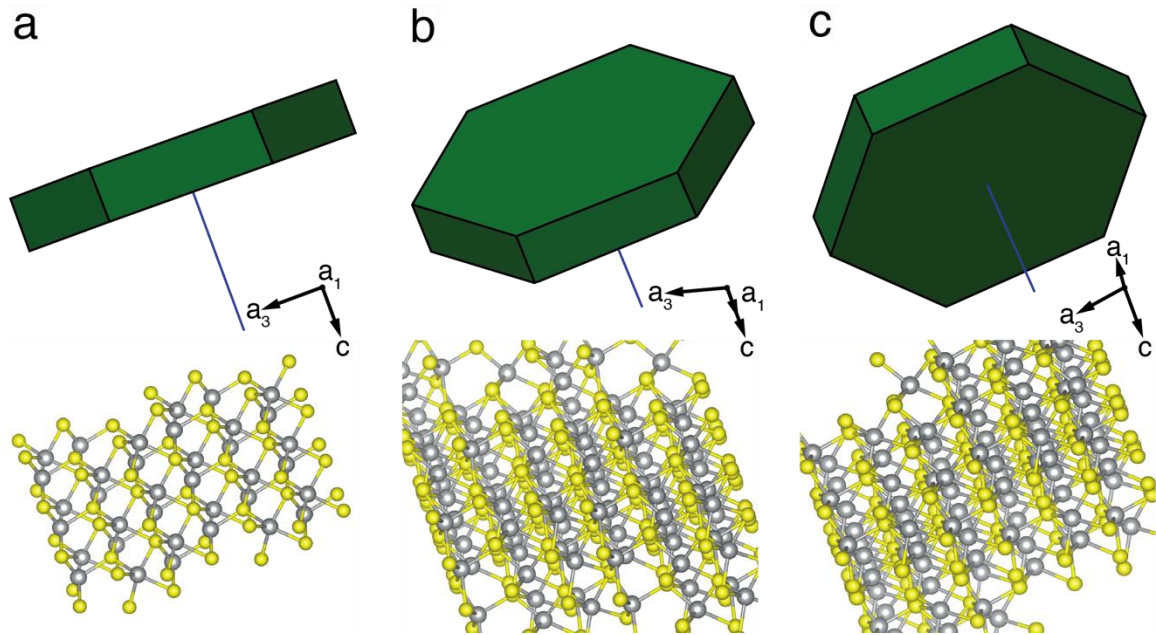


**FIG. 2.9.** Corresponding crystal and crystal-structure representations of millerite viewed in specific orientations. These correlate with the two principle orientations determined using EBSD. (a) Crystal viewed along  $[\bar{1}100]$ , corresponding to the orientation observed by the twins exhibiting the weak BSE response (darker). Note the presence of comparatively large, open, and continuous channels. These are expected to result in a relatively low atomic density encountered by incident electrons travelling in this direction. (b) Crystal viewed along  $[1\bar{1}05]$ . (c) Crystal viewed along  $[110\bar{5}]$ . Both sections shown in (b) and (c) are representative of the orientation observed in the twins exhibiting a stronger BSE response (brighter). In such orientations, there are no open channels along which incident electrons may travel, and the atomic density is comparatively greater to that in (a) Other symmetrical equivalents of these orientations will also produce the same result.

tones (Fig 2.5). In this way, the production of BSE and resulting grey-tones when millerite is observed under BSE imaging directly correlates to the crystallographic zones that are being viewed, with darker grey-tones corresponding to  $[\bar{1}100]$  and brighter grey-tones corresponding to  $[\bar{1}105]$ .

While the OC effect provides an explanation for the observed variations in BSE production, and the resultant grey-tones, a complete understanding of the effect likely includes a combination of factors:

(1) The fact that there is an inherently greater contrast between the proportion of channelled and non-channelled electrons in materials with relatively high  $\eta$ . The channelling effect is dependent on the occurrence of a low degree of high-angle scattering of electrons along specific directions of a crystal structure. This condition is often satisfied when electrons are incident along a major crystallographic direction, as the stopping power is lower along this direction than oblique to it (in comparison to an isotropic medium). As such, the effect is largely independent of the  $\eta_{\text{avg}}$  or the  $Z_{\text{avg}}$  of the material as a whole, but is instead a function of the local  $\eta$  along a specific direction in a crystal. For example, if two materials with different  $Z_{\text{avg}}$  but identical structures are considered, the proportion of electrons backscattered by the lattice will be similar along equivalent directions that coincide with open channels, but will differ significantly along directions oblique to these channels. In other words, the stopping power approaches zero along open channels and may be largely (but not entirely) independent of the  $Z_{\text{avg}}$  of the material, but when oblique to these specific directions,  $\eta$  directly correlates (and will be influenced largely) with the  $Z_{\text{avg}}$  of the material. Therefore, materials with a higher  $Z_{\text{avg}}$  have a greater potential to exhibit variation in BSE production resulting from OC should the path of incident electrons be coincident with a major crystallographic direction of the material, as the difference in stopping power along channels vs oblique to channels is comparative greater.

(2) The anisotropy of the material in terms of atomic density with respect to crystallographic orientation will also play a role in the production of BSE. The crystal structure of millerite is layered along [0001], with the atomic density in this direction being less than in the plane parallel to it owing to the presence of six-membered rings in (0001) that form continuous channels along [0001] (Grice & Ferguson 1974). Therefore, there is likely to be a strong, orientational contrast in  $\eta$  depending on whether the section of millerite is oriented parallel to or perpendicular to [0001]. The highly anisotropic nature of the crystal structure of millerite will also result in a strong dependence of  $\eta$  on the OC associated with polysynthetic twins formed by reflection across  $\{01\bar{1}2\}$ , as this introduces orientational variation into what would otherwise be a crystallographically continuous grain.

### 2.5.2 *Twinning*

The occurrence of twins in millerite has been previously described, but never precisely quantified. Palache & Wood (1904) and Dana (1949) describes the rhombohedron  $\{01\bar{1}2\}$  as a gliding plane along which artificial twins may be formed, and Grice & Ferguson (1974) note the material they studied (from Marbridge mine) was “twinned by reflection across  $\{01\bar{1}2\}$  which is the common twin law for millerite”, although no specific reference was provided. Ramdohr (1969) also notes the presence of two distinct types of twins being present in millerite stating, “the lamellae themselves are often lamellated”; his observation likely reflects the presence of Type I and Type II twins observed in this present study as two distinct generations of twins. The work of Palache & Wood (1904), Dana (1949), and Ramdohr (1969) all attribute the development of the twins in millerite to a post-crystallization increase in pressure, so the resultant twins should thus be considered a secondary feature, although the basis for this is unclear. It is curious that the polysynthetic twinning in millerite strongly resembles that in calcite, the latter being commonly attributed to post-crystallization deformation (Palache & Wood 1904; Deer *et al.* 1963).

Although millerite and calcite appear unrelated in terms of their chemistry and respective crystal structures, certain similarities do exist between the two minerals. For example, both are trigonal in symmetry and possess a rhombohedral lattice, with millerite ( $\beta$ -NiS) crystallizing in the space group  $R3m$  (No. 160) and calcite crystallizing in  $R\bar{3}c$  (No. 167). Furthermore, both minerals can be considered as having layered crystal structures, with the layering occurring along  $[0001]$ . In calcite, layers of  $^{19}\text{Ca}$  alternate with trigonal planar  $\text{CO}_3$  groups, while in millerite layers of  $^{58}\text{Ni}$  alternate with layers of  $^{32}\text{S}$ . It perhaps should not be surprising then, that both may show similar twinning, *i.e.* reflection across  $\{01\bar{1}2\}$ . This presumably being the case, then the process by which twins develop in both may be similar.

It should be noted that the twin law for calcite, as given, is derived from the morphological cell, which represent a smaller hexagonal cell that is  $\frac{1}{4}$  the height of the true structural cell along  $c$  (Barber & Wenk 1979). Thus, the true twin law for calcite (when referencing the structural cell) is reflection across  $\{01\bar{1}8\}$ . The morphological cell is typically used to discuss cleavage, twins, and other morphological features in calcite as many of these observations were conducted prior to the advent of X-ray crystallography. However, diffraction patterns cannot be properly indexed using the morphological cell, and the structural cell is used in these instances. For the sake of simplicity and in drawing comparisons with millerite, the twin law will be given as reflection across  $\{01\bar{1}2\}$ , referencing the morphological cell for calcite.

The  $\{01\bar{1}2\}$  twinning in calcite is attributed to shear displacement along  $\{01\bar{1}2\}$  (Barber & Wenk 1979). It results from a dislocation-glide mechanism, and occurs readily with low critical shear stress and its development is virtually independent of temperature (Motohashi *et al.* 1976). This type of twinning is ubiquitously associated with deformation, and is commonly observed in many rocks containing recrystallized calcite (Burkhard 1993).

It must be noted that until now, there have been no formal studies documenting the nature of the twinning process in millerite, for example, in terms of orientation, magnitude, active slip-

system, and dislocation mechanisms, *etc.* Initial recognition of twinning on  $\{01\bar{1}2\}$  was based solely upon macroscopic observations of crystals, and measurements of interfacial angles (Palache & Wood 1904). In this sense, the process of mechanism(s) behind the potential development of twinning in millerite has remained unknown. By extension, it remains unclear as to whether the twinning is a primary feature developed during crystallization or a product of post-crystallization process(es). It is important to note then, that the EBSD data presented herein both support and corroborate the well-accepted notion that twinning in millerite commonly occurs *via* reflection across  $\{01\bar{1}2\}$ .

It is worth repeating that an increase in pressure, potentially resulting from deformation, has been invoked as the cause of twinning in millerite (Ramdohr 1969). As such, the development of twins in millerite may also be related to deformation and if so, one of two (or possibly both) processes may be considered. These could include: (1) application of external pressure ( $P_{\text{ext}}$ ) during deformation; and (2) application of internal pressure ( $P_{\text{int}}$ ) *via* volumetric expansion during a phase inversion.

In case of (1), which invokes  $P_{\text{ext}}$ , the development of the twinning is not a growth-related feature but a post-crystallization one, wherein the formation of these twins is directly attributed to the application of stress during deformation. This is analogous to the development of deformation twins in calcite, which may be considered as products of recrystallization (Burkhard 1993). The millerite examined in this study shows evidence for the development of triple junctions, sub-grains along boundaries, and disruption of the internal fabric present, all of which are consistent with deformation. In particular, millerite from Nickel Rim South mine shows the strongest such evidence of deformation in that all the indicators listed are present. It is interesting to note that while the millerite from Nickel Rim South mine shows signs of deformation, the remaining internal fabric in these samples exhibits curved and/or disrupted twins, suggesting that additional periods of deformation may have occurred after twin development, or that the rocks experienced a comparatively higher degree of deformation.

In the case of scenario (2),  $P_{\text{int}}$  is considered as the primary force responsible for the development of twins, which occurs either independently, or largely independent of, external forces. Instead, an increase in confining or internal pressure, attributable to the inversion of  $\alpha$ -NiS to  $\beta$ -NiS that coincides with a volume expansion, is considered to be the primary mechanism resulting in the observed twins. While both high-temperature ( $\alpha$ -) and low-temperature ( $\beta$ -) NiS are known experimentally, millerite ( $\beta$ -NiS) was considered to be the only natural form until the recent discovery of crowningshieldite ( $\alpha$ -NiS) as inclusions in a diamond (Smith *et al.* 2018). The high-temperature form ( $\alpha$ -NiS) has long been known to exist as a synthetic material at temperature above 379 °C (Kullerud & Yund 1962). The  $\alpha \rightarrow \beta$  transition in NiS occurs at 397 °C at 1 atm, with the  $\beta$ -structure stable and the  $\alpha$ -structure metastable below this temperature (Wang *et al.* 2006). It is a solid-state transformation, which is accompanied by: (1) an inversion of the lattice parameters  $a$  and  $c$ ; and (2) a concomitant increase in the volume of the unit cell by 1.78 %. As it is a solid-state conversion, this means that any  $\alpha$ -NiS trapped within a solidified matrix (as would be the case for the NiS that crystallized within Cu-Ni-PGE veins at temperatures  $>379$  C°) would be expected to convert to  $\beta$ -NiS during the cooling process. This, in turn, would be expected to result in a relative increase in  $P_{\text{int}}$ , owing to the volume change associated with the transformation. Previous studies of NiS inclusions in glass have shown that the volumetric expansion accompanying the  $\alpha \rightarrow \beta$  phase transition can result in a significant pressure increase, resulting in cracking and failure of the glass (Barry & Ford 2001). These findings support the notion that an increase in  $P_{\text{int}}$  could then induce the polysynthetic twinning that is observed in the millerite analyzed over the course of this study. In this sense, the polysynthetic twinning developed in the millerite must be considered as a post-crystallization process.

The occurrence of  $\{01\bar{1}2\}$  twins in millerite is most prominently observed in large ( $>1$  cm), optically continuous crystals that show little to no evidence of deformation. If these twins are to be considered secondary (*i.e.* resulting from post-crystallization processes), it is plausible

that the primary mechanism driving the development of these twins is an increase in  $P_{\text{int}}$  resulting from a volumetric expansion accompanying the  $\alpha \rightarrow \beta$  phase transition in NiS. However, considering the ease with which these twins can be induced in millerite, such as with a knife edge as illustrated by Palache & Wood (1904), they may have also been generated by relatively low confining pressures ( $P_{\text{ext}}$ ) that would not have left any other evidence of deformation in either the millerite itself or the chalcopyrite matrix (which itself is easily deformable). Samples of millerite that exhibited clear evidence of deformation (*i.e.*, triple junctions, sub-grain development, *etc.*) rarely exhibited twinning, and if it was present the lamellae were curved and/or discontinuous. This suggests that while twins may have initially developed in these samples, the twinning was influenced by subsequent deformation, which itself may have erased such evidence. Therefore, it cannot be stated with certainty as to whether the development of  $\{01\bar{1}2\}$  twins in millerite is the result of strictly  $P_{\text{ext}}$  or  $P_{\text{int}}$ , only that both scenarios can be considered as possible mechanisms for their development.

### 2.5.3 Notes on Orientation Contrast in Geological Materials

The use of BSEI in the geological realm is often restricted to  $Z$ -contrast, with  $\eta$  being correlated solely with the chemistry of a sample, and contrast in this response interpreted to be representative of areas of different chemical composition. However, as has been shown in the case of millerite,  $\eta$  may also be strongly dependent on the orientation of the samples, and the incidence of electrons along certain crystallographic directions may result in the occurrence of a strong channelling effect that can either enhance or depress BSE production. The geological literature does not provide reference to the occurrence of OC in millerite, but considering the prominence with which it occurs in samples observed over the course of this investigation, it is likely much more common than has been reported to date. Furthermore, the structure of millerite appears to be particularly conducive to producing such effects, and it is highly probable that other minerals with similar crystal-structure features such as strong layering in one direction, as is

common in the NiAs-type structure (or derivatives thereof) that is adopted by many sulphides (including pyrrhotite) and related minerals may also exhibit OC more readily than others. In general, it is likely that this phenomenon is more common in the geological realm than has been reported to date, and is exacerbated in minerals with relatively high  $Z_{avg}$  and strongly anisotropic structures. Therefore, caution should be exercised when significant variations in  $\eta$  are observed between grains of the same mineral, and quantitative chemical analyses should be conducted in order to ensure the validity of any statement made regarding the correlation between  $\eta$  and chemical composition. This is particularly critical when material possess a tendency to exhibit grains in multiple crystallographic orientations (*i.e.*, twinning).

How common the OC effect is in minerals is unknown, but an appreciation of the relationship between crystal structure and BSE production is key. Certainly, any attempt to develop a more comprehensive understanding of BSE microscopy amongst geological materials must consider the role that the crystal structure plays.

## 2.6 CONCLUSIONS

Based on the information presented, it is concluded that in millerite from footwall Cu-Ni-PGE stringers at Coleman mine examined in this study:

(1) Most, if not all, grain exhibit a sharp lamellae which are interpreted as polysynthetic twins formed by reflection across  $\{01\bar{1}2\}$ , represented by Type I and Type II twins where the prior are earlier forming and dominant, with the latter forming subsequently. These twins show a striking contrast colour under PPL, alternatively go into extinction under XPL, and exhibit alternating grey-tones when viewed with BSEI.

(2) SEM-EDS analyses indicate that the twins are chemically homogeneous within the precision of the instrumentation. Thus, the variations in the patterns of backscattered electrons produced by millerite (grey-tone variations) do not arise from changes in mineral chemistry (minor-element substitutions or deviations from stoichiometry), are not attributed to any

appreciable chemical variations and their subsequent impact on  $Z_{\text{avg}}$  and thus  $\eta$ . Instead, they are the result of orientation contrast resulting from electron channelling.

(3) The twins are secondary in nature, possibly resulting from deformation ( $P_{\text{ext}}$ ) and/or an increase in internal pressure ( $P_{\text{int}}$ ) accompanying an increase in the unit-cell volume (1.78%) resulting from the  $\alpha \rightarrow \beta$  phase transition in NiS (*i.e.* crowningshieldite  $\rightarrow$  millerite) that occurs at 379°C.

## 2.7 REFERENCES

- BARBER, D.J., & WENK, H.R. (1979) Deformation twinning in calcite, dolomite and other rhombohedral carbonates. *Physics and Chemistry of Materials* **5**, 141-165.
- BARRY, J.C., & FORD, S. (2001) An electron microscopic study of nickel sulfide inclusions in toughened glass. *Journal of Material Science* **36**, 3721–3730.
- BURKHARD, M. (1993) Calcite twins, their geometry, appearance and significance as stress-strain markers and indicators of tectonic regime: a review. *Journal of Structural Geology* **15**, 351–368.
- DANA, E.S. (1949) *A Textbook of Mineralogy*. 4<sup>th</sup> Edition. Wiley, 851 pp.
- DAY, A., & TRIMBY, P. (2004) *Channel 5 Manual*. HKL Technology Inc., Hobro, Denmark.
- DEER, W.A., HOWIE, R.A., & ZUSSMAN, J. (1963) *Rock Forming Minerals Vol. V*. 1<sup>st</sup> Edition. Longmans, Green and Co. Ltd., 371 pp.
- GRICE, J.D., & FERGUSON, R.B. (1974) Crystal structure refinement of Millerite (beta -NiS). *Canadian Mineralogist* **12**, 248–252.
- JOY, D.C., NEWBURY, D.E., & DAVIDSON, D.I. (1982) Electron Channeling Patterns in the Scanning Electron-Microscope. *Journal of Applied Physics* **53**, 81–122.
- KULLERUD, G., & YUND, R.A. (1962) The Ni-S System and Related Minerals. *Journal of Petrology* **3**, 126–175.
- LLOYD, G.E. (1987) Atomic-Number and Crystallographic Contrast Images with the Sem - a Review of Backscattered Electron Techniques. *Mineralogical Magazine* **51**, 3–19.
- MOTOHASHI, Y., BRAILLON, P., & SERUGHETTI, J. (1976) Elastic energy stress-field of dislocations, and dislocation parameters in calcite crystals. *Physica Status Solidi a-Applied Research*, **37**, 263–270.
- NEUBERT, G., AND ROGASCHEWSKI, S. (1980) Backscattering Coefficient Measurements of 15 to 60 Kev Electrons for Solids at Various Angles of Incidence. *Physica Status Solidi a-Applied Research* **59**, 35–41.

- PALACHE, C., & WOOD, H.O. (1904) Crystallographic Study of Millerite. *American Journal of Science* **18**, 343–359.
- PRIOR, D.J., BOYLE, A.P., BRENKER, F., CHEADLE, M.C., DAY, A., LOPEZ, G., PERUZZO, L., POTTS, G.J., REDDY, S., SPIESS, R., & OTHERS (1999) The application of electron backscatter diffraction and orientation contrast imaging in the SEM to textural problems in rocks. *American Mineralogist* **84**, 1741–1759.
- RAMDOHR, P. (1969) *The Ore Minerals and Their Intergrowths*. 1<sup>st</sup> Edition, Elsevier, 1193 pp.
- REIMER, L. (1998) *Transmission Electron Microscopy: Physics of Image Formation and Microanalysis*. 2<sup>nd</sup> Edition. Springer, 532 pp.
- SMITH, E.M., NESTOLA, F., PASQUALETTO, L., ZORZI, F., SECCO, L., & WANG, W. (2018) Crowningshieldite, IMA 2018-072. CNMNC Newsletter No. 45, October 2018, page 1043. *European Journal of Mineralogy* **30**, 1037–1043.
- WANG, H.P., PRING, A., NGOTHAI, Y., & O'NEILL, B. (2006) The kinetics of the  $\alpha \rightarrow \beta$  transition in synthetic nickel monosulfide. *American Mineralogist* **91**, 171–181.
- ZAEFFERER, S., & ELHAMI, N.N. (2014) Theory and application of electron channelling contrast imaging under controlled diffraction conditions. *Acta Materialia* **75**, 20–50.

**APPENDIX A – MINERALOGY OF MAGMATIC SAMPLES**

**Table A1 – Macroscopic Mineralogy**

<b>Sample</b>	<b>Chalcopyrite</b>	<b>Millerite</b>	<b>Pyrrhotite</b>	<b>Pentlandite</b>	<b>Bornite</b>
NRS-001	X	X			X
NRS-002	X		X	X	
NRS-003	X		X		
NRS-004	X	X			
NRS-005	X	X			
NRS-006	X				
NRS-007	X				
NRS-008	X	X			
NRS-009	X	X			X
NRS-010	X	X			
NRS-011	X	X			
NRS-012	X	X			
NRS-013	X				
NRS-014	X				
NRS-015	X	X			
NRS-016	X				
NRS-017	X				
NRS-018	X	X			
NRS-019	X	X			
NRS-020	X				
NRS-021	X				
NRS-022	X		X		
NRS-023	X	X			
NRS-024	X		X	X	
NRS-025	X		X		
NRS-026	X		X	X	
NRS-027					X
NRS-028					X
NRS-029					X
NRS-030					X
NRS-031	X				X
NRS-032					X
NRS-033	X				X
NRS-034					X
NRS-035					X
NRS-036					X
NRS-037					X
NRS-038	X	X	X		X
NRS-039	X	X			
NRS-040	X	X			
NRS-041	X	X			X
NRS-042	X	X			
NRS-043	X	X			
NRS-044	X	X			
NRS-045	X	X			
NRS-046	X	X			
NRS-047	X		X	X	
NRS-048	X		X		
COL-001	X		X		
COL-002	X		X	X	
COL-003	X		X	X	
COL-004	X		X	X	

**Table A-1 (cont.)**

COL-005	X			X	
COL-006	X		X	X	
COL-007	X		X	X	
COL-008	X				
COL-009	X	X			
COL-010	X	X			
COL-011	X				
COL-012	X	X			
COL-013				X	
COL-014				X	
COL-015				X	
COL-016	X		X	X	
COL-017	X	X			
COL-018	X		X	X	
COL-019			X	X	
COL-020			X	X	
COL-021			X	X	
COL-022			X	X	
COL-023	X				
COL-024	X		X	X	
COL-025			X	X	
COL-026			X	X	
COL-027			X	X	
COL-028			X	X	
COL-029	X		X	X	
COL-030	X	X			X
COL-031	X	X			
COL-032	X	X			X
COL-033	X	X			
COL-034			X	X	
COL-035	X		x	X	
COL-036			X	X	
COL-037	X		X	X	
<b>Total</b>	63	29	31	29	17

\*All minerals were visually identified with the unaided eye, a hand lens, or indicated by magnetism.

\* All mineral assemblages also contain magnetite

**Table A2 – Microscopic Mineralogy**

Sample	Ccp	Mlr	Pn	Po	Bn	Cbn	Mag	Ilm <sup>1</sup>	Gn	Sp	Bhc	Haw	Ag	Au	Hes	Mch	Mon	Fro	Nig	Pa	Plv	Sbl	Sdb	Ktl	Ath	Ag-S
COL-004	X		X				X								X	X	X									
COL-007	X		X	X			X		X							X										
COL-008	X	X					X		X							X										
COL-015	X		X				X		X						X	X										
COL-016a	X		X	X			X		X						X											
COL-016b	X		X	X			X		X						X	X										
COL-017	X	X					X			X	X				X		X									
COL-020	X	X	X				X		X		X	X			X			X		X					X	
COL-021	X	X	X				X		X																	
COL-031a	X	X	X				X		X		X			X	X	X	X					X				
COL-031b	X	X	X				X		X					X	X	X	X									
COL-032	X	X			X		X		X						X											X
COL-033	X	X			X		X								X		X									
COL-034			X				X		X						X	X										
COL-035	X		X				X		X						X	X										
COL-036	X		X				X		X						X											
COL-037a	X		X				X		X																	
COL-037b	X		X				X		X						X	X										
NRS-002	X		X	X		X	X		X							X						X				
NRS-010	X	X					X								X	X	X									
NRS-015	X	X					X								X	X	X								X	
NRS-022	X		X	X		X	X		X						X	X	X	X	X	X						
NRS-023	X	X					X								X		X								X	
NRS-038a	X	X			X		X	X		X																
NRS-038b	X	X			X		X	X		X																
NRS-038c	X	X			X		X	X		X																
NRS-040	X	X			X		X		X																	
NRS-041	X	X			X		X		X				X		X									X		
NRS-042	X	X			X		X	X																		
NRS-045	X	X					X	X																		
<b>Total</b>	<b>29</b>	<b>18</b>	<b>16</b>	<b>5</b>	<b>8</b>	<b>2</b>	<b>30</b>	<b>5</b>	<b>19</b>	<b>4</b>	<b>3</b>	<b>1</b>	<b>1</b>	<b>2</b>	<b>19</b>	<b>14</b>	<b>9</b>	<b>2</b>	<b>1</b>	<b>1</b>	<b>1</b>	<b>1</b>	<b>1</b>	<b>2</b>	<b>1</b>	<b>1</b>

Bhc = bismutohauchecornite, Haw = hawleyite, Ag = silver, Au = gold, Hes = hessite, Mch = michenerite, Mon = moncheite, Fro = froodite, Nig = niggliite, Pa = parkerite, Plv = paolovite, Sbl = sobolevskite, Sdb = sudburyite, Ktl = kotulskite, Ath = acanthite.

<sup>1</sup>Ilmenite only occurs in association with host magnetite as an exsolved phase

\*All minerals were identified using either reflected-light microscopy and/or SEM-EDS

**APPENDIX B – CHEMISTRY OF MILLERITE**

**Table B1 – Chemistry of Magmatic Millerite**

Sample No.	Element (wt. %)				Total	<i>apfu</i> (S = 1)			
	Fe	Ni	Co	S		Fe	Ni	Co	Total
COL-017-01-1	0.21(6)	63.46(26)	0.71(6)	35.37(13)	99.75	0.003	0.980	0.011	0.995
COL-017-01-1	0.22	63.30	0.62	35.45	99.59	0.004	0.976	0.010	0.989
COL-017-01a-1	0.20	63.28	0.65	35.58	99.71	0.003	0.972	0.010	0.985
COL-017-02-2	0.26	63.68	0.64	35.72	100.30	0.004	0.974	0.010	0.988
COL-017-02-3	0.23	63.44	0.66	35.36	99.69	0.004	0.980	0.010	0.994
COL-017-02b-2	0.33	63.71	0.66	35.62	100.32	0.005	0.977	0.010	0.993
COL-017-03-2	0.21	63.30	0.73	35.35	99.59	0.003	0.978	0.011	0.993
COL-017-04-2	0.28	63.45	0.75	35.51	99.99	0.005	0.976	0.011	0.992
COL-017-05-2	0.25	63.36	0.67	35.51	99.79	0.004	0.975	0.010	0.989
COL-020-06-2	0.48	63.57	0.25	35.92	100.22	0.008	0.967	0.004	0.979
COL-020-12-2	0.40	63.45	0.13	35.71	99.69	0.006	0.971	0.002	0.979
COL-021-01-2	0.32	63.78	0.07	35.95	100.12	0.005	0.969	0.001	0.976
COL-021-01-3	0.38	63.52	0.14	35.90	99.94	0.006	0.967	0.002	0.975
COL-021-04-3	0.42	63.80	0.17	35.70	100.09	0.007	0.977	0.003	0.986
COL-021-06-3	0.41	63.93	0.20	35.91	100.45	0.007	0.973	0.003	0.982
COL-021-09-5	0.42	63.44	0.15	35.49	99.50	0.007	0.977	0.002	0.986
COL-021-09-6	0.39	63.58	0.26	35.45	99.68	0.006	0.980	0.004	0.990
COL-021-16-1	0.34	63.65	0.17	35.43	99.59	0.006	0.982	0.003	0.990
COL-031a-03-1	0.90	63.28	0.24	35.38	99.80	0.015	0.977	0.004	0.996
COL-031a-03-2	0.93	63.77	0.16	35.45	100.31	0.015	0.983	0.002	1.000
COL-031a-03-3	0.90	63.66	0.14	35.68	100.38	0.014	0.975	0.002	0.992
COL-031a-15-2	0.79	63.09	0.17	35.35	99.40	0.013	0.975	0.003	0.991
COL-031a-15-3	0.69	63.73	0.17	35.38	99.97	0.011	0.984	0.003	0.998
COL-031a-15-4	0.80	63.79	0.23	35.68	100.50	0.013	0.977	0.004	0.993
COL-031a-15-5	0.83	63.61	0.14	35.89	100.47	0.013	0.968	0.002	0.984
COL-031a-15-6	0.84	63.48	0.22	35.63	100.17	0.014	0.974	0.003	0.990
COL-031a-15-7	0.81	63.57	0.17	35.79	100.34	0.013	0.971	0.003	0.986
COL-031b-01-2	0.88	63.82	0.16	35.93	100.79	0.014	0.971	0.002	0.987
COL-031b-01-3	1.24	62.88	0.22	35.98	100.32	0.020	0.955	0.003	0.978
COL-031b-01-4	0.91	63.01	0.14	35.99	100.05	0.015	0.957	0.002	0.973
COL-031b-01-5	0.93	63.44	0.14	35.81	100.32	0.015	0.968	0.002	0.985
COL-031b-01-6	0.91	63.35	0.17	35.73	100.16	0.015	0.969	0.003	0.986
COL-031b-01-7	0.93	63.44	0.19	35.92	100.48	0.015	0.965	0.003	0.983
COL-031b-01-8	0.96	63.84	0.18	36.01	100.99	0.015	0.969	0.003	0.987
COL-031b-01-9	0.90	63.83	0.17	35.92	100.82	0.014	0.971	0.003	0.988
COL-031b-01b-1	0.92	63.57	0.15	35.67	100.31	0.015	0.974	0.002	0.991
COL-031b-01b-2	0.89	63.52	0.13	35.87	100.41	0.014	0.968	0.002	0.984
COL-031b-01b-3	0.97	63.66	0.25	35.73	100.61	0.016	0.974	0.004	0.993
COL-031b-01b-4	0.93	63.54	0.23	35.63	100.33	0.015	0.974	0.004	0.993
COL-031b-01b-5	0.97	63.40	0.21	35.72	100.30	0.016	0.970	0.003	0.989
COL-031b-01b-6	0.98	63.45	0.17	35.87	100.47	0.016	0.967	0.003	0.985
COL-031b-01b-8	0.98	63.85	0.12	35.74	100.69	0.016	0.976	0.002	0.994
COL-031b-02a-1	0.97	63.01	0.12	35.81	99.91	0.016	0.961	0.002	0.979
COL-031b-02a-2	0.94	63.56	0.10	35.98	100.58	0.015	0.965	0.002	0.982
COL-031b-02a-3	0.84	63.31	0.16	35.85	100.16	0.013	0.965	0.002	0.981
COL-031b-02a-4	0.94	63.53	0.09	35.84	100.40	0.015	0.969	0.001	0.985
COL-031b-02a-5	0.97	63.79	0.24	35.86	100.86	0.016	0.972	0.004	0.991
COL-031b-02a-6	0.99	63.57	0.15	35.87	100.58	0.016	0.968	0.002	0.987
COL-031b-02a-7	0.89	63.63	0.07	35.89	100.48	0.014	0.969	0.001	0.984
COL-031b-02a-8	0.95	63.37	0.18	35.94	100.44	0.015	0.963	0.003	0.981
COL-031b-05-1	0.83	63.78	0.12	35.76	100.49	0.013	0.975	0.002	0.990

**Table B1 (cont.)**

COL-031b-05-2	0.91	63.98	0.19	35.94	101.02	0.015	0.973	0.003	0.990
COL-031b-05-3	0.90	63.55	0.14	36.16	100.75	0.014	0.960	0.002	0.977
COL-031b-05-4	0.90	63.62	0.21	35.99	100.72	0.014	0.966	0.003	0.983
COL-031b-05-5	0.96	63.59	0.15	36.02	100.72	0.015	0.965	0.002	0.982
COL-031b-05-6	0.86	63.72	0.08	35.79	100.45	0.014	0.973	0.001	0.988
COL-031b-05-7	0.83	63.59	0.22	35.99	100.63	0.013	0.965	0.003	0.982
COL-031b-09-1	0.86	63.98	0.13	35.85	100.82	0.014	0.975	0.002	0.991
COL-031b-09-2	0.89	63.99	0.20	35.94	101.02	0.014	0.973	0.003	0.990
COL-031b-09-3	0.77	63.85	0.18	35.78	100.58	0.012	0.975	0.003	0.990
COL-031b-09-4	0.90	63.78	0.15	35.69	100.52	0.014	0.977	0.002	0.993
COL-031b-09-5	1.08	63.85	0.19	36.01	101.13	0.017	0.969	0.003	0.989
COL-031b-09-7	1.10	63.84	0.20	35.58	100.72	0.018	0.980	0.003	1.001
COL-031b-09-8	0.91	63.79	0.14	35.92	100.76	0.015	0.970	0.002	0.987
COL-031b-09-9	0.81	63.71	0.07	35.88	100.47	0.013	0.970	0.001	0.984
COL-031b-12-1	0.90	63.80	0.22	35.91	100.83	0.014	0.971	0.003	0.989
COL-031b-12-2	0.95	63.41	0.15	35.78	100.29	0.015	0.968	0.002	0.986
COL-031b-12-3	0.90	63.71	0.19	35.73	100.53	0.014	0.974	0.003	0.992
COL-031b-12-4	0.92	63.88	0.08	35.58	100.46	0.015	0.981	0.001	0.997
COL-031b-12-5	0.90	63.70	0.12	35.86	100.58	0.014	0.971	0.002	0.987
COL-031b-18-2	0.94	63.32	0.12	35.56	99.94	0.015	0.973	0.002	0.990
COL-031b-18-3	0.99	63.01	0.10	35.59	99.69	0.016	0.967	0.002	0.985
COL-031b-18-4	0.98	63.00	0.11	35.66	99.75	0.016	0.965	0.002	0.983
COL-031b-18-5	1.03	63.30	0.15	35.63	100.11	0.017	0.971	0.002	0.990
COL-031b-18-6	1.06	63.24	0.20	35.68	100.18	0.017	0.969	0.003	0.989
COL-031b-18-7	1.19	63.54	0.15	35.53	100.41	0.019	0.977	0.002	0.999
COL-032-06a-1	0.17	64.19	0.05	35.48	99.89	0.003	0.989	0.001	0.992
COL-032-06a-2	0.16	63.94	0.02	35.46	99.58	0.003	0.985	0.000	0.988
COL-032-06a-3	0.14	63.86	0.01	35.54	99.55	0.002	0.982	0.000	0.984
COL-032-06a-4	0.19	63.93	0.05	35.33	99.50	0.003	0.989	0.001	0.993
COL-032-06a-5	0.19	63.86	0.01	35.54	99.60	0.003	0.982	0.000	0.985
COL-032-06a-6	0.20	63.85	0.05	35.72	99.82	0.003	0.977	0.001	0.981
COL-032-11-1	0.17	63.86	0.11	35.45	99.59	0.003	0.984	0.002	0.989
COL-032-11-2	0.13	63.84	0.03	35.36	99.36	0.002	0.987	0.000	0.989
COL-032-11-3	0.17	63.89	0.10	35.49	99.65	0.003	0.984	0.002	0.988
COL-032-11-4	0.18	63.76	0.00	35.82	99.76	0.003	0.973	0.000	0.976
COL-032-14-1	0.27	64.22	0.08	35.37	99.94	0.004	0.992	0.001	0.998
COL-032-14-2	0.18	63.73	0.07	35.49	99.47	0.003	0.981	0.001	0.985
COL-032-14-3	0.23	64.01	0.05	35.67	99.96	0.004	0.981	0.001	0.985
COL-032-14-4	0.23	64.44	0.02	35.53	100.22	0.004	0.991	0.000	0.995
COL-032-16-2	0.18	64.55	0.04	35.67	100.44	0.003	0.989	0.001	0.992
COL-032-16-3	0.24	64.30	0.02	35.78	100.34	0.004	0.982	0.000	0.986
COL-032-16-4	0.17	64.21	0.10	35.61	100.09	0.003	0.985	0.002	0.990
COL-032-16-5	0.21	63.65	0.03	35.79	99.68	0.003	0.972	0.000	0.976
COL-033-01-3	0.13	63.71	0.34	35.89	100.07	0.002	0.970	0.005	0.977
COL-033-01-4	0.09	63.30	0.33	35.84	99.56	0.001	0.965	0.005	0.972
COL-033-01-5	0.14	63.50	0.37	35.90	99.91	0.002	0.967	0.006	0.974
COL-033-01-6	0.11	63.43	0.46	36.09	100.09	0.002	0.960	0.007	0.969
COL-033-02-2	0.19	63.73	0.47	35.76	100.15	0.003	0.974	0.007	0.984
COL-033-02-3	0.16	63.87	0.40	35.77	100.20	0.003	0.976	0.006	0.984
COL-033-02-4	0.13	63.50	0.52	35.80	99.95	0.002	0.969	0.008	0.979
COL-033-02-5	0.05	63.30	0.48	35.83	99.66	0.001	0.965	0.007	0.973
COL-033-03-3	0.09	63.18	0.48	35.69	99.44	0.001	0.967	0.007	0.976
COL-033-03-4	0.07	63.31	0.48	35.86	99.72	0.001	0.965	0.007	0.973
COL-033-03-5	0.10	63.77	0.51	35.74	100.12	0.002	0.975	0.008	0.984
COL-033-03-6	0.02	63.84	0.52	35.85	100.23	0.000	0.973	0.008	0.981
COL-033-05-4	0.12	63.62	0.57	35.91	100.22	0.002	0.968	0.009	0.979
COL-033-05-5	0.12	63.39	0.50	35.88	99.89	0.002	0.965	0.008	0.975
COL-033-05-6	0.15	63.61	0.56	35.89	100.21	0.002	0.968	0.008	0.979
COL-033-05-7	0.11	63.87	0.53	35.77	100.28	0.002	0.976	0.008	0.986
COL-033-05-8	0.08	63.20	0.60	35.72	99.60	0.001	0.967	0.009	0.977
COL-033-05-9	0.09	63.89	0.55	35.70	100.23	0.001	0.978	0.008	0.988
COL-033-06b-1	0.08	63.28	0.55	35.54	99.45	0.001	0.973	0.008	0.983

**Table B1 (cont.)**

COL-033-06b-2	0.18	63.38	0.49	35.72	99.77	0.003	0.970	0.007	0.980
COL-033-06b-3	0.09	63.42	0.51	35.64	99.66	0.001	0.972	0.008	0.982
COL-033-06b-5	0.11	63.33	0.33	35.78	99.55	0.002	0.967	0.005	0.974
COL-033-06b-6	0.13	63.07	0.50	35.58	99.28	0.002	0.969	0.008	0.978
COL-033-10-1	0.09	63.47	0.44	35.67	99.67	0.001	0.972	0.007	0.980
COL-033-10-2	0.11	63.83	0.55	35.65	100.14	0.002	0.978	0.008	0.989
COL-033-11a-1	0.23	63.43	0.51	35.71	99.88	0.004	0.971	0.008	0.982
COL-033-11a-2	0.10	63.75	0.53	35.80	100.18	0.002	0.973	0.008	0.983
COL-033-11a-3	0.14	63.79	0.57	35.67	100.17	0.002	0.977	0.009	0.988
COL-033-11a-4	0.08	64.05	0.43	35.92	100.48	0.001	0.974	0.007	0.982
COL-033-11a-5	0.12	63.72	0.54	35.85	100.23	0.002	0.971	0.008	0.981
COL-033-11b-1	0.05	64.00	0.52	35.66	100.23	0.001	0.981	0.008	0.989
COL-033-11b-2	0.08	63.95	0.48	35.83	100.34	0.001	0.975	0.007	0.984
COL-033-11b-3	0.08	63.48	0.48	35.77	99.81	0.001	0.970	0.007	0.978
COL-033-11b-4	0.09	63.86	0.50	35.73	100.18	0.001	0.977	0.008	0.986
COL-033-11b-5	0.09	63.97	0.53	35.77	100.36	0.001	0.977	0.008	0.987
COL-033-11b-6	0.17	63.58	0.47	35.82	100.04	0.003	0.970	0.007	0.980
NRS-015-01-1	0.25	63.38	0.25	35.65	99.53	0.004	0.971	0.004	0.979
NRS-015-01-4	0.25	63.75	0.21	35.93	100.14	0.004	0.970	0.003	0.977
NRS-015-04-1	0.26	64.08	0.21	35.94	100.49	0.004	0.974	0.003	0.982
NRS-015-04-2	0.28	63.76	0.27	35.62	99.93	0.005	0.978	0.004	0.987
NRS-015-04-3	0.30	63.80	0.22	35.70	100.02	0.005	0.977	0.003	0.985
NRS-015-05-3	0.41	63.35	0.20	35.78	99.74	0.007	0.967	0.003	0.977
NRS-015-05a-1	0.36	63.43	0.19	35.68	99.66	0.006	0.971	0.003	0.980
NRS-015-05a-2	0.30	63.22	0.21	35.68	99.41	0.005	0.968	0.003	0.976
NRS-015-05a-4	0.24	63.30	0.18	35.50	99.22	0.004	0.974	0.003	0.981
NRS-015-06-1	0.30	64.00	0.22	35.83	100.35	0.005	0.976	0.003	0.984
NRS-015-06-2	0.31	63.57	0.26	35.13	99.27	0.005	0.989	0.004	0.998
NRS-015-06-3	0.26	63.44	0.22	35.50	99.42	0.004	0.976	0.003	0.984
NRS-015-06a-1	0.31	63.60	0.18	35.42	99.51	0.005	0.981	0.003	0.989
NRS-015-06a-2	0.30	63.38	0.26	35.50	99.44	0.005	0.976	0.004	0.984
NRS-015-06a-3	0.35	63.32	0.23	35.54	99.44	0.006	0.974	0.004	0.983
NRS-015-07-2	0.33	63.48	0.26	35.55	99.62	0.005	0.976	0.004	0.985
NRS-015-07-3	0.29	63.53	0.20	35.68	99.70	0.005	0.973	0.003	0.981
NRS-015-08-1	0.34	63.84	0.22	35.69	100.09	0.005	0.977	0.003	0.986
NRS-015-09-2	0.32	63.77	0.26	35.65	100.00	0.005	0.977	0.004	0.987
NRS-015-10-2	0.32	63.10	0.19	35.76	99.37	0.005	0.964	0.003	0.972
NRS-015-10-3	0.26	63.63	0.24	35.74	99.87	0.004	0.973	0.004	0.981
NRS-015-12-4	0.29	63.42	0.26	35.72	99.69	0.005	0.970	0.004	0.979
NRS-023-01-1	0.12	64.08	0.24	35.61	100.05	0.002	0.983	0.004	0.989
NRS-023-02-1	0.11	63.94	0.30	35.45	99.80	0.002	0.986	0.005	0.992
NRS-023-02-3	0.28	64.30	0.26	35.67	100.51	0.005	0.985	0.004	0.993
NRS-023-04-3	0.17	63.66	0.26	35.55	99.64	0.003	0.979	0.004	0.985
NRS-023-05-1	0.12	63.51	0.23	35.54	99.40	0.002	0.976	0.004	0.982
NRS-023-05-2	0.14	63.49	0.27	35.24	99.14	0.002	0.984	0.004	0.991
NRS-023-06-1	0.11	64.02	0.27	35.40	99.80	0.002	0.988	0.004	0.994
NRS-023-06-2	0.13	63.73	0.37	35.32	99.55	0.002	0.986	0.006	0.994
NRS-023-07-1	0.15	64.06	0.32	35.51	100.04	0.002	0.986	0.005	0.993
NRS-023-07-2	0.23	64.01	0.32	35.76	100.32	0.004	0.978	0.005	0.987
NRS-023-08-2	0.12	63.70	0.30	35.41	99.53	0.002	0.983	0.005	0.990
NRS-040-01-4	0.17	63.10	0.49	35.55	99.31	0.003	0.970	0.008	0.980
NRS-040-01-5	0.20	63.03	0.56	35.49	99.28	0.003	0.970	0.009	0.982
NRS-040-01-6	0.16	63.43	0.52	35.78	99.89	0.003	0.969	0.008	0.979
NRS-040-01-7	0.23	63.62	0.58	35.90	100.33	0.004	0.968	0.009	0.981
NRS-040-02-6	0.13	63.26	0.64	36.00	100.03	0.002	0.960	0.010	0.972
NRS-040-03-1	0.16	63.36	0.64	35.95	100.11	0.003	0.963	0.010	0.975
NRS-040-03-2	0.13	63.13	0.57	35.71	99.54	0.002	0.966	0.009	0.977
NRS-040-05-2	0.10	63.47	0.49	36.00	100.06	0.002	0.963	0.007	0.972
NRS-040-07-1	0.14	63.03	0.56	35.56	99.29	0.002	0.969	0.009	0.979
NRS-040-07-2	0.13	63.01	0.62	35.64	99.40	0.002	0.966	0.009	0.978

**Table B1 (cont.)**

<b>NRS-041-01-1</b>	0.22	64.07	0.50	35.59	100.38	0.004	0.984	0.008	0.995
<b>NRS-041-01-3</b>	0.14	63.91	0.59	35.80	100.44	0.002	0.975	0.009	0.987
<b>NRS-041-01-4</b>	0.23	63.57	0.50	35.79	100.09	0.004	0.971	0.008	0.982
<b>NRS-041-05-3</b>	0.12	63.70	0.63	35.75	100.20	0.002	0.974	0.010	0.985
<b>Average</b>	0.44	63.62	0.29	35.71	100.05	0.007	0.974	0.004	0.985
<b>Minimum</b>	0.02	62.88	0.00	35.13	99.14	0.000	0.955	0.000	0.969
<b>Maximum</b>	1.24	64.55	0.75	36.16	101.13	0.020	0.992	0.011	1.001
<b><math>\sigma</math></b>	0.353	0.302	0.191	0.188	0.437	0.006	0.007	0.003	0.006
<b>Range</b>	1.22	1.67	0.75	1.03	1.99	0.019	0.037	0.011	0.032

Errors indicated by parentheses

\*All spectra obtained using the methods outlined in section 1.2

**Table B2 – Chemistry of Hydrothermal Millerite**

Sample	Element (wt. %)					<i>apfu</i> (S = 1)			
	Fe	Ni	Co	S	Total	Fe	Ni	Co	Total
CMN-001-01-1	1.62(6)	61.63(26)	0.17(6)	36.43(13)	99.85	0.026	0.924	0.003	0.952
CMN-001-01-2	1.63	61.94	0.19	36.31	100.07	0.026	0.932	0.003	0.961
CMN-001-01-3	1.35	62.37	0.17	36.21	100.10	0.021	0.941	0.003	0.965
CMN-001-01-4	1.75	61.19	0.17	36.18	99.29	0.028	0.924	0.003	0.954
CMN-001-01-5	1.61	61.47	0.19	36.14	99.41	0.026	0.929	0.003	0.958
CMN-001-02-1	0.81	62.95	0.00	36.31	100.07	0.013	0.947	0.000	0.960
CMN-001-02-2	0.93	62.61	0.00	36.47	100.01	0.015	0.938	0.000	0.953
CMN-001-02-4	1.05	61.83	0.13	36.16	99.17	0.017	0.934	0.002	0.953
CMN-001-03-s1	0.92	61.99	0.31	36.02	99.24	0.015	0.940	0.005	0.960
CMN-001-03-1	0.76	62.68	0.28	35.97	99.69	0.012	0.952	0.004	0.969
CMN-001-03-2	0.92	62.66	0.35	36.38	100.31	0.015	0.941	0.005	0.961
CMN-001-03-3	0.76	62.57	0.32	35.96	99.61	0.012	0.951	0.005	0.968
CMN-001-06-2	1.36	62.17	0.16	36.65	100.34	0.021	0.927	0.002	0.951
CMN-001-06-3	0.60	62.67	0.22	36.70	100.19	0.009	0.933	0.003	0.946
CMN-001-06-4	0.50	63.34	0.16	36.47	100.47	0.008	0.949	0.002	0.959
CMN-001-06-5	0.75	63.01	0.22	36.48	100.46	0.012	0.944	0.003	0.959
CMN-001-07-1	0.97	63.05	0.20	36.32	100.54	0.015	0.949	0.003	0.967
CMN-001-07-2	0.98	62.51	0.14	36.24	99.87	0.016	0.943	0.002	0.960
CMN-001-07-3	0.90	62.26	0.14	36.44	99.74	0.014	0.934	0.002	0.950
CMN-001-07-4	0.81	62.37	0.18	36.36	99.72	0.013	0.937	0.003	0.953
CMN-001-07-5	0.90	62.44	0.00	36.30	99.64	0.014	0.940	0.000	0.954
CMN-001-08-1	0.60	63.21	0.00	36.38	100.19	0.009	0.949	0.000	0.959
CMN-001-08-2	0.49	63.39	0.20	36.17	100.25	0.008	0.958	0.003	0.968
CMN-001-08-3	0.59	63.28	0.00	36.27	100.14	0.009	0.953	0.000	0.963
CMN-001-08-4	0.66	62.91	0.00	36.31	99.88	0.010	0.947	0.000	0.957
CMN-001-08-5	0.70	63.03	0.00	36.11	99.84	0.011	0.954	0.000	0.965
CMN-001-09-1	1.84	61.91	0.00	36.39	100.14	0.029	0.930	0.000	0.959
CMN-001-09-2	2.30	61.25	0.00	36.17	99.72	0.037	0.925	0.000	0.962
CMN-001-09-3	2.44	61.01	0.17	36.23	99.85	0.039	0.920	0.003	0.961
CMN-001-09-4	2.61	60.92	0.15	36.27	99.95	0.041	0.918	0.002	0.961
CMN-001-09-5	2.65	61.06	0.00	36.19	99.90	0.042	0.922	0.000	0.964
CMN-001-10-1	0.99	62.34	0.00	35.98	99.31	0.016	0.947	0.000	0.963
CMN-001-10-2	1.60	62.09	0.15	36.30	100.14	0.025	0.935	0.002	0.962
CMN-001-10-3	1.75	61.90	0.00	36.28	99.93	0.028	0.932	0.000	0.960
CMN-001-10-4	0.87	62.93	0.00	36.38	100.18	0.014	0.945	0.000	0.959
CMN-001-10-5	1.10	62.37	0.15	36.19	99.81	0.017	0.942	0.002	0.961
CMN-002-01-1	0.39	61.85	1.61	36.35	100.20	0.006	0.930	0.024	0.960
CMN-002-01-2	0.20	61.11	2.23	36.18	99.72	0.003	0.923	0.034	0.960
CMN-002-01-3	0.19	61.76	1.63	35.96	99.54	0.003	0.938	0.025	0.966
CMN-002-01-4	0.23	61.58	1.79	36.35	99.95	0.004	0.926	0.027	0.956
CMN-002-02-1	0.17	60.20	2.92	36.07	99.36	0.003	0.912	0.044	0.959
CMN-002-02-2	0.30	59.70	3.57	36.16	99.73	0.005	0.902	0.054	0.961
CMN-002-02-3	0.29	60.02	2.67	36.10	99.08	0.005	0.908	0.040	0.953
CMN-002-02-4	0.15	61.86	1.05	36.20	99.26	0.002	0.934	0.016	0.952
CMN-002-02-5	0.22	61.70	0.73	35.87	98.52	0.004	0.940	0.011	0.955
CMN-002-03-1	1.06	61.37	1.42	36.08	99.93	0.017	0.929	0.021	0.968
CMN-002-03-2	0.67	61.24	1.81	35.90	99.62	0.011	0.932	0.027	0.970
CMN-002-03-3	0.42	61.54	1.75	36.09	99.80	0.007	0.932	0.026	0.965
CMN-002-03-5	1.87	59.78	1.45	36.21	99.31	0.030	0.902	0.022	0.954
CMN-002-04-1	0.32	62.51	0.83	36.30	99.96	0.005	0.941	0.012	0.958
CMN-002-04-5	0.33	62.07	1.01	36.17	99.58	0.005	0.938	0.015	0.958
CMN-002-05-1	0.24	61.36	1.53	36.31	99.44	0.004	0.923	0.023	0.950
CMN-002-05-2	0.19	61.88	1.56	36.12	99.75	0.003	0.936	0.024	0.963
CMN-002-05-3	0.13	61.60	1.74	36.40	99.87	0.002	0.925	0.026	0.953
CMN-002-05-4	0.20	60.62	2.78	36.13	99.73	0.003	0.917	0.042	0.962
CMN-002-05-5	0.64	60.59	1.60	36.22	99.05	0.010	0.914	0.024	0.948
CMN-002-06-1	0.16	60.24	2.85	36.57	99.82	0.003	0.900	0.042	0.945
CMN-002-06-2	0.33	61.84	1.56	36.47	100.20	0.005	0.927	0.023	0.955
CMN-002-06-3	0.51	61.30	1.83	36.26	99.90	0.008	0.924	0.027	0.959
CMN-002-06-4	0.19	61.02	2.62	36.26	100.09	0.003	0.920	0.039	0.962
CMN-002-06-5	0.28	60.88	2.26	35.73	99.15	0.004	0.931	0.034	0.970

**Table B2 (cont.)**

CMN-002-07-1	0.34	62.67	0.87	36.04	99.92	0.005	0.950	0.013	0.969
CMN-002-07-2	0.38	62.20	0.81	35.83	99.22	0.006	0.949	0.012	0.967
CMN-002-07-4	0.28	62.23	0.81	36.16	99.48	0.004	0.940	0.012	0.957
CMN-002-07-5	0.24	62.11	0.83	35.83	99.01	0.004	0.947	0.013	0.964
CMN-003-01-2	0.16	62.12	1.19	36.73	100.20	0.003	0.924	0.018	0.944
CMN-003-01-3	0.25	62.14	1.28	36.25	99.92	0.004	0.937	0.019	0.960
CMN-003-01-4	0.09	62.05	1.26	36.45	99.85	0.001	0.930	0.019	0.950
CMN-003-02-1	0.15	62.65	0.79	36.11	99.70	0.002	0.948	0.012	0.962
CMN-003-02-2	0.15	62.41	0.74	35.70	99.00	0.002	0.955	0.011	0.969
CMN-003-03-1	1.36	60.39	2.35	35.87	99.97	0.022	0.920	0.036	0.977
CMN-003-03-2	0.34	61.98	1.31	35.81	99.44	0.005	0.946	0.020	0.971
CMN-003-03-3	0.76	61.22	1.52	35.73	99.23	0.012	0.936	0.023	0.972
CMN-003-03-4	0.89	60.63	2.10	35.84	99.46	0.014	0.924	0.032	0.971
CMN-003-03-5	1.09	60.48	1.79	35.74	99.10	0.018	0.925	0.027	0.969
CMN-003-04-1	0.16	62.45	1.15	35.94	99.70	0.003	0.949	0.017	0.969
CMN-003-04-2	0.17	62.48	1.10	35.96	99.71	0.003	0.949	0.017	0.969
CMN-003-04-3	0.18	62.26	1.25	35.85	99.54	0.003	0.949	0.019	0.971
CMN-003-05-2	0.23	62.62	0.87	35.70	99.42	0.004	0.958	0.013	0.975
CMN-003-05-3	0.28	62.43	1.08	35.82	99.61	0.004	0.952	0.016	0.973
CMN-003-05-4	0.51	62.04	1.20	35.91	99.66	0.008	0.944	0.018	0.970
CMN-004-01a-1	0.42	61.79	1.37	35.47	99.05	0.007	0.952	0.021	0.980
CMN-004-01a-3	0.43	61.77	1.29	35.56	99.05	0.007	0.949	0.020	0.976
CMN-004-01a-4	0.43	62.03	1.33	34.99	98.78	0.007	0.969	0.021	0.996
CMN-004-01a-5	0.43	62.03	1.33	34.99	98.78	0.007	0.969	0.021	0.996
CMN-004-01b-1	0.42	62.45	1.24	35.82	99.93	0.007	0.953	0.019	0.978
CMN-004-01b-3	0.40	61.44	1.39	35.58	98.81	0.006	0.944	0.021	0.971
CMN-004-01b-5	0.33	61.73	1.25	35.47	98.78	0.005	0.951	0.019	0.975
CMN-005-01-1	1.48	62.09	0.42	35.77	99.76	0.024	0.949	0.006	0.979
CMN-005-01-2	1.66	61.48	0.66	35.97	99.77	0.026	0.934	0.010	0.970
CMN-005-01-3	1.54	62.01	0.37	36.17	100.09	0.024	0.937	0.006	0.967
CMN-005-01-5	1.70	61.72	0.57	35.68	99.67	0.027	0.945	0.009	0.981
CMN-005-02-1	1.75	61.75	0.61	36.02	100.13	0.028	0.937	0.009	0.974
CMN-005-02-2	1.78	61.52	0.51	35.93	99.74	0.028	0.936	0.008	0.972
CMN-005-02-5	1.86	61.73	0.50	36.13	100.22	0.030	0.934	0.008	0.971
CMN-005-03-1	1.63	61.58	0.49	35.90	99.60	0.026	0.937	0.007	0.971
CMN-005-03-2	1.58	61.83	0.60	35.43	99.44	0.026	0.954	0.009	0.988
CMN-005-03-3	1.45	62.14	0.43	35.78	99.80	0.023	0.949	0.007	0.979
CMN-005-03-5	1.41	62.14	0.34	35.83	99.72	0.023	0.948	0.005	0.975
CMN-005-04-1	1.96	61.43	0.34	35.68	99.41	0.032	0.941	0.005	0.978
CMN-005-04-3	1.18	62.43	0.46	35.70	99.77	0.019	0.956	0.007	0.982
CMN-005-04-5	1.33	61.67	0.42	35.36	98.78	0.022	0.953	0.006	0.981
CMN-005-05-1	1.15	62.31	0.31	35.95	99.72	0.018	0.947	0.005	0.970
CMN-005-05-2	1.16	61.65	0.29	35.67	98.77	0.019	0.944	0.004	0.968
CMN-005-05-3	1.20	62.34	0.30	35.75	99.59	0.019	0.953	0.005	0.977
CMN-005-05-4	1.25	61.75	0.24	35.71	98.95	0.020	0.945	0.004	0.969
CMN-005-06-s8	1.68	61.65	0.66	35.97	99.96	0.027	0.937	0.010	0.973
CMN-005-06-5	1.62	61.96	0.55	36.07	100.20	0.026	0.939	0.008	0.973
CMN-006-01-s1	0.71	60.71	2.83	35.85	100.10	0.011	0.925	0.043	0.980
CMN-006-01-1	0.70	60.52	2.82	35.64	99.68	0.011	0.928	0.043	0.982
CMN-006-01-2	0.79	60.30	2.82	35.61	99.52	0.013	0.925	0.043	0.981
CMN-006-01-3	0.74	60.22	2.91	35.85	99.72	0.012	0.918	0.044	0.974
CMN-006-01-4	0.83	60.74	2.74	35.99	100.30	0.013	0.922	0.041	0.977
CMN-006-02-1	0.85	59.76	2.64	35.67	98.92	0.014	0.915	0.040	0.969
CMN-006-02-3	0.78	60.76	2.83	35.72	100.09	0.013	0.929	0.043	0.985
CMN-006-02-8	0.75	60.88	2.63	35.64	99.90	0.012	0.933	0.040	0.986
CMN-006-02-9	0.73	60.91	2.76	35.83	100.23	0.012	0.929	0.042	0.983
CMN-006-03-1	0.70	59.69	2.82	35.66	98.87	0.011	0.915	0.043	0.969
CMN-006-03-3	0.71	60.53	2.91	35.81	99.96	0.011	0.924	0.044	0.979
CMN-006-04-1	0.67	60.27	2.88	35.89	99.71	0.011	0.918	0.044	0.972
CMN-006-04-2	0.69	60.45	2.94	35.99	100.07	0.011	0.918	0.044	0.973

**Table B2 (cont.)**

<b>CMN-006-04-3</b>	0.75	60.78	2.89	35.71	100.13	0.012	0.930	0.044	0.986
<b>CMN-006-04-4</b>	0.73	60.55	2.90	35.58	99.76	0.012	0.930	0.044	0.986
<b>CMN-006-05-1</b>	0.78	60.88	2.85	35.98	100.49	0.012	0.925	0.043	0.980
<b>CMN-006-05-3</b>	0.70	60.63	2.86	35.70	99.89	0.011	0.928	0.044	0.983
<b>CMN-006-06-1</b>	0.71	60.56	2.86	35.47	99.60	0.011	0.933	0.044	0.988
<b>CMN-006-06-3</b>	0.72	60.03	2.87	35.37	98.99	0.012	0.927	0.044	0.983
<b>CMN-006-06-4</b>	0.71	60.69	2.75	35.47	99.62	0.011	0.935	0.042	0.989
<b>CMN-006-06-5</b>	0.64	60.31	2.93	35.47	99.35	0.010	0.929	0.045	0.984
<b>CMN-006-06-6</b>	0.74	60.42	2.77	35.00	98.93	0.012	0.943	0.043	0.999
<b>CMN-006-08-s7</b>	0.70	60.11	3.14	35.72	99.67	0.011	0.920	0.048	0.979
<b>CMN-006-08-1</b>	0.71	59.81	3.26	35.68	99.46	0.011	0.916	0.050	0.977
<b>CMN-006-08-2</b>	0.68	60.07	3.25	35.81	99.81	0.011	0.917	0.049	0.977
<b>CMN-006-08-3</b>	0.75	59.95	3.27	35.78	99.75	0.012	0.916	0.050	0.977
<b>CMN-006-08-4</b>	0.73	60.01	3.21	35.75	99.70	0.012	0.917	0.049	0.978
<b>CMN-006-09-1</b>	0.70	59.94	3.13	35.43	99.20	0.011	0.924	0.048	0.984
<b>CMN-006-09-2</b>	0.75	59.72	3.24	35.40	99.11	0.012	0.922	0.050	0.984
<b>CMN-006-09-3</b>	0.65	60.00	3.25	35.73	99.63	0.010	0.918	0.050	0.978
<b>CMN-006-09-4</b>	0.75	59.71	3.26	35.49	99.21	0.012	0.919	0.050	0.981
<b>CMN-006-10-2</b>	0.63	59.93	3.08	35.33	98.97	0.010	0.927	0.047	0.985
<b>CMN-006-10-3</b>	0.69	59.69	3.08	35.57	99.03	0.011	0.917	0.047	0.975
<b>CMN-006-10-5</b>	0.76	59.43	3.18	35.56	98.93	0.012	0.913	0.049	0.974
<b>Average</b>	0.84	61.49	1.37	35.96	99.66	0.013	0.934	0.021	0.969
<b>Minimum</b>	0.09	59.43	0.00	34.99	98.52	0.001	0.900	0.000	0.944
<b>Maximum</b>	2.65	63.39	3.57	36.73	100.54	0.042	0.969	0.054	0.999
<b><math>\sigma</math></b>	0.558	0.974	1.134	0.343	0.436	0.009	0.014	0.017	0.011
<b>Range</b>	2.56	3.96	3.57	1.74	2.02	0.041	0.069	0.054	0.054

Errors indicated by parentheses

\*All spectra obtained using the methods outlined in section 1.2

## APPENDIX C – TEMPERATURE GRADIENTS FOR FURNACES

**Table C1 – Temperature Gradients for Chico**

d (cm)	1000 °C	900 °C	800 °C	700 °C	600 °C	500 °C	400 °C	300 °C
0	1000	900	800	700	600	500	400	300
1	1000	900	800	701	602	503	402	302
2	997	902	801	703	605	506	404	305
3	998	906	807	706	608	508	407	306
4	1003	906	808	707	607	509	407	305
5	1006	903	806	705	606	507	405	302
6	1003	899	803	702	602	502	401	297
7	1000	894	798	697	596	497	396	292
8	995	887	793	691	591	491	390	288
9	989	880	787	685	584	484	382	282
10	984	872	780	675	575	476	376	276
11	977	864	771	668	566	467	368	270
12	969	853	760	657	555	458	361	263
13	960	841	749	645	543	447	352	260
14	946	830	736	633	531	436	344	254
15	928	826	720	618	517	425	335	248
16	911	810	708	604	505	414	327	242
17	898	795	694	590	492	398	310	234

\*Temperature readings were obtained using a thermocouple placed in the furnace at the desired distance. The thermocouple was allowed five minutes to adjust to the temperature for each reading.

**Table C2 – Temperature Gradients for Gummo**

d (cm)	1000 °C	900 °C	800 °C	700 °C	600 °C	500 °C	400 °C	300 °C
0	1000	898	800	700	600	500	400	300
1	1000	899	801	700	602	503	402	300
2	1001	901	802	701	605	504	404	299
3	1006	906	807	704	608	507	406	299
4	1011	908	812	708	611	509	407	299
5	1013	912	813	709	611	508	405	299
6	1013	912	812	708	609	506	402	298
7	1011	910	809	705	605	501	398	295
8	1007	906	805	701	600	497	393	290
9	1001	900	799	695	593	490	388	285
10	995	894	793	688	585	482	380	279
11	988	887	784	679	576	473	372	273
12	978	875	774	668	564	464	363	268
13	967	862	763	656	553	453	356	262
14	953	849	748	643	540	440	346	256
15	937	834	733	625	525	429	337	248
16	919	816	718	613	510	418	327	244
17	902	799	700	596	497	405	314	230

\*Temperature readings were obtained using a thermocouple placed in the furnace at the desired distance. The thermocouple was allowed five minutes to adjust to the temperature for each reading.

## APPENDIX D – CATALOGUE OF ALL MILLERITE & NiS SPECIMENS

### Samples from Canadian Museum of Nature

**CMN-001:** Dumbarton Mine, Bird River, Manitoba, Canada

- CMNMC 31969 (Millerite)
- Individual grains in capsule
- 1<sup>st</sup> row of “Puck 1” 10 grains

**CMN-002:** Halls Gap, Kentucky, USA

- CMNMC 31972 (Millerite)
- Individual grains in capsule
- 2<sup>nd</sup> row of “Puck 1” 7 grains

**CMN-003:** Gap Mine, Pennsylvania, USA

- CMNMC 31977 (Millerite)
- Individual Grains in capsule
- 1<sup>st</sup> row of “Puck 2” 5 grains

**CMN-004:** Orford Nickel Mine, Québec, Canada

- CMNMC 31980 (Millerite)
- Individual grains in capsule
- 2<sup>nd</sup> row of “Puck 2” 2 grains

**CMN-005:** Sterling Mine, New York, USA

- CMNMC 31982 (Millerite)
- Individual grains in capsule
- 1<sup>st</sup> row of “Puck 3” 6 grains

**CMN-006:** Pafuri Deposit, Northern Transvaal, South Africa

- CMNMC 31984 (Millerite)
- Individual grains in capsule
- 2<sup>nd</sup> row of “Puck 3” 4 grains

### Samples from Nickel Rim South Mine

**NRS-001:** Nickel Rim South Mine, Sudbury, Ontario, Canada

- 1680 m, 225 E, ground (depth, heading, location)
- Corresponding hand sample

**NRS-002:** Nickel Rim South Mine, Sudbury, Ontario, Canada

- 1680 m, 225 E, ground
- Corresponding hand sample
- Corresponding thin section
- Corresponding PXRD vial

**NRS-003:** Nickel Rim South Mine, Sudbury, Ontario, Canada

- 1680 m, 225 E, ground
- Corresponding hand sample

**NRS-004:** Nickel Rim South Mine, Sudbury, Ontario, Canada

- 1680 m, 225 E, ground
- Corresponding hand sample

**NRS-005:** Nickel Rim South Mine, Sudbury, Ontario, Canada

- 1680 m, 225 E, ground
- Corresponding hand sample

**NRS-006:** Nickel Rim South Mine, Sudbury, Ontario, Canada

- 1680 m, 225 E, ground
- Corresponding hand sample

**NRS-007:** Nickel Rim South Mine, Sudbury, Ontario, Canada

- 1680 m, 225 E, ground
- Corresponding hand sample

**NRS-008:** Nickel Rim South Mine, Sudbury, Ontario, Canada

- 1660 m, 287 E, ground
- Corresponding hand sample

**NRS-009:** Nickel Rim South Mine, Sudbury, Ontario, Canada

- 1660 m, 287 E, ground
- Corresponding hand sample

**NRS-010:** Nickel Rim South Mine, Sudbury, Ontario, Canada

- 1660 m, 287 E, ground
- Corresponding hand sample
- Corresponding thin section
- Corresponding PXRD vial

**NRS-011:** Nickel Rim South Mine, Sudbury, Ontario, Canada

- 1660 m, 287 E, ground
- Corresponding hand sample

**NRS-012:** Nickel Rim South Mine, Sudbury, Ontario, Canada

- 1660 m, 287 E, ground
- Corresponding hand sample

**NRS-013:** Nickel Rim South Mine, Sudbury, Ontario, Canada

- 1660 m, 287 E, ground
- Corresponding hand sample

**NRS-014:** Nickel Rim South Mine, Sudbury, Ontario, Canada

- 1660 m, 287 E, ground
- Corresponding hand sample

**NRS-015:** Nickel Rim South Mine, Sudbury, Ontario, Canada

- 1660 m, 287 E, ground
- Corresponding hand sample
- Corresponding thin section
- Corresponding PXRD vial

**NRS-016:** Nickel Rim South Mine, Sudbury, Ontario, Canada

- 1660 m, 287 E, ground
- Corresponding hand sample

**NRS-017:** Nickel Rim South Mine, Sudbury, Ontario, Canada

- 1660 m, 287 E, ground
- Corresponding hand sample

**NRS-018:** Nickel Rim South Mine, Sudbury, Ontario, Canada

- 1680 m 350 E, wall vein
- Corresponding hand sample

**NRS-019:** Nickel Rim South Mine, Sudbury, Ontario, Canada

- 1680 m 350 E, wall vein
- Corresponding hand sample

**NRS-020:** Nickel Rim South Mine, Sudbury, Ontario, Canada

- 1680 m 350 E, wall vein
- Corresponding hand sample

**NRS-021:** Nickel Rim South Mine, Sudbury, Ontario, Canada

- 1480 m 287 E, ground
- Corresponding hand sample

**NRS-021:** Nickel Rim South Mine, Sudbury, Ontario, Canada

- 1480 m 287 E, ground
- Corresponding hand sample

**NRS-022:** Nickel Rim South Mine, Sudbury, Ontario, Canada

- 1480 m 287 E, ground
- Corresponding hand sample
- Corresponding thin section

**NRS-023:** Nickel Rim South Mine, Sudbury, Ontario, Canada

- 1480 m 287 E, ground
- Corresponding hand sample
- Corresponding thin section
- Corresponding PXRD vial

**NRS-024:** Nickel Rim South Mine, Sudbury, Ontario, Canada

- 1480 m 287 E, ground
- Corresponding hand sample

**NRS-025:** Nickel Rim South Mine, Sudbury, Ontario, Canada

- 1480 m 287 E, ground
- Corresponding hand sample

**NRS-026:** Nickel Rim South Mine, Sudbury, Ontario, Canada

- 1480 m 287 E, ground
- Corresponding hand sample

**NRS-027:** Nickel Rim South Mine, Sudbury, Ontario, Canada

- 1480 m 220 E, wall vein
- Corresponding hand sample

**NRS-028:** Nickel Rim South Mine, Sudbury, Ontario, Canada

- 1480 m 220 E, wall vein
- Corresponding hand sample

**NRS-029:** Nickel Rim South Mine, Sudbury, Ontario, Canada

- 1480 m 220 E, wall vein
- Corresponding hand sample

**NRS-030:** Nickel Rim South Mine, Sudbury, Ontario, Canada

- 1480 m 220 E, wall vein
- Corresponding hand sample

**NRS-031:** Nickel Rim South Mine, Sudbury, Ontario, Canada

- 1480 m 220 E, wall vein
- Corresponding hand sample

**NRS-032:** Nickel Rim South Mine, Sudbury, Ontario, Canada

- 1480 m 220 E, wall vein
- Corresponding hand sample

**NRS-033:** Nickel Rim South Mine, Sudbury, Ontario, Canada

- 1480 m 220 E, wall vein
- Corresponding hand sample

**NRS-034:** Nickel Rim South Mine, Sudbury, Ontario, Canada

- 1480 m 220 E, wall vein
- Corresponding hand sample

**NRS-035:** Nickel Rim South Mine, Sudbury, Ontario, Canada

- 1480 m 220 E, wall vein
- Corresponding hand sample

**NRS-036:** Nickel Rim South Mine, Sudbury, Ontario, Canada

- 1480 m 220 E, wall vein
- Corresponding hand sample
- Corresponding thin section

**NRS-037:** Nickel Rim South Mine, Sudbury, Ontario, Canada

- 1480 m 220 E, wall vein
- Corresponding hand sample

**NRS-038:** Nickel Rim South Mine, Sudbury, Ontario, Canada

- 1480 m 220 E, wall vein
- Corresponding hand sample
- Corresponding thin sections A, B, and, C

**NRS-039:** Nickel Rim South Mine, Sudbury, Ontario, Canada

- 1480 m 220 E, wall vein
- Corresponding hand sample

**NRS-040:** Nickel Rim South Mine, Sudbury, Ontario, Canada

- 1480 m 220 E, wall vein
- Corresponding hand sample
- Corresponding thin section

**NRS-041:** Nickel Rim South Mine, Sudbury, Ontario, Canada

- 1480 m 220 E, wall vein
- Corresponding hand sample
- Corresponding thin section
- Corresponding PXRD vial

**NRS-042:** Nickel Rim South Mine, Sudbury, Ontario, Canada

- 1480 m 220 E, wall vein
- Corresponding hand sample
- Corresponding thin section

**NRS-043:** Nickel Rim South Mine, Sudbury, Ontario, Canada

- 1480 m 220 E, wall vein
- Corresponding hand sample

**NRS-044:** Nickel Rim South Mine, Sudbury, Ontario, Canada

- 1480 m 220 E, wall vein
- Corresponding hand sample

**NRS-045:** Nickel Rim South Mine, Sudbury, Ontario, Canada

- 1480 m 220 E, wall vein
- Corresponding hand sample
- Corresponding thin section

**NRS-046:** Nickel Rim South Mine, Sudbury, Ontario, Canada

- 1480 m 220 E, wall vein
- Corresponding hand sample

**NRS-047:** Nickel Rim South Mine, Sudbury, Ontario, Canada

- 1200 m, wall vein
- Corresponding hand sample

**NRS-048:** Nickel Rim South Mine, Sudbury, Ontario, Canada

- 1200 m, wall vein
- Corresponding hand sample

### **Samples from Coleman Mine**

**COL-001:** Coleman Mine, Sudbury, Ontario, Canada

- 1740 m, wall vein (depth, location)
- Corresponding hand sample

**COL-002:** Coleman Mine, Sudbury, Ontario, Canada

- 1740 m, wall vein (depth, location)
- Corresponding hand sample

**COL-003:** Coleman Mine, Sudbury, Ontario, Canada

- 1740 m, wall vein (depth, location)
- Corresponding hand sample

**COL-004:** Coleman Mine, Sudbury, Ontario, Canada

- 1740 m, wall vein (depth, location)
- Corresponding hand sample
- Corresponding thin section

**COL-005:** Coleman Mine, Sudbury, Ontario, Canada

- 1740 m, wall vein (depth, location)
- Corresponding hand sample

**COL-006:** Coleman Mine, Sudbury, Ontario, Canada

- 1740 m, wall vein (depth, location)
- Corresponding hand sample

**COL-007:** Coleman Mine, Sudbury, Ontario, Canada

- 1780 m, wall vein (depth, location)
- Corresponding hand sample
- Corresponding thin section

**COL-008:** Coleman Mine, Sudbury, Ontario, Canada

- 1780 m, wall vein (depth, location)
- Corresponding hand sample
- Corresponding thin section

**COL-009:** Coleman Mine, Sudbury, Ontario, Canada

- 1780 m, wall vein (depth, location)
- Corresponding hand sample

**COL-010:** Coleman Mine, Sudbury, Ontario, Canada

- 1780 m, wall vein (depth, location)
- Corresponding hand sample

**COL-011:** Coleman Mine, Sudbury, Ontario, Canada

- 1470 m, wall vein (depth, location)
- Corresponding hand sample

**COL-012:** Coleman Mine, Sudbury, Ontario, Canada

- 1470 m, wall vein (depth, location)
- Corresponding hand sample

**COL-013:** Coleman Mine, Sudbury, Ontario, Canada

- 1470 m, wall vein (depth, location)
- Corresponding hand sample

**COL-014:** Coleman Mine, Sudbury, Ontario, Canada

- 1470 m, wall vein (depth, location)
- Corresponding hand sample

**COL-015:** Coleman Mine, Sudbury, Ontario, Canada

- 1470 m, wall vein (depth, location)
- Corresponding hand sample
- Corresponding thin section

**COL-016:** Coleman Mine, Sudbury, Ontario, Canada

- 1470 m, wall vein (depth, location)
- Corresponding hand sample
- Corresponding thin sections A and B

**COL-017:** Coleman Mine, Sudbury, Ontario, Canada

- 1470 m, wall vein (depth, location)
- Corresponding hand sample
- Corresponding thin section
- Corresponding PXRD vial

**COL-018:** Coleman Mine, Sudbury, Ontario, Canada

- 1510 m, wall vein (depth, location)
- Corresponding hand sample

**COL-019:** Coleman Mine, Sudbury, Ontario, Canada

- 1510 m, wall vein (depth, location)
- Corresponding hand sample

**COL-020:** Coleman Mine, Sudbury, Ontario, Canada

- 1510 m, wall vein (depth, location)
- Corresponding hand sample
- Corresponding thin section
- Corresponding PXRD vial

**COL-021:** Coleman Mine, Sudbury, Ontario, Canada

- 1510 m, wall vein (depth, location)
- Corresponding hand sample
- Corresponding PXRD vial

**COL-022:** Coleman Mine, Sudbury, Ontario, Canada

- 1510 m, wall vein (depth, location)
- Corresponding hand sample

**COL-023:** Coleman Mine, Sudbury, Ontario, Canada

- 1510 m, wall vein (depth, location)
- Corresponding hand sample

**COL-024:** Coleman Mine, Sudbury, Ontario, Canada

- 1510 m, wall vein (depth, location)
- Corresponding hand sample

**COL-025:** Coleman Mine, Sudbury, Ontario, Canada

- 1510 m, wall vein (depth, location)
- Corresponding hand sample

**COL-026:** Coleman Mine, Sudbury, Ontario, Canada

- 1510 m, wall vein (depth, location)
- Corresponding hand sample

**COL-027:** Coleman Mine, Sudbury, Ontario, Canada

- 1510 m, wall vein (depth, location)
- Corresponding hand sample

**COL-028:** Coleman Mine, Sudbury, Ontario, Canada

- 1510 m, wall vein (depth, location)
- Corresponding hand sample

**COL-029:** Coleman Mine, Sudbury, Ontario, Canada

- 1510 m, wall vein (depth, location)
- Corresponding hand sample

**COL-030:** Coleman Mine, Sudbury, Ontario, Canada

- 153 ore-body, unknown depth
- Corresponding hand sample

**COL-031:** Coleman Mine, Sudbury, Ontario, Canada

- 153 ore-body, unknown depth
- Corresponding hand sample
- Corresponding thin section A, B, and C
- Corresponding PXRD vial

**COL-032:** Coleman Mine, Sudbury, Ontario, Canada

- 153 ore-body, unknown depth
- Corresponding hand sample
- Corresponding thin section
- Corresponding PXRD vial

**COL-033:** Coleman Mine, Sudbury, Ontario, Canada

- 153 ore-body, unknown depth
- Corresponding hand sample
- Corresponding thin section
- Corresponding PXRD vial

**COL-034:** Coleman Mine, Sudbury, Ontario, Canada

- 153 ore-body, unknown depth
- Corresponding hand sample
- Corresponding thin section

**COL-035:** Coleman Mine, Sudbury, Ontario, Canada

- 153 ore-body, unknown depth
- Corresponding hand sample
- Corresponding thin section

**COL-036:** Coleman Mine, Sudbury, Ontario, Canada

- 153 ore-body, unknown depth
- Corresponding hand sample
- Corresponding thin section

**COL-037:** Coleman Mine, Sudbury, Ontario, Canada

- 153 ore-body, unknown depth
- Corresponding hand sample
- Corresponding thin sections A and B

### **Samples from the Morrison Deposit**

**4090L:** Morrison Deposit, McCreedy East Mine, Sudbury, Ontario, Canada

- 1250 m (depth)
- Corresponding hand sample (from Paul Wawrzonkowski)
- Corresponding thin section (from Paul Wawrzonkowski)

**4090LC:** Morrison Deposit, McCreedy East Mine, Sudbury, Ontario, Canada

- 1250 m
- Corresponding hand sample (from Paul Wawrzonkowski)
- Corresponding thin section (from Paul Wawrzonkowski)

**4090LD:** Morrison Deposit, McCreedy East Mine, Sudbury, Ontario, Canada

- 1250 m
- Corresponding hand sample (from Paul Wawrzonkowski)
- Corresponding thin section (from Paul Wawrzonkowski)

**4090LE:** Morrison Deposit, McCreedy East Mine, Sudbury, Ontario, Canada

- 1250 m
- Corresponding hand sample (from Paul Wawrzonkowski)
- Corresponding thin section (from Paul Wawrzonkowski)

**4090LG:** Morrison Deposit, McCreedy East Mine, Sudbury, Ontario, Canada

- 1250 m
- Corresponding hand sample (from Paul Wawrzonkowski)
- Corresponding thin section (from Paul Wawrzonkowski)

**4090LI:** Morrison mine, Sudbury, Ontario, Canada

- 1250 m
- Corresponding hand sample (from Paul Wawrzonkowski)
- Corresponding thin section (from Paul Wawrzonkowski)

**4090LO:** Morrison Deposit, McCreedy East Mine, Sudbury, Ontario, Canada

- 1250 m
- Corresponding hand sample (from Paul Wawrzonkowski)
- Corresponding thin section (from Paul Wawrzonkowski)

**4210L:** Morrison Deposit, McCreedy East Mine, Sudbury, Ontario, Canada

- 1280 m
- Corresponding hand sample (from Paul Wawrzonkowski)
- Corresponding thin section (from Paul Wawrzonkowski)

**4210L9:** Morrison Deposit, McCreedy East Mine, Sudbury, Ontario, Canada

- 1280 m
- Corresponding hand sample (from Paul Wawrzonkowski)
- Corresponding thin section (from Paul Wawrzonkowski)

**4340Lb:** Morrison Deposit, McCreedy East Mine, Sudbury, Ontario, Canada

- 1320 m
- Corresponding hand sample (from Paul Wawrzonkowski)
- Corresponding thin section (from Paul Wawrzonkowski)

**4340Lb:** Morrison Deposit, McCreedy East Mine, Sudbury, Ontario, Canada

- 1320 m
- Corresponding hand sample (from Paul Wawrzonkowski)
- Corresponding thin section (from Paul Wawrzonkowski)

**4340LC:** Morrison Deposit, McCreedy East Mine, Sudbury, Ontario, Canada

- 1320 m
- Corresponding hand sample (from Paul Wawrzonkowski)
- Corresponding thin section (from Paul Wawrzonkowski)

**4340Ld:** Morrison Deposit, McCreedy East Mine, Sudbury, Ontario, Canada

- 1320 m
- Corresponding hand sample (from Paul Wawrzonkowski)
- Corresponding thin section (from Paul Wawrzonkowski)

**4600L:** Morrison Deposit, McCreedy East Mine, Sudbury, Ontario, Canada

- 1400 m
- Corresponding hand sample (from Paul Wawrzonkowski)
- Corresponding thin section (from Paul Wawrzonkowski)

**Millerite:** Morrison Deposit, McCreedy East Mine, Sudbury, Ontario, Canada

- Unknown depth
- Corresponding hand sample (from Paul Wawrzonkowski)
- Corresponding thin section (from Paul Wawrzonkowski)

### **Samples Synthesized by CVT**

**SYN-001:** Synthetic

- Grown in sealed capsule from 700 → 600 °C
- Natural millerite (COL-031), crystalline iodine
- Individual grain on capsule segments
- Individual grains on carbon tape (corresponding slide)
- 001 row of “High Temperature Synthesis” puck, 6 grains

**SYN-002:** Synthetic

- Grown in sealed capsule from 800 → 700 °C
- Natural millerite (COL-031), crystalline iodine
- Individual grain on capsule segments
- Individual grains on carbon tape (corresponding slide)
- 002 row of “High Temperature Synthesis” puck, 6 grains

**SYN-003:** Synthetic

- Grown in sealed capsule from 800 → 700 °C
- Natural millerite (COL-031), crystalline iodine
- Individual grain on capsule segments
- Individual grains on carbon tape (corresponding slide)
- 003 row of “High Temperature Synthesis” puck, 6 grains